Instituto Superior
de Engenharia
Politécnico de Coimbra

DEPARTAMENTO DE ENGENHARIA
ELETROTÉCNICA

# Double Coupling Dynamic Inductive Power Transfer Systems for Electric Vehicles Charging Applications

Trabalho de Projeto para a obtenção do grau de Mestre em Engenharia Eletrotécnica

Especialização em Automação e Comunicações em Sistemas Industriais

Autor

**Miguel Moreira Torres**

Orientador

**Professora Doutora Marina Mendes Sargento Domingues Perdigão**

INSTITUTO POLITÉCNICO
DE COIMBRA

INSTITUTO SUPERIOR
DE ENGENHARIA
DE COIMBRA

Coimbra, março 2024

# Resumo

Os veículos elétricos (EV)s estão a crescer em popularidade, mas o carregamento frequente é inconveniente. A tecnologia de transferência de energia sem fios (WPT) oferece uma solução, permitindo que os EVs sejam carregados sem contacto. Uma tecnologia WPT que tem sido muito utilizada para o carregamento estático de EVs é a transferência de energia indutiva (IPT). Para carregar EVs em movimento, é necessária uma tecnologia IPT dinâmica (DIPT), pelo que esta tecnologia utiliza infraestruturas de carregamento especializadas, incluindo bobinas implementadas na estrada, para transferir energia para o EV em movimento. No DIPT, as deslocações inerentes ao sentido de marcha, bem como os desalinhamentos já esperados (verticais e laterais), originam diferentes condições de acoplamento (sem acoplamento a acoplamento total). É utilizado um sistema IPT na roda (inWIPT) de acoplamento duplo para transferir energia do lado de fora para o lado de bordo do EV, utilizando a roda como intermediário. O sistema proposto incorpora dois acopladores magnéticos (MC) para a transferência de energia entre o lado de fora do veículo e a roda e outro da roda para o lado de bordo, mantendo o entreferro a um nível mínimo e quase independente do tipo de veículo. A compensação ressonante S-S-S, já analisada para a aplicação estática inWIPT, não apresenta uma solução viável para o DIPT. Este trabalho de mestrado apresenta o estudo das estratégias adoptadas para avaliar a aplicabilidade e o desempenho do sistema inWIPT em DIPT. Para tal, é efetuada uma análise matemática de compensações ressonantes como S-S-S, LCL-S-S e LCC-S-S em operação DIPT para identificar as suas características intrínsecas e permitir a limitação de correntes e tensões no lado do transmissor a valores aceitáveis. Também incluí medições experimentais e análise da indutância própria/mútua e dos perfis de acoplamento para diferentes geometrias do sistema proposto, a fim de avaliar a sua tolerância em condições DIPT específicas. O protótipo experimental utilizando a topologia LCL-S-S e as simulações MATLAB/Simulink validam toda a gama de condições de acoplamento e de carga, desde o acoplamento total até ao desacoplamento.

**Palavras-chave**: Transferência de Energia Indutiva em modo Dinâmico (DIPT), Veículo Elétrico (EV), In-wheel, Sistema de Duplo Acoplamento, Conversor Ressonante

# Abstract

Electric vehicles (EV)s are growing in popularity, but frequent recharging is inconvenient. Wireless power transfer (WPT) technology offers a solution, allowing EVs to be charged without contact. A WPT technology that has been widely used for static charging of EVs is inductive power transfer (IPT). In order to charge EVs in motion, a dynamic IPT (DIPT) technology is required, therefore this technology uses specialized charging infrastructure, including coils implemented in the road, to transfer energy to the moving EV. In DIPT, inherent displacements in the travel direction, as well as the already expected misalignments (vertical and lateral) lead to different coupling conditions (no-coupling to full-coupling). A double coupling in-Wheel IPT (inWIPT) system is used for transferring energy from the off-board to the on-board side of EV using the wheel as an intermediary. The proposed system incorporates two magnetic couplers (MC) for the energy transfer between the off-board side to the wheel and another from the wheel to the on-board side, keeping the air gap to a minimum and almost independent of the vehicle type. The S-S-S resonant compensation, already analysed for the static inWIPT application, does not present a viable solution for DIPT. This master's work presents the study of adopted strategies to assess the applicability and performance of the inWIPT system in DIPT. Therefore, a mathematical analysis of resonant compensations such as S-S-S, LCL-S-S and LCC-S-S is carried out in DIPT operation to identify their intrinsic characteristics for enabling the limitation of currents and voltages on the transmitter side to acceptable values. Additionally, it includes experimental measurements and analysis of self/mutual inductance and coupling profiles for different geometries of the proposed system to assess their tolerance under specific DIPT conditions. The experimental prototype using LCL-S-S topology and the MATLAB/Simulink simulations validate the full range of coupling and load conditions, from full to no-coupling.

**Keywords**: Dynamic Inductive Power Transfer (DIPT), Electric Vehicle (EV), In-wheel, Double Coupling System, Resonant Converter

# Dedication

This work is dedicated to my parents, who have supported me throughout my academic journey. Their inspiration, encouragement, and sacrifices have enabled me to pursue my dreams and reach my full potential. Without their guidance and support, this achievement would not have been possible.

I dedicate this thesis to my colleagues from Instituto de Telecomunicações - Coimbra for accepting me as a member and supporting throughout my master's degree project.

Lastly, I would also like to dedicate this thesis to my closest friends, who have always been my pillars of strength and my biggest cheerleaders. Their constant motivation and support have helped me overcome challenges and push my limits.

Miguel Torres

## Acknowledgments

I would like to express my gratitude to the following people who have helped and supported me throughout the completion of this thesis: First and foremost, I would like to thank my thesis advisor Professor Doctor Marina Mendes Sargento Domingues Perdigão and my colleagues Master Válter de Sousa Costa and Doctor Emanuel Gonçalves Marques for their guidance, encouragement, and patience during the entire process. Their knowledge, expertise, and insights have been invaluable in shaping this thesis.

I would like to extend my thanks to Professor Doctor André Manuel dos Santos Mendes, to my colleagues from Instituto de Telecomunicações - Coimbra and to my friend and colleague from Coimbra University Isidro Ribeiro, for their support, motivation, and helpful discussions that have inspired and motivated me to complete this thesis.

I am also grateful to the members of my thesis committee, for their constructive feedback, suggestions, and critical insights that have significantly improved the quality of my work.

I also want to acknowledge the support and understanding of my family, for their unwavering encouragement, love, and patience during this journey.

Finally, I want to express my gratitude to all those who have contributed in some way, big or small, to the completion of this thesis.

Thank you.

# Contents

# List of Tables

# List of Figures

## List of abbreviations

| | |
|---|---|
| ECCE | *Energy Conversion Congress & Expo* |
| ICNIRP | *International Commission on Non-Ionizing Radiation Protection* |
| IEEE | *Institute of Electrical and Electronics Engineers* |
| ISEC | Instituto Superior de Engenharia de Coimbra |
| MIT | *Massachusetts Institute of Tecnhology* |
| VPPC | *Vehicle Power and Propulsion* |
| SAE | *Society of Automotive Engineers* |

# Acronyms

| | |
|---|---|
| AC | Alternating current |
| AGV | Automated guided vehicles |
| BMS | Battery management system |
| BPP | Bipolar pad |
| CC | Constant current |
| CP | Circular pad |
| CPT | Capacitive power transfer |
| CV | Constant voltage |
| DC | Direct current |
| DDP | Double-D pad |
| DSP | Digital signal processor |
| DIPT | Dynamic inductive power transfer |
| EMF | Electromagnetic field |
| EMI | Electromagnetic interference |
| EV | Electric vehicle |
| FEA | Finite element analysis |
| FHA | First harmonic approximation |
| HF | High frequency |
| IC | Intermediate coupler |
| ICE | Internal combustion engine |
| ICWPT | Inductive coupled wireless power transfer |
| IMD | Implantable medical device |
| inWIPT | In-wheel inductive power transfer |
| IPT | Inductive power transfer |
| IRMC | Inner rim magnetic coupler |
| IWM | In-wheel motors |
| LCC | Inductor-Capacitor-Capacitor resonant configuration |
| LCC-S-S | Inductor-Capacitor-Capacitor-Series-Series double coupling resonant configuration |
| LCL | Inductor-Capacitor-Inductor resonant configuration |
| LCL-S-S | Inductor-Capacitor-Inductor-Series-Series double coupling resonant configuration |
| LIO | Load independent operation |
| LPT | Laser power transfer |

| | |
|---|---|
| MC | Magnetic coupler |
| MCRWPT | Magnetically coupled resonance wireless power transfer |
| MOSFET | Metal–oxide Semiconductor field effect transistor |
| ORMC | Outer rim magnetic coupler |
| PFC | Power factor correction |
| PHEV | Plug-in hybrid electric vehicle |
| PHS | Phase shift |
| RFPT | Radio frequency power transfer |
| RMS | Root mean square |
| SBT | Space between turns |
| SiC | Silicon carbide |
| SIPT | Static inductive power transfer |
| SoC | State of charge |
| SP | Solenoid pad |
| S-LCL | Series configuration in the transmitter side and Inductor-Capacitor-Inductor configuration in the receiver side |
| S-S | Series-Series resonant configuration |
| S-S-S | Series-Series-Series double coupling resonant configuration |
| S-S-P | Series-Series-Parallel double coupling resonant configuration |
| UAV | Unmanned aerial vehicle |
| WIWM | Wireless in-wheel motor |
| WPT | Wireless power transfer |
| ZCS | Zero current switching |
| ZPA | Zero phase angle |
| ZVS | Zero voltage switching |

# Nomenclature

| | |
|---|---|
| air gap or $airgap$ | Distance between the transmitter and receiver coils |
| $A$ | Ampere |
| $A_{rms}$ | RMS Ampere |
| $B$ | Magnetic field |
| $Coil_l$ | Length of ORMC transmitter or receiver coil |
| $Coil_w$ | Width of ORMC transmitter or receiver coil |
| $Coil_{lint}$ | Interior length of ORMC transmitter or receiver coil |
| $Coil_{lintcomb}$ | Interior combination length of ORMC transmitter or receiver coil |
| $Coil_{loverlap}$ | Overlapped length of ORMC Bipolar Pad receiver coil |
| $Coil_{lintoverlap}$ | Interior overlapped length of ORMC Bipolar Pad receiver coil |
| $Coil_{wint}$ | Interior width of ORMC transmitter or receiver coil |
| $C_s$ | Capacitor at the input side |
| $C_1$ | Capacitor of the ORMC transmitter resonant tank |
| $C_2$ | Capacitor of the wheel resonant tank |
| $C_4$ | Capacitor of the IRMC receiver resonant tank |
| $d_{L3}$ | Length of IRMC transmitter coil |
| $d_{L4}$ | Length of IRMC receiver coil |
| $e$ | Magnitude of the induced voltage |
| $e_1$ | Magnitude of the transmitter induced voltage |
| $e_2$ | Magnitude of the receiver induced voltage |
| $F$ | Farad |
| $f_o$ | Natural frequency |
| $f_r$ | Resonance frequency |
| $f_s$ | Switching frequency |
| $g_{12}$ | ORMC air gap |
| $g_{34}$ | IRMC air gap |
| $G_{vReqvin}$ | Voltage gain function between the on-board receiver side and input side |
| $G_{i4vin}$ | Transconductance gain function between on-board receiver side and input side |
| $G_{i1vin}$ | Transconductance gain function between off-board transmitter side and input side |
| $H$ | Henry |
| $Hz$ | Hertz |
| $I$ | Current |

| | |
|---|---|
| $\overline{I}_{in}$ | Current phasor at the input side or at the inverter output terminals |
| $\overline{I}_{in_{(s)}}$ | Current phasor at the input side or at the inverter output terminals using Laplace transform |
| $\overline{I}_{out}$ or $\overline{I}_{bat}$ | Current phase in the batteries |
| $I_{R_{bat\,RMS}}$ | RMS current in the batteries |
| $\overline{I}_{sc}$ | Current phasor in the receiver coil during the short-circuit test |
| $\overline{I}_{sc_{res}}$ | Current phasor in the receivor coil during the short-circuit test with resonant tank |
| $\overline{I}_1$ | Current phasor in the off-board transmitter side |
| $\overline{I}_{1_{(s)}}$ | Current phasor in the off-board transmitter side using Laplace transform |
| $\overline{I}_2$ | Current phasor in the wheel side |
| $\overline{I}_{2_{(s)}}$ | Current phasor in the wheel side using Laplace transform |
| $\overline{I}_4$ or $\overline{I}_{R_{eq}}$ | Current phasor in the on-board side or in the equivalent resistance |
| $\overline{I}_{4_{(s)}}$ | Current phasor in the on-board side using Laplace transform |
| $I_{C_{s_{RMS}}}$ | RMS input capacitor side |
| $I_{C_{1_{RMS}}}$ | RMS transmitter tank capacitor side |
| $I_{DC_{RMS}}$ | RMS DC bus current |
| $I_{in_{RMS}}$ | RMS value in the current on input circuit |
| $I_{1_{RMS}}$ | RMS value in the current on off-board transmitter side |
| $I_{2_{RMS}}$ | RMS value in the current on outer rim circuit |
| $I_{4_{RMS}}$ or $I_{R_{eq_{RMS}}}$ | RMS value in the current on on-board side or in the equivalent resistance |
| $k$ | Coupling coefficient |
| $km$ | Kilometer |
| $km/h$ | Kilometer per hour |
| $k_+$ | Series coupling coefficient connection |
| $k_-$ | Anti-series coupling coefficient connection |
| $k_1$ | Coupling coefficient of transmitter coil |
| $k_2$ | Coupling coefficient of receiver coil |
| $k_{12}$ | Coupling coefficient between the transmitter and receiver coils in two-coil systems and of the ORMC in inWIPT system |
| $k_{34}$ | Coupling coefficient between the transmitter and receiver coils of the IRMC in inWIPT system |
| $L$ | Self-inductance |
| $L_s$ | Self-inductance at the input coil side |
| $L_T$ | Total inductance |
| $L_{T_+}$ | Series inductance connection |
| $L_{T_-}$ | Anti-series inductance connection |
| $L_1$ | Self-inductance of the transmitter coil in two-coil system and of the ORMC in inWIPT system |
| $L_2$ | Self-inductance of the receiver coil in two-coil system and of the ORMC |

| | |
|---|---|
| | in inWIPT system |
| $L_3$ | Self-inductance of the transmitter coil of the IRMC in inWIPT system |
| $L_4$ | Self-inductance of the receiver coil of the IRMC in inWIPT system |
| $L_{12}$ | Mutual inductance between the transmitter and receiver coils in two-coil systems and of the ORMC in inWIPT system |
| $L_{12_{max}}$ | Maximum value of ORMC mutual inductance in inWIPT system |
| $L_{34}$ | Mutual inductance between the transmitter and receiver coils of the IRMC in inWIPT system |
| $l$ | Coil length |
| $mm$ | Millimeter |
| $M$ | Mutual inductance |
| $M_x$ | Lateral displacement |
| $M_+$ | Series mutual inductance connection |
| $M_-$ | Anti-series mutual inductance connection |
| $M_{12}$ | Mutual inductance of coil 1 linking coil 2 |
| $M_{21}$ | Mutual inductance of coil 2 linking coil 1 |
| $N$ | Number of turns of a coil |
| $Q$ | Quality factor |
| $P_{DC_{RMS}}$ | RMS power of DC bus |
| $P_{in_{RMS}}$ | RMS input side power or at the inverter output terminals |
| $P_{out}$ or $P_{bat}$ | Output power or power of the batteries |
| $P_{R_{eq\,RMS}}$ | RMS power in the equivalent resistance of the batteries before rectifier action |
| $P_{R_{bat\,RMS}}$ | RMS power in the batteries |
| $P_{su}$ | Uncompensated apparent power |
| $P_{sc}$ | Compensated apparent power |
| $rad/s$ | Radian per second |
| $R_{bat}$ or $R_o$ | Resistance of the batteries |
| $R_{eq}$ | Equivalent resistance of the batteries before rectifier action |
| $r_s$ | Resistance of the input coil side |
| $r_1$ | Resistance of the transmitter coil of two and three-coil systems and of the ORMC in inWIPT system |
| $r_2$ | Resistance of the receiver coil of two and three-coil systems and of the ORMC in inWIPT system |
| $r_3$ | Resistance of the IRMC transmitter coil in inWIPT system |
| $r_4$ | Resistance of the IRMC receiver coil in inWIPT system |
| $r_{L2}$ | Radius of ORMC receiver coil |
| $S$ | Cross section |
| $Sad_{BPP}$ | Saddle Bipolar Pad |
| $SoC_{min}$ | Minimum State of Charge value |

| | |
|---|---|
| $SoC_{max}$ | Maximum State of Charge value |
| $s$ | Second or variable for Laplace transform |
| $T$ | MATLAB/Similink time |
| $T_{step}$ | MATLAB/Simulink sampling time |
| $T_{stop}$ | MATLAB/Simulink stop time |
| $V$ | Volt |
| $VA$ | Volt-Ampere |
| $V_{DC}$ | DC bus voltage link |
| $V_{DC_{RMS}}$ | RMS DC bus voltage |
| $\overline{V}_{bat}$ | Voltage phasor in batteries |
| $\overline{V}_{C_s}$ | Voltage phasor in the capacitor on the input side |
| $V_{C_{s_{RMS}}}$ | RMS voltage in the capacitor on the input side |
| $\overline{V}_{C_{s_{(s)}}}$ | Voltage phasor in the capacitor at the input side using Laplace transform |
| $\overline{V}_{C_1}$ | Voltage phasor in the capacitor of the ORMC transmitter resonant tank |
| $V_{C_{1_{RMS}}}$ | RMS voltage in the capacitor of the ORMC transmitter resonant tank |
| $\overline{V}_{C_{1_{(s)}}}$ | Voltage phasor in the capacitor of the ORMC transmitter resonant tank using Laplace transform |
| $\overline{V}_{C_2}$ | Voltage phasor in the capacitor of the wheel resonant tank |
| $V_{C_{2_{RMS}}}$ | RMS voltage in the capacitor of the wheel resonant tank |
| $\overline{V}_{C_4}$ | Voltage phasor in the capacitor of the IRMC receiver resonant tank |
| $V_{C_{4_{RMS}}}$ | RMS voltage in the capacitor of the IRMC receiver resonant tank |
| $\overline{V}_{in}$ | Voltage phasor at the input side or at the inverter output terminals |
| $V_{in_{RMS}}$ | RMS input side or at the inverter output terminals |
| $\overline{V}_{in_{(s)}}$ | Voltage phasor at the input side or at the inverter output terminals using Laplace transform |
| $\overline{V}_{L_s}$ | Voltage phasor in the input coil side |
| $V_{L_{s_{RMS}}}$ | RMS input coil side |
| $\overline{V}_{L_1}$ | Voltage phasor in the ORMC transmitter coil |
| $\overline{V}_{L_2}$ | Voltage phasor in the ORMC receiver coil |
| $\overline{V}_{L_3}$ | Voltage phasor in the IRMC transmitter coil |
| $\overline{V}_{L_4}$ | Voltage phasor in the IRMC receiver coil |
| $\overline{V}_{oc}$ | Voltage phasor in the receiver coil during the open-circuit test |
| $\overline{V}_{R_{eq}}$ | Voltage phasor in the equivalent resistance of the batteries before rectifier action |
| $V_{R_{bat_{RMS}}}$ | RMS voltage in the batteries |
| $V_{R_{eq_{RMS}}}$ | RMS voltage in the equivalent resistance of the batteries before rectifier action |
| $V_{rms}$ | RMS voltage value |
| $V_{r_s}$ | Voltage at the resistance of the input coil side |
| $V_{r_1}$ | Voltage in the resistance of the ORMC transmitter coil |

| | |
|---|---|
| $V_{r_2}$ | Voltage in the resistance of the ORMC receiver coil |
| $V_{r_3}$ | Voltage in the resistance of the IRMC transmitter coil |
| $V_{r_4}$ | Voltage in the resistance of the IRMC receiver coil |
| $V_{1_{RMS}}$ | RMS Voltage of ORMC transmitter coil |
| $V_{2_{RMS}}$ | RMS Voltage of ORMC receiver coil |
| $V_{3_{RMS}}$ | RMS Voltage of IRMC transmitter coil |
| $V_{4_{RMS}}$ | RMS Voltage of IRMC receiver coil |
| $\overline{V}_{12}$ | Voltage phasor of ORMC transmitter coil linking ORMC receiver coil |
| $\overline{V}_{21}$ | Voltage phasor of ORMC receiver coil linking ORMC transmitter coil |
| $\overline{V}_{34}$ | Voltage phasor of IRMC transmitter coil linking IRMC receiver coil |
| $\overline{V}_{43}$ | Voltage phasor of IRMC receiver coil linking IRMC transmitter coil |
| $W$ | Watt |
| $Z_{in}$ | Equivalent impedance of the input side |
| $Z_1$ | Impedance of the ORMC transmitter resonant tank in inWIPT system |
| $Z_2$ | Impedance of the wheel resonant tank in inWIPT system |
| $Z_4$ | Impedance of the IRMC receiver resonant tank in inWIPT system |
| $Z_{r_{IRMC}}$ | Reflected impedance from the on-board side onto the wheel side in inWIPT system |
| $Z_{r_{ORMC}}$ | Reflected impedance from the wheel side onto the transmitter side in inWIPT system |
| $\alpha$ | Phase angle |
| $\Omega$ | Ohm |
| $\omega$ | Operational angular frequency of the system |
| $\omega_1$ | Natural angular frequency of the transmitter resonant tank in two-coil syst |
| $\omega_2$ | Natural angular frequency of the receiver resonant tank in two-coil system |
| $\omega_4$ | Natural angular frequency of on-board resonant tank in inWIPT system |
| $\theta_s$ | Wheel's rotation for Bipolar pad |
| $\theta I_{in}$ | Phase of the current at the input side in inWIPT system |
| $\theta I_1$ | Phase of the current in the off-board ORMC transmitter side in inWIPT system |
| $\theta I_2$ | Phase of the current in the wheel side in inWIPT system |
| $\theta I_4$ | Phase of the current in the on-board IRMC receiver side in inWIPT system |
| $\Phi$ | Magnetic flux |
| $\Phi_1$ | Magnetic flux on the transmitter winding |
| $\Phi_2$ | Magnetic flux on the receiver winding |
| $\Phi_{12}$ | Magnetic flux of transmitter winding linking receiver winding |
| $\Phi_{21}$ | Magnetic flux of receiver winding linking transmitter winding |

| | |
|---|---|
| $\mu_o$ | Permeability of free space |
| $^\circ$ | Degrees |

# 1 Introduction

In contrast to conventional vehicles that rely on internal combustion engines (ICE), electric vehicles (EV)s have gained significant importance due to their energy efficiency and minimal carbon emissions. These two factors have made them a more appealing option among consumers, leading to their growing popularity. Despite these benefits, one of the key challenges with EVs is the requirement for frequent recharging, which may pose an inconvenience to the drivers. To overcome this issue, wireless power transfer (WPT) technology [1] has emerged as a potential solution, enabling EVs and others applications to be charged without the need for physical connections [2, 3].

The impact of magnetic induction has been the subject of study in the last century with numerous applications. The development of semiconductors with high switching frequencies has enabled the creation of energy transmission systems with large air gap and high efficiency. The operating method of an IPT system is similar to that of a transformer, with the main difference in the air gap value between primary and secondary. The lack of contact between the two parts of the system makes it suitable for safe and efficient energy transfer in different environments, while also ensuring galvanic isolation between the two parts of the system. Reliability, safety of the electric energy supply and simplicity, can be achieved by using a contactless power transfer to an electrical load.

## 1.1 Overview of wireless power transfer

Wireless charging [4] was first demonstrated in the 19th century by Nikola Tesla, who believed that wireless energy transmission was possible. He conducted several experiments with the hope of creating a wireless communication system available to everyone. In 2007 [5], researchers from the *Massachusetts Institute of Technology* (MIT) announced that they had discovered an efficient solution for transmitting energy between separated coils over a distance of a few meters using the technique of resonant coupling.

Until today, new studies have been carried out in the scope of this technology and, as a result, have emphasized the various applications in order to introduce this new technology through electronic devices, charging of EV batteries, and others. Therefore, the continuous study of this technology has presented new proposals to overcome limitations without user intervention.

### 1.1.1 Classification of WPT

A WPT system enables the transmission of electrical energy from a power source to an electronic device without the need for physical connections, allowing the wireless energy transfer between transmitter and receiver through a variable magnetic field.

These systems are typically divided into two categories due to the mechanisms of energy transmission as shown in Fig. 1.1 and Table 1.1 [3]:

- Far-field WPT [3] uses an electromagnetic wave in the form of radio frequency signal for longer ranges, resulting a decrease in energy transfer capacity for communication and photo-electricity purposes. Within this group, there is radio frequency power transfer (RFPT) which is a type of wireless transmission of energy using diffused microwaves as a medium to transfer energy. This technology is applied in aviation and mobile applications. On the other hand [3, 4], there is laser power transfer (LPT) which is a type of wireless transmission of energy using highly concentrated laser light pointed at the receiver to obtain the best efficiency over long distances. These systems have many applications, such as, powering satellites and providing power for devices and remote sensors.
- Near-field WPT [4] uses magnetic or electric field for wireless transmission in shorter environments to be used in power applications. These systems provide a high efficiencies for different applications from low to high power systems. Furthermore, inductive power transfer (IPT) and capacitive power transfer (CPT) systems are often noted for its widespread adoption in various industries and the considerable attention it has garnered for its continuous evolution and development (EVs, biomedicine and more). IPT systems use varying magnetic field to achieve power transfer between the transmitter and receiver coils. Alternatively, CPT systems apply an electric field for transmission of energy with the use of transmitter and receiver which are two flat capacitors. These systems [4]

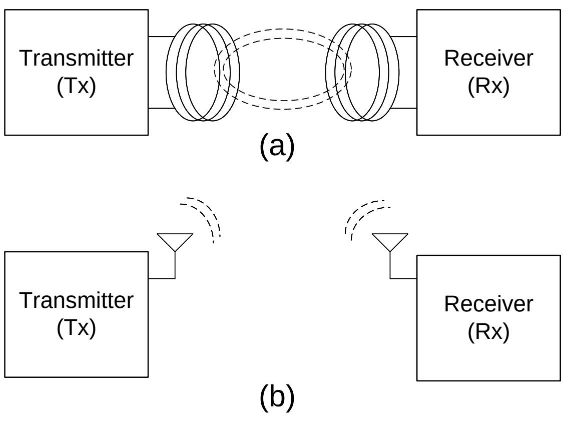


Figure 1.1: Wireless power transfer techniques: (a) Near-field and (b) Far-field [4].

are preferable for reduced powers, as the ratio between power and size is much higher when compared to magnetic coupling systems, hence its wide applicability in charging electronic devices.

Table 1.1: Principal characteristics of different WPT technologies [3].

| WPT technique | WPT technology | Power transfer | Distances | Frequency | Efficiency |
|---|---|---|---|---|---|
| Near-field (non-radiative) | Inductive power transfer (IPT) | W to MW | Short | kHz to MHz | High |
| | Capacitive power transfer (CPT) | W to kW | Short | kHz to MHz | High |
| Far-field (radiative) | Radio frequency power transfer (RFPT) | mW or kW | Long | MHz to GHz | Low |
| | Laser power transfer (LPT) | W or kW | Long | > THz | Medium |

## 1.2 Inductive power transfer systems

Inductive power transfer (IPT) [6] is a type of WPT technology that has been widely used for static (parked car) and dynamic (moving car) charging of EVs. These systems use a charging pad that is connected to a power source, and the EV is parked on top of it. The charging pad contains a coil that generates a magnetic field, and the EV is equipped with a receiving coil that converts the magnetic field into electrical energy, which charges the battery. The benefits of such configuration includes galvanic isolation, operation under different weather conditions and energy transfer capabilities with a fixed (static) or moving (dynamic) receiver. However, there are limiting factors of the power transfer capability such as the low coupling factor between the transmitter and receiver pads of the magnetic coupler (MC) and the compliance of *International Commission on Non-Ionizing Radiation Protection* (ICNIRP) guidelines rules to human exposure of magnetic fields.

IPT systems can further be divided inductive coupled wireless power transfer (ICWPT) and magnetically coupled resonance wireless power transfer (MCRWPT) [7]. ICWPT systems [4] are designed to transfer energy by means of a magnetic field between two coupled coils at close range in its basic configuration. However [4], these IPT systems have limitations regarding their energy efficiency during transfer due to the air gap between the transmitter and receiver, which causes flux losses and decreases the energy transfer capability by increasing reactive losses compared to conventional systems. To address this issue, capacitors are added either on the transmitter or receiver side in different combinations to operate at resonance in both the transmitter and receiver sides of the system. Their addition with the pads belonging to the MC designates resonant compensation systems or MCRWPT. For these systems, the use of high-frequency (HF) with resonant compensation enhances the energy transfer capability in order to achieve higher efficiency with a lower coupling factor [8]. It also allows reducing switching losses in the power circuit by avoiding hard switching.

### 1.2.1 IPT applications

IPT technology has opened up new possibilities for WPT in various applications, delivering low or high levels of power over different distances with the respective efficiencies, frequencies and other parameters, according to the needs of users.

This technology has a wide window of applications from low-power scenarios (1-10 W) such as toothbrushes, heating system [12], induction cooker [13] and TV [14] for daily appliances to high-power scenarios (kW) such as electric transportation [15, 16, 17], unmanned aerial vehicles (UAV)s [18], robot manipulation [19]. For instance [9], Wibotic wireless charging technology can be used to power and recharge small robots or drones that require lower power levels, such as a few watts or tens of watts. At the same time, their systems are also capable of delivering higher power levels, which can be suitable to charging larger industrial robots or EVs. For example, Fig 1.2 (a) presents products such as UAVs and Automated Guided Vehicles (AGV)s developed by Wibotic. Wibotic offers a wide range of modules for various needs. Their UAV can be designed with a transmitter TR-301 and an on-board OC-251, which has an output of 250 W and it is supplied with an input 90 - 264 $V_{DC}$ with 50-60 Hz. In addition, their AGV can incorporate with the same transmitter and an on-board OC-301, that has an output of 300 W and the same input electrical specifications.

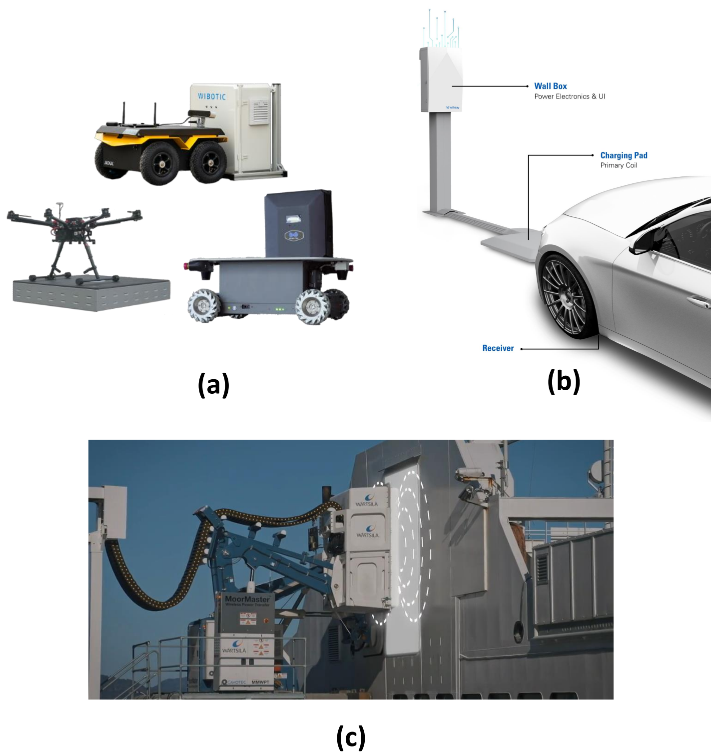


Figure 1.2: (a) Examples of charging systems developed by Wibotic for robot applications [9] and (b) Charging EV system developed by Witricty [10] and (c) the Wärtsilä wireless vessel charging system [11].

Other lower power scenarios can be applied in the field of medicine and using this technology is a big step of evolution due to the disadvantages of using conventional apparatus in humans. Implantable medical devices (IMD) [20, 21] such as artificial cardiac pacemakers, cardiac monitoring, nerve stimulators, and others are different devices that are being designed with IPT technology to avoid, specifically, battery replacement and improving their efficiency. Recent design and other up-to-date implementations [22, 23] can achieve considerable efficiency over near air gap, taking account of safety considerations and being applicable for this type of scenarios. Moreover, portable devices such as laptops and mobile phones [24] are designed by large companies and commercialized to be supplied with a standard compliant wireless charger such as Qi charger, Airpulse charging pad and many others.

Higher power applications, such as EVs are the focus within the scope of WPT, in particular IPT. These EVs have been developed [3] according to the US standard called *Society of Automotive Engineers* (SAE)J2954, which describes the criteria for interoperability, electromagnetic compatibility, and other considerations to agree with the rest of the standards around the world. For instance, WiTricity Corporation [10] was founded in 2007 to commercialize a new technology for wireless electricity invented and patented two years earlier by a team of physicists of MIT, from EV use case to consumer electronics and others applications. Fig 1.2 (b) presents a SIPT charging system developed by Witricity for an EV. The wall box is composed of high-power electronics that convert the grid supply to HF energy that is delivered to the charging pad. Additionally, a MC is presented to transfer the energy to the vehicle, each pad containing the proper configuration and construction to allow the batteries to charge. WiTricity [10] delivers scalable charging rates from 3.6 to 22 kW, to meet the needs of vehicles ranging from plug-in hybrid electric vehicls (PHEV)s with small capacity battery packs to EV's with high capacity, long range battery packs, according to SAEJ2954 standards.

Another example of these applications is wireless vessel charging system developed by Wärtsilä [11], which this marine battery charging system is especially ideal for fully electric vessels that have minimal docking times, such as ferries. The wireless charger has a sending coil on-shore with y and z axis movement. It connects to a nearby power electronic unit supporting grid connection and shore-based energy storage. Input voltage to the power electronics is 690 V 50/60 Hz. On the ship side, a similar coil arrangement is used, with the receiving coil plate mounted flush with the vessel's side. This coil setup connects to a rectifier for DC conversion. This autonomous system can transfer more than 2 MW with a distance between the coils of about 4- 500 $mm$, ensuring a low maintenance and high safety with galvanic isolation.

In the context of DIPT [26], ElectReon Wireless, an Israeli company specialising in inductive charging of EVs by offering a convenient and viable charging solution for a cleaner and greener transportation future. The innovative approach of the company


(a) (b)

Figure 1.3: (a) Electreon's wireless charging system and (b) Wireless charging infrastructure deployment [25].

involves embedding wireless charging technology directly into the road infrastructure, enabling EVs to charge while driving, eliminating the need for frequent stops at charging stations. Fig 1.3, Electreon will deploy its technology in a public wireless road project in Germany, which will power a public electric bus. In Fig 1.3 (a), it is observed the depiction of the charging system, addressing from the start of transmission of electric energy from the grid to the charging system and then to the charging of electric bus batteries. Additionally, a real-time management system is presented to monitor the bus's operating mode. Furthermore in Fig 1.3 (b), the 1 $km$ of coils is installed underneath the road to therefore, being repaved with asphalt to construct the road surface and to ensure the proper condition of the road.

### 1.2.2 Basic IPT system configuration

Essentially [6], an IPT system uses a pair of magnetically linked coils, commonly referred to as power pads or MC, to facilitate the transfer of energy between the off-board and on-board components, as depicted in Fig. 1.4.

On the off-board side, it is composed by an AC-DC converter (rectifier) in order to obtain from an alternating current (AC) signal, for example an electrical network at 50 Hz, a direct current (DC) signal. This rectifier should have an output capacitor, called

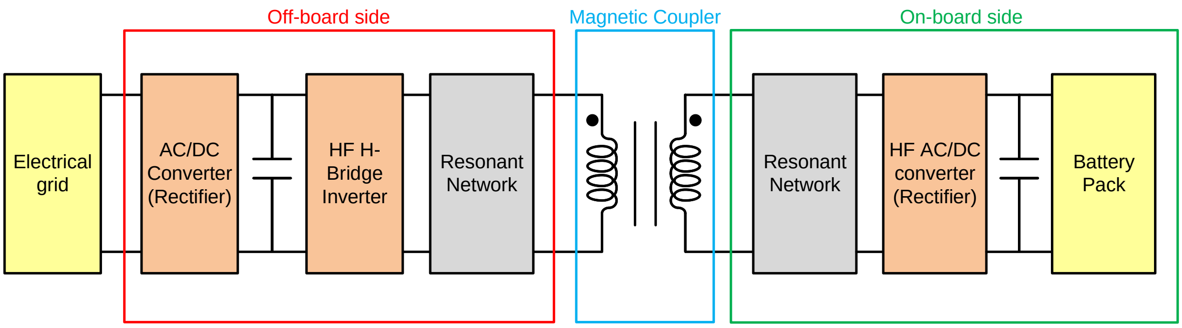


Figure 1.4: Overview of a typical IPT system with its main components [27].

reservoir capacitor to achieve an output signal as constant as possible. Furthermore, it is followed by a HF H-bridge inverter which changes DC to AC, regulating the output frequency to conventional IPT frequency values (10 kHz to 100 kHz). These IPT systems [28] operate at a frequency ranging from 79 kHz to 90 kHz (standard frequency of 85 kHz) according to the SAEJ2954 standard. Subsequently, there's a resonant compensation network and the transmitter pad of the MC.

On the on-board side, it includes the receiver pad of the MC, a resonant compensation, an HF AC-DC converter, and the battery pack.

### 1.2.3 Resonant topologies

Resonant compensation systems are not a new concept and have been used in electric power systems for power factor correction (PFC) or transmission line compensation. In the case of IPT systems, the compensation of the reactive component is done to allow the maximum transfer of power (active power). To properly design an IPT system, it is necessary to know the type and level of compensation to be used. There are two basic types of compensation [7]: series and parallel. In series compensation, a capacitor is placed in series with the leakage inductance of the transmitter and/or receiver. In the case of parallel compensation, the capacitor is placed in parallel with the transmitter

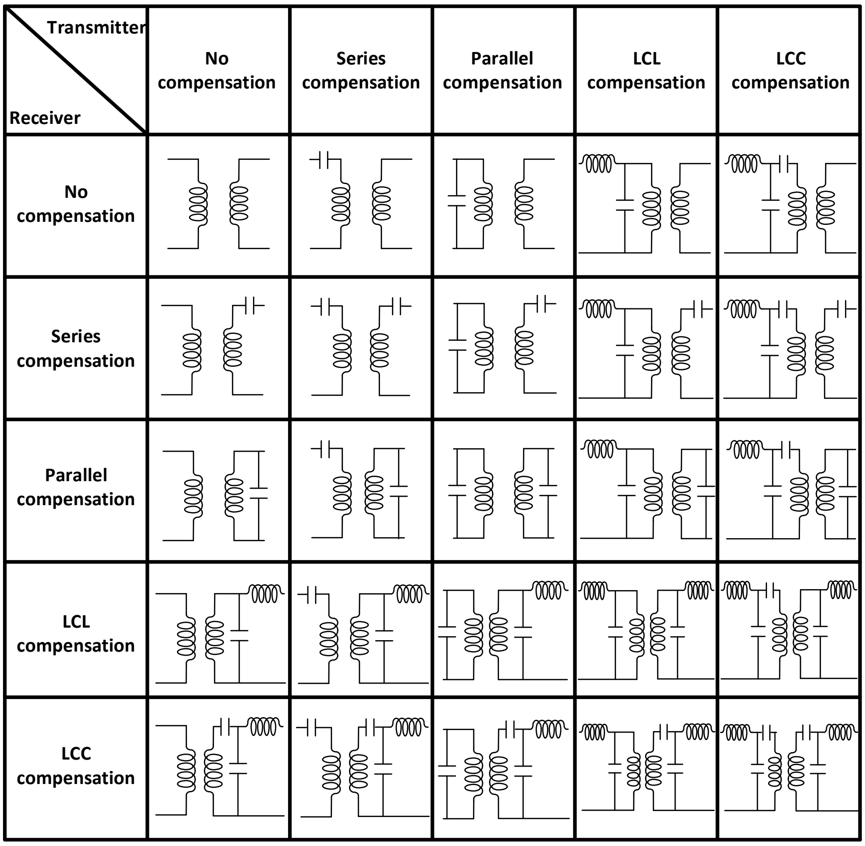


Figure 1.5: Different IPT compensation topologies.

and/or receiver. Moreover, there is an option to incorporate an additional inductor at the start of either the transmitter or receiver side, resulting in what is known as LCL compensation and a capacitor can be introduced in series with the inductance of the transmitter and/or receiver, presenting the LCC compensation. The LCL and LCC hybrid topologies [7] are designed to enhance the efficiency of power transfer and improve the overall performance of the IPT system. Fig. 1.5 demonstrates the different compensation topologies possible for the IPT systems.

These resonant configurations must be chosen according to the following requirements to a given application and its suitability [7]:

- Minimum VA rating: Compensating for the leakage inductance of the transmitter results in a higher power factor, while the receiver coil continues to operate in a similar resonant configuration.
- Maximum power transfer: Each compensation network circuit is designed to operate at resonance, meaning that the filter natural frequency $f_0$ is equal to the inverter switching frequency $f_s$. At resonance, the system is operating on the condition of the highest power transfer.
- Constant current (CC) or constant voltage (CV): Differs according to the application, the system should operate in CC or CV.
- High efficiency: The efficiency of the system is highly dependent on several factors, including the quality factor of the coils, coupling coefficient and soft-switching of the inverter. For achieving soft-switching or minimum losses in the inverter, the decision of the suitable resonant configuration is relevant.
- Displacement tolerance: To ensure the power transfer requirements are met when the coupling values are low, either the power supply's VA rating needs to be surpassed or the inverter risks losing its soft-switching operation due to bifurcation. Bifurcation is when multiple zero phase angle (ZPA) resonant frequencies occur, causing the impedance at the inverter terminals to suddenly switch from capacitive to inductive, depending on the receiver's quality factors. The resonant configuration affects the input impedance of the system.
- Control of the transmitted power through frequency: Based on the control of the inverter frequency.

### 1.2.4 Static and dynamic IPT operation

IPT systems enable wireless power transfer using magnetic fields, supporting both stationary and mobile applications depending on the needs of the user and the complexity of the system. Therefore, these charging systems are divided into two modes: static IPT (SIPT) and dynamic IPT (DIPT). In SIPT, these systems allow convenient charging

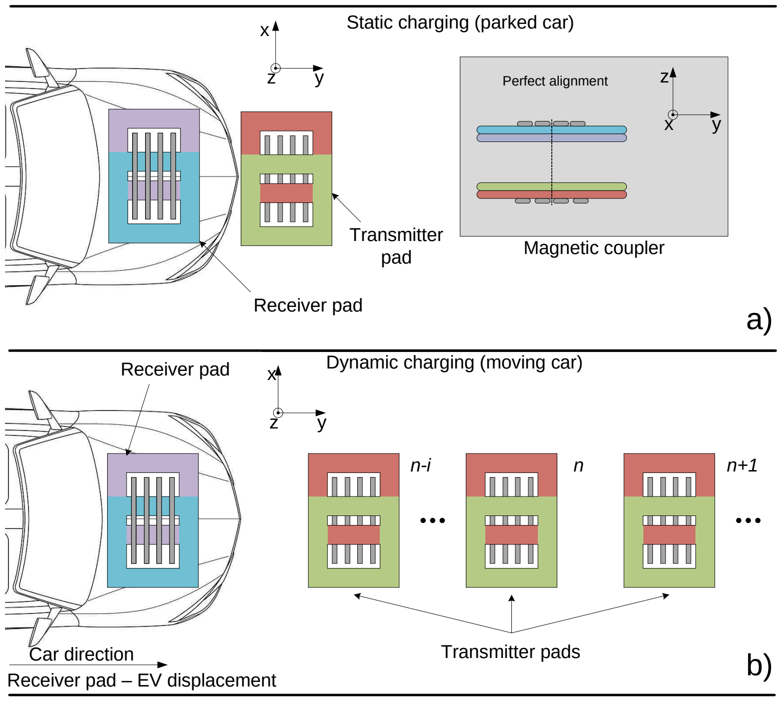


Figure 1.6: Comparison of IPT systems for (a) Static and (b) dynamic charging applications [27].

across small air gap of electronic devices, EVs and other end user applications. Alternatively, DIPT systems enable wireless charging based on vehicle movement during the charging process. The primary objective of SIPT is to achieve maximum power transfer for a particular range of load variation while maintaining constant coupling. This is achieved by charging the battery in either CC or CV mode from State of Charge (SoC) $SoC_{min}$ to $SoC_{max}$. Even with slight misalignments, optimal power transfer can be achieved, as noted in [29]. Fig. 1.6 (a) illustrates the SIPT process to charge a vehicle and the position of the pads.

On the other hand, DIPT [30, 27] allows for charging while the EV is in motion, reducing the charging time and eliminating range anxiety associated with EVs. Coupling variations are expected due to the EV's inherent movement, resulting in unpredictable SoC levels that can affect the converter's power transfer, though the coupling variations can impact the power transfer. The DIPT charging infrastructure allows for almost unlimited cruising while minimizing the size and cost of the on-board battery pack. The authors in [27] have explored the use of single elongated off-board transmitters compared to several individual off-board transmitters. In summary, long pads have advantages in construction cost, control, and power transfer. They provide a constant power transfer and coupling factor. However, they also have drawbacks such as leakage magnetic fields, iron and joule losses, and a low coupling factor. On the other hand, segmented pads offer better system efficiency, a higher coupling factor, and easy system replacement. Nevertheless, it is important to consider the disadvantages of increased system costs and control complexity for this type. As shown in Fig. 1.6 (b), using multiple transmitter pads in a DIPT configuration can enhance energy management. However, each pad must be energized separately as the moving EV approaches, which increases the system complexity.

In general, DIPT [6] presents additional challenges regarding to Static IPT (SIPT), among them, the choice of pad topology (elongated or segmented and different pad geometry), vehicle displacement due to inherent vehicle movement, air gap and lateral or vertical displacements and EV speed, leading to different coupling conditions (no-coupling to full-coupling). The technology is still in development, but it has the potential to change the EV industry by allowing longer driving ranges and eliminating the need for frequent stops to recharge.

Therefore, different studies of IPT systems and its variants are made to minimize the overall problems of IPT systems and enhance their system efficency. One example of these studies is a double coupling IPT partially embedded in the wheel (inWIPT) that allows transferring energy between the off-board side (road) to the wheel and from the wheel to the on-board side (vehicle). The inWIPT concept is presented in [31], and tries to mitigate the impact of the air gap between the off-board transmitter pad and the on-board receiver pad by maintaining a lower air gap and almost independent of the vehicle. The system uses the wheel as an intermediary stage to transfer energy through two consecutive MCs. In addition to the existing transmitter (off-board side) and receiver (on-board side) resonant configuration networks, a third resonant compensation network is included between the two MCs (wheel side). The work that will be presented is related with this in-wheel concept. An early mention of inWIPT technology was made in [30], where the authors envisioned the placement of several receiver coils in the rubber surface inside the tire. A drawback in the proposed work is the use of slip rings to transfer the DC bus from the wheel to the vehicle side. The low reliability and high maintenance of carbon brushes make it an undesired solution. Furthermore, the placement of converters inside the tire makes them more prone to mechanical shocks.

Embedded in-wheel systems started with the idea of in-wheel motors (IWM). In 1884, the concept of IWM [32], also known as hub motors, was first introduced in this field of EVs and consist of a type of electric motor that is placed directly inside the wheel hub of a vehicle to optimize their efficiency. They offer a number of advantages over traditional motors, including increased efficiency, simplified drivetrain design (by eliminating the transmission system and power losses), improved vehicle handling and more space. These systems can be used in both electric and hybrid vehicles, and are becoming increasingly popular as the demand for more efficient and eco-friendly transportation options grows.

Fig. 1.7 [33] illustrates a simple block diagram of an IMW system in an EV. Firstly, at the core of the system is the IMW itself, which is located directly inside the vehicle's wheel hub. This motor is responsible for converting electrical energy stored in the vehicle's battery into rotational energy that powers the wheel. The IWM is connected to a control unit, which regulates the flow of electricity to the motor and controls the working operation to ensure efficiency and safety. The IWM system also includes a battery management system (BMS), which is responsible for managing the charging and discharging of the vehicle battery. Finally, the IWM system may include additional components, such as regenerative braking systems, which capture energy from the vehicle's motion and convert it back into electrical energy to recharge the battery. The system may also include sensors and control algorithms to optimize vehicle performance and efficiency.

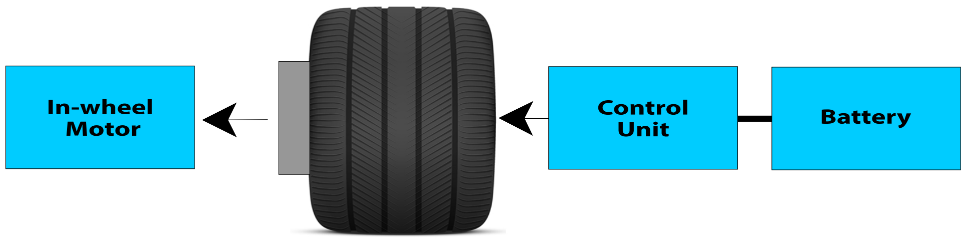


Figure 1.7: Overview of a typical IWM system with its main components [33].

According to a review paper [33], there are four major topologies for these kinds of systems. In particular, a topology called wireless in-wheel motor (WIWM) [34] is introduced to overcome the main issues that exist in conventional EV and IWM vehicles such as the electric hazard risks of conventional power cord battery chargers. These systems are operating under different and harsh weather and environments conditions and it is possible to compromise the integrity of the system by disconnecting due to vibrations and high acceleration. However, there are issues to take into account due to complexity of IWMs control using in-motion WPT. One of them are the misalignment of MC generates fluctuations in voltage applied to the receiver. Therefore [34], it is used a novel hysteresis control to maintain a desired value of DC link voltage, if provided that adequate power is conveyed from the primary side to the secondary side. The inverter output power is estimated by the alternative proposed method and applied to a feed forward controller to maintain a constant voltage across the secondary DC link. The effectiveness of the proposed control methods was validated by the results of the bench tests conducted on the trial unit, demonstrating high efficiency (between 90 and 95 %) in both motor powering and energy regeneration.

In addition, another WIWM system [35] is proposed to solve problems in motion operation for EVs. This proposed system uses a mutual inductance S-S topology model to transfer the power through tyre and wheel and using IWM. A full-scale model is tested to reduce the possibility to foreign objects entering into between the MC and it is achieved the efficiency of 97.7 % with an arc-shaped coil and the minimum error of $\pm$ 5 % between the calculations and the measurements made with a small and full scale model.

## 1.3 Motivation and objectives

As evidenced in the aforementioned sub-chapters, IPT systems plays an important role in the integration of a wide range of applications, namely in the battery charging of EVs. The design and construction of the IPT system represents a key parameter for achieving good results in terms of energy transfer, tolerance to horizontal and lateral misalignments, and high efficiency. Therefore, the work presented in this master's thesis is done under the inWIPT concept, which uses the wheel as an intermediary stage between the off-board and the on-board sides of the vehicle. In this way, the air gap distance between the transmitter and receiver pads of the MC is minimal and independent of vehicle class. The S-S-S resonant compensation solution already developed for the static inWIPT application cannot be used for the dynamic mode due to inherent displacements and misalignments, which leads to different coupling conditions and consequently, results in high transmitter voltage and current values. This would naturally endanger the power electronic converter that feeds the primary transmitter pad. As a result, charging EVs in motion requires the study of alternative strategies for DIPT operation and several studies introduced the use of LCL and LCC resonant compensation networks, which presents a natural current limiting behaviour and is well-known for conventional IPT systems [36, 7, 37].

In this context, the main objectives of this master's work were:

- Survey and bibliographic review of conventional and alternative variants of IPT systems for static vs dynamic charging, including the investigation of new methods to improve the dynamic mode performance of the novel inWIPT concept such as:
  - Investigation of new resonant compensations to assess the applicability of the proposed system.
- Analysis of the selected resonant configurations (S-S-S, LCL-S-S and LCC-S-S) involving:
  - Circuital analysis including the equivalent mathematical model and transfer functions;
  - Analysis of the behaviour of different resonant configurations by creating graphs with specific variables and conduct a comprehensive evaluation of their inherent characteristics.

  - Validation of the mathematical equations comparing theoretical and simulated results using the fundamental harmonic component and square wave signal as power feeding signals, using MATLAB/Simulink software.
  - Collaboration in the experimental testing with a prototype using LCL-S-S resonant power converter to validate the previous work.
- Experimental implementation and characterization of different magnetic geometries to analyse its behaviour for the experimental prototype.
  - Construction of the prototype to validate the MCs behavioural analysis under the mentioned conditions;
  - MC characterization in terms of self and mutual inductances and coupling factors, considering the impact of the space between turns, number of turns, volume of core and air gap, as well as vertical and lateral displacements and wheel's rotation;
  - Data measurement of the experimental MC characterization and analysis of the results.
- Contribute to the dissemination of the collected data and acquired knowledge in alignment with a project supported by Instituto de Telecomunicações, Project inWheel Inductive Power Charging for Sustainable Mobility with reference 2022.06192.PTDC. (Master project, papers in conference).

This master's work starts with an overview of WPT and IPT systems in Chapter I. In IPT systems, the practical real-world applications, the basic setup of these systems, resonant topologies and static and dynamic operations are introduced. Moreover, a novel technology named in-wheel motor (IWM) are demonstrated for the traction of vehicles. Chapter II addresses the fundamentals of IPT systems, comprised of electromagnetic concepts, magnetic coupling experimental calculations, measurements and magnetic coupling systems with two coils and variants to the conventional IPT systems such as multiple coupling IPT systems. Chapter III presents the theoretical analysis of the S-S-S, LCL-S-S and LCC-S-S resonant configurations, including the equivalent mathematical model, transfer functions and the comparison of different parameters for DIPT operation. Furthermore, Chapter IV approaches the validation of the mathematical equations comparing theoretical and simulated under different conditions using MATLAB/Simulink software. In addition, an experimental analysis using LCL-S-S topology is presented to corroborate with the previous work. Chapter V demonstrates the characterization of different integrated pad geometries for in-Wheel EV IPT applications and an experimental prototype is built to validate the MC behavioural analysis under different conditions. Lastly, the main conclusions are summarized in the last chapter.

# 2 Single and multiple coupling in IPT systems

The impact of magnetic induction has been the subject of study in the last century with numerous applications. The development of semiconductors with high switching frequencies has enabled the creation of energy transmission systems with large air gap and high efficiency. The operating method of an IPT system is similar to that of a transformer, with the main difference in the air gap value between primary and secondary. The lack of contact between the two parts of the system makes it suitable for safe and efficient energy transfer in different environments, while also ensuring galvanic isolation between the two parts of the system.

This chapter presents the basic working principles of IPT systems in static and dynamic mode, showing the fundamental electromagnetic equations and the main electromagnetic concepts in two-coil systems. Additionally, different variants of these systems are presented, including the inWIPT system which is a multiple coupling IPT.

## 2.1 Mutual inductance and coupling factor

The IPT systems are based on [38] two fundamental principles: Ampère's law, also known as the fourth Maxwell equation, and Faraday's law, which was derived by the second Maxwell equation. According to the Ampère's law (2.1), a product of the current $I$ passing through a loop and the permeability of free space $\mu_o$ generates a magnetic field around a closed loop $B$ .

$$\oint \vec{B}.\, d\vec{s} = \mu_o.I \tag{2.1}$$

The Faraday's law (2.2) states that when there is a change in the magnetic field through a loop of wire, a voltage is induced in that loop of wire. The magnitude of the induced voltage $e$ is proportional to the rate of change of the magnetic field $\Phi$ composed, optionally, of $N$ identical turns in the case of a coil. In addition, Lenz's law (minus sign) affirms that the direction of the induced voltage in a closed loop is such that it produces a current that creates a magnetic field that opposes the original change in the magnetic flux.

$$e = \oint \vec{E}.\, d\vec{l} = -N.\frac{d\Phi}{dt} \tag{2.2}$$

A single coil [38] can create his own flux if a current is passed through the coil, this current will generate its own magnetic field $B$, which will create a magnetic flux $\Phi$ that is linked to the coil. Therefore, flux $\Phi$ (2.3) is proportional of the product of current

$I$ and the self-inductance $L$. Additionally, $L$ can be expressed (2.4) as a ratio of the differential change in the flux linkages to the differential change in the current.

$$\Phi = L.I \tag{2.3}$$

$$L = N\frac{d\Phi}{di} \tag{2.4}$$

Using Ampère's law and the Biot-Savart's law, $L$ can be expressed as (2.5)

$$L = \frac{N^2 \mu_0 A}{l} \tag{2.5}$$

where this quantity depends on the geometric, $N$, the cross section $S$ and the coil length $l$.

Alternatively [38], if there are two coils that are close enough to induce a voltage on each other, similar what happens in a IPT system and illustrated in Fig. 2.1.

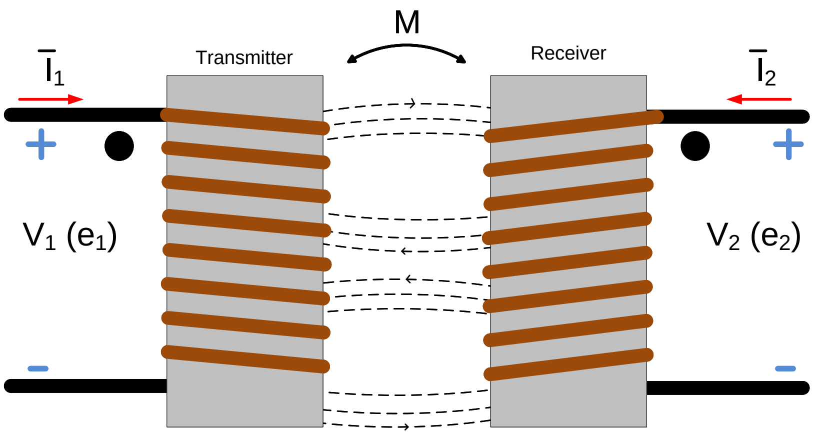


Figure 2.1: General representation of coupled inductors [38].

In this case, there is a magnetic connection between the two circuits and this connection (2.6) will have a self-inductance part, proportional to the current flowing in that circuit, and a mutual inductance part, proportional to the current flowing in the other circuit.

$$\begin{cases} \Phi_1 = L_1.I_1 + M_{21}.I_2 \\ \Phi_2 = M_{12}.I_2 + L_2.I_2 \end{cases} \tag{2.6}$$

The voltages at the terminals of both circuits are presented in (2.7)

$$\begin{cases} e_1 = \frac{d\Phi_1}{dt} = L_1.\frac{dI_1}{dt} + M_{21}.\frac{dI_2}{dt} = L_1.\frac{d\Phi 1}{dI1} \pm N_2.\frac{d\Phi_{21}}{dI2} \\ e_2 = \frac{d\Phi_2}{dt} = M_{12}.\frac{dI_1}{dt} + L_2.\frac{dI_2}{dt} = L_2.\frac{d\Phi 2}{dI2} \pm N_1.\frac{d\Phi_{12}}{dI1} \end{cases} \tag{2.7}$$

where ($\Phi_{12} = k_1\Phi_1$) and ($\Phi_{21} = k_2\Phi_2$) represent the flux linkage between transmitter and receiver windings and the flux linkage receiver and transmitter windings, respectively. The above expressions can be simplified if we consider ($M_{12} = M_{21} = M$) and ($k = \sqrt{k_1 k_2}$) , where $M$ is the mutual inductance of the system and $k$ is the coupling factor, (2.8) expressed by

$$M = k\sqrt{L_1 L_2} \tag{2.8}$$

$$k = \frac{M}{\sqrt{L_1 L_2}} \tag{2.9}$$

where $L_1$ and $L_2$ are the self-inductance values of the transmitter and receiver coils and $M$ is the mutual inductance. The subscript number in the variables denotes the associated side, with 1 referring to the transmitter and 2 to the receiver.

The coupling coefficient variable $k$ is a dimensionless quantity that quantifies the magnetic link between both pads, ranging from 0 to 1, where 0 indicates no-coupling between the two coils, and 1 indicates perfect coupling. The coupling factor depends on the geometry of the coils and the relative orientation of their magnetic fields.

## 2.2 Magnetic coupling systems with two-coils

WPT between the transmitter and receiver coils in IPT systems is made possible by the essential component of the MC. The MC consists of transmitter and receiver pads, each with one or more coils, a ferromagnetic core, and an optional shield. This coupler is a transformer with loose coupling between its components.

The open and short-circuit tests shown in Fig. 2.2 are used to determine the self and mutual inductance values and power transfer capabilities of a MC. During the open-circuit test [27, 39], the transmitter coil is supplied with the nominal current ($\overline{I}_1$) while the receiver coil remains open. In the short-circuit test, the receiver coil is shunted and the transmitter coil is supplied with the nominal current of the transmitter pad.

$$\overline{V}_{oc} = j.\omega.M.\overline{I}_1 \tag{2.10}$$

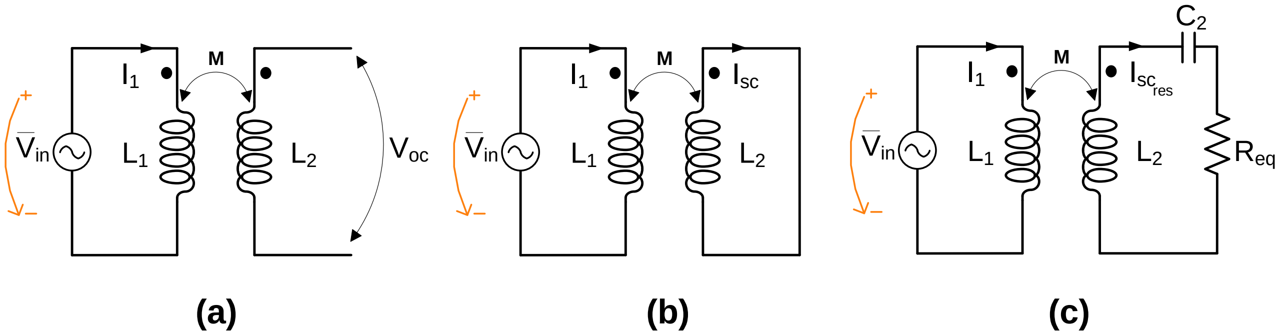


Figure 2.2: (a) Open-circuit test, (b) short-circuit test and (c) resonant capacitor scheme [27, 39].

$$\overline{I}_{sc} = \frac{\overline{V}_{oc}}{j.\omega.L_2} = \frac{M.\overline{I}_1}{L_2} \tag{2.11}$$

$$\overline{I}_{sc_{res}} = \frac{\overline{V}_{oc}}{R_{eq} + j.(\omega.L_2 - 1/\omega.C_2)} = \frac{M.\overline{I}_1}{L_2} = j\frac{M.\omega.I_1}{R_{eq}} \tag{2.12}$$

Under the assumption of a lossless circuit [27, 39], the uncompensated power ($P_{su}$) of the MC can be calculated as the product of the root mean square (RMS) open-circuit voltage test ($|\overline{V}_{oc}|$) and the RMS short-circuit current test ($|\overline{I}_{sc}|$) described in (2.10) and (2.11), respectively. This variable represents the power that is dissipated in the system due to its reactive components, such as the inductance and capacitance. In (2.13), it is possible to verify that the uncompensated power $P_{su}$ is dependent on the coefficient $M^2/L_2$, both magnetic parameters. Although, using a resonant tank, the new compensated power ($P_{sc}$) can be calculated as the product of the RMS open-circuit voltage test ($|\overline{V}_{oc}|$) and the new RMS short-circuit current test ($|\overline{I}_{sc_{res}}|$) described in (2.10) and (2.12), respectively. In (2.14), the mentioned power is demonstrated.

$$P_{su} = \overline{V}_{oc}.\overline{I}_{sc} = j.\omega.I_1^2.\frac{M^2}{L_2} \tag{2.13}$$

$$P_{sc} = \overline{V}_{oc}.\overline{I}_{sc_{res}} = \frac{\omega^2.M^2.I_1^2}{R_{eq}} = P_{su}.\frac{\omega.L_2}{R_{eq}} = P_{su}.Q \tag{2.14}$$

In (2.14) [27, 39], a new variable defined by quality factor (Q) is presented. Q of an IPT system corresponds to the ratio between reactive power and active power. Q is a crucial parameter for efficient IPT power transfer, measuring the energy stored in the resonant tank circuit compared to the energy dissipated. Greater Q factors indicate a higher amount of energy stored in the resonant tank circuit compared to the dissipated energy, resulting in more efficient power transfer. The output power ($P_{out}$) corresponds to the product of $P_{su}$ with the load quality factor ($Q$), as show in

$$P_{out} = P_{su}.Q = |\overline{V}_{oc}|.|\overline{I}_{sc}|.Q = \omega.k^2.L_1.|\overline{I}_1|^2.Q. \tag{2.15}$$

$P_{out}$ of an IPT system refers to the amount of power that can be transferred contactless from the transmitter to the receiver coils.

## 2.3 Multiple coupling IPT systems

The coupling [39] between the transmitter and receiver sides plays a critical role in determining the efficiency of IPT systems. This is particularly important in systems with significant vertical and lateral displacements. The use of multi-coil resonators or intermediate couplers (IC) (auxiliary couplers) and multiple MCs can boost the coupling coefficient between the pads. Different solutions are presented using these techniques for IPT systems with both static and dynamic capabilities. Fig 2.3 exemplifies a multiple

MC generic configuration of an IPT.

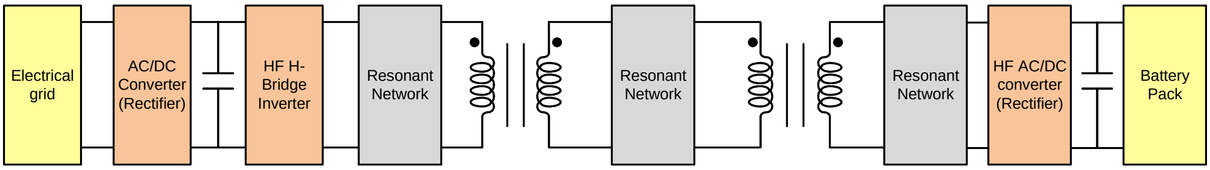


Figure 2.3: Equivalent generic circuit of a multiple coupling system [39].

The article [40] compares the energy efficiency of two and three-coil S-S resonant topology systems. The authors found that the three-coil system has higher energy efficiency, a reduced current stress, and lower leakage field emissions caused by misalignments. Additionally, the three-coil system is found to have energy efficiency stiffness against load variations.

In [41], the authors investigate the efficiency of power transmission between the two and three-coil systems. The authors show for a better efficiency, these systems should have a symmetric structure and for load variation effect, both systems are not robust. Although, for higher load resistor, the three-coil IPT system is more optimal.

Furthermore, one of the systems proposed in [42] presents a new roadway IPT system. The system includes an elongated primary pad, ground pads, and an IC circuit that allows independent control of individual charging sections on the road. It also provides isolation between the power supply and the charging sections. The authors tested the system at 20 kHz and achieved an efficiency of 92.5 % at an output power of 5 kW. The system can operate with a frequency changing capability between the power supply primary track and each ground transmitter pad, including 85 kHz of international guidelines.

On the subject of multiple coupling, the authors in [43] proposed a system to power multiple loads using a various S-LCL configuration. This system ensures CC in load-independent operation (LIO) with an experimental setup with 10 loads and a maximum efficiency of 84 %. Article [44] analyses IPT systems using multiple magnetic couplings and finds that the proposed multiple coupling system achieves higher power transfer efficiency and lower magnetic field emissions, especially at larger distances between the transmitter and receiver. The authors demonstrate the highest values of power transferred to the load using four coils connected in series with three magnetic couplings.

The authors in [31, 45] presented a new double coupling inWIPT. Such approach follows the trend line of moving the powertrain from the vehicle into the wheels [46]. The development of new airless tyre designs like the Uptis model from Michelin with non-magnetic materials strengthens the applicability of inWIPT. These new airless tyre designs also eliminate the risk of pressure increase in the tyre caused by the Joule losses in the receiver coils placed within the tyre. In addition, the aluminium rim shields the leakage flux lines above the receiver coils and avoids the use of additional shielding material. The system uses the wheel as an intermediary stage to transfer energy through two consecutive MCs. The impact of the air gap between the off-board transmitter pad and the on-board receiver pad is mitigated by maintaining a lower air gap and almost independent of the vehicle. In addition to the existing transmitter (off-board side) and receiver (on-board side) resonant configuration networks, a third resonant compensation network is included between the two MCs (wheel side). Furthermore, the use of aluminium rims in inWIPT systems limits the magnetic stray fields and avoids the use of additional shielding in the vehicle side.

Fig. 2.4 [31, 45] illustrates the proposed double coupling inWIPT system and presents the placement of the pad on the off-board (roadway), wheel and on-board (vehicle) sides. The first MC (Fig. 2.4 (a)) is referred in this work as Outer Rim Magnetic Coupler (ORMC), transferring power from the off-board transmitter pad, placed on the roadway, to the receiver pad, placed in the outer side of the rim and inside the tyre. The second MC (Fig. 2.4 (b)) is referred as Inner Rim Magnetic Coupler (IRMC), which transfers power from the transmitter pad, placed in the inner side of the rim, to the receiver pad fixed in the wheel hub (on-board side). In addition, an aluminium enclosure [45] is used to block the leakage flux between IRMC pads and both ORMC and IRMC coils to remain decoupled from one another, and protecting against the outside intrusion such as water and dust. The IRMC design has a cylindrical hollow shape (solenoid geometry) in order to be incorporated between the breaking system of the vehicle and the inner side of the rim. In such conditions, the IRMC air gap offers a constant coupling profile and independent for any rotary position regardless of the relative positioning between the transmitter and receiver pads. The cylindrical design required for the ORMC receiver pad and IRMC modifies the coupling profiles of traditional IPT geometry pads. In addition, the impact of the new degree of freedom introduced by the wheel's rotation depends on the pad geometry.

In an earlier version of the work presented here regarding solely the selection of reso-

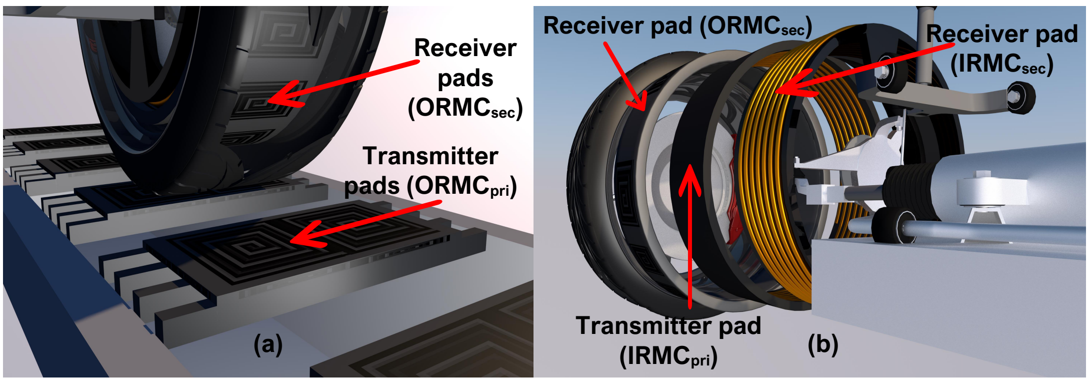


Figure 2.4: 3D overview of the ORMC and IRMC placement on the roadway and wheel's hub for the inWIPT system (a) ORMC and (b) IRMC [31, 45].

nant compensation networks, the authors [31, 45] analysed series-series-series (S-S-S) or series-series-parallel (S-S-P) resonant power converter where three capacitors are added in series with the MC coils, and the first two added in series and the last in parallel, respectively and one for each compensation mesh. It was found that S-S-S topology configuration exhibits CV mode with LIO charging characteristic and CC mode with LIO in S-S-P, both at resonance condition. The S-S-S configuration limits the transmitter current under no load conditions, unlike the series-series (S-S) configuration in conventional IPT systems. Nonetheless, a no-coupling condition in the first MC results in high transmitter currents, making them undesirable for DIPT applications. Consequently, for charging EVs in motion, news strategies are required to prevent these type of situations. In the following chapters, an evaluation of different compensation networks is done in order to safeguard adequate converter operation. This evaluation was made in different steps, first a theoretical mathematic approach with circuital analysis, then simulation and finally some experimental validation.

# 3 Double coupling system

In this chapter, a detailed explanation of inWIPT system and theoretical circuit analysis of the LCL-S-S and LCC-S-S topologies (hybrid topologies) are presented considering dynamic operation, taking into account the analysis of the S-S-S base topology. Furthermore, a comparative analysis of the different gain functions and input impedance was made to assess the intrinsic characteristics of each resonant configuration. In addition, an analysis of the behaviour of the resonant configurations was made by assessing graphics under dynamic operation and it is conducted a comprehensive evaluation of their inherent characteristics.

## 3.1 inWIPT system

An electrical circuit schematic of a double coupling inWIPT system is presented in Fig. 3.1. Two MCs allow the power transfer from the charging station (Off-board side) to the vehicle (On-board side) via the wheel. The off-board side consists of an HF inverter, supplied by a DC bus, and connected to the transmitter pad of the first MC via a resonant compensation network. The wheel side comprises the receiver pad of the first MC, which is referred to in this work as ORMC, and the transmitter pad of the second MC, which is referred to in this work as IRMC electrically connected by a resonant compensation network. The on-board side includes the receiver pad of the second MC connected to a resonant compensation network, followed by a H-bridge rectifier and the battery bank.

Fig. 3.2 represents the general equivalent circuit model of the proposed inWIPT system, using the aforementioned resonant compensations for its analysis. For analysis

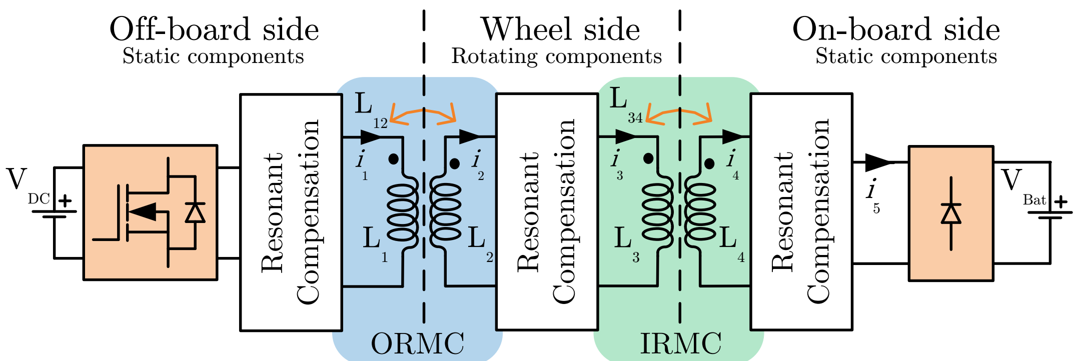


Figure 3.1: Block diagram of a double coupling inWIPT system [45].

purposes, the first harmonic approximation (FHA) is used (the output of the full wave inverter is replaced by a sinusoidal source with its fundamental component ($\overline{V}_{in}$)). The root mean square (RMS) of the input voltage ($|\overline{V}_{in}|$) of the inverter, at the fundamental harmonic, can then be described as a function of the phase shift (PHS) control angle ($\alpha$) using

$$|\overline{V}_{in}| = V_{DC}\frac{2\sqrt{2}}{\pi}cos(\frac{\alpha}{2}), \tag{3.1}$$

where $V_{DC}$ is the average DC link voltage.

The two mentioned MCs are modeled considering dependent voltage sources and circuit impedances as show in Fig. 3.2 and are defined by

$$\overline{V}_{12} = j.\omega.L_{12}.\overline{I}_1, \overline{V}_{21} = -j.\omega.L_{12}.\overline{I}_2 \tag{3.2}$$

$$\overline{V}_{34} = j.\omega.L_{34}.\overline{I}_2, \overline{V}_{43} = -j.\omega.L_{34}.\overline{I}_4 \tag{3.3}$$

where $\overline{V}_{12}$ and $\overline{V}_{21}$ are the reflected voltage from the ORMC transmitter side mesh onto

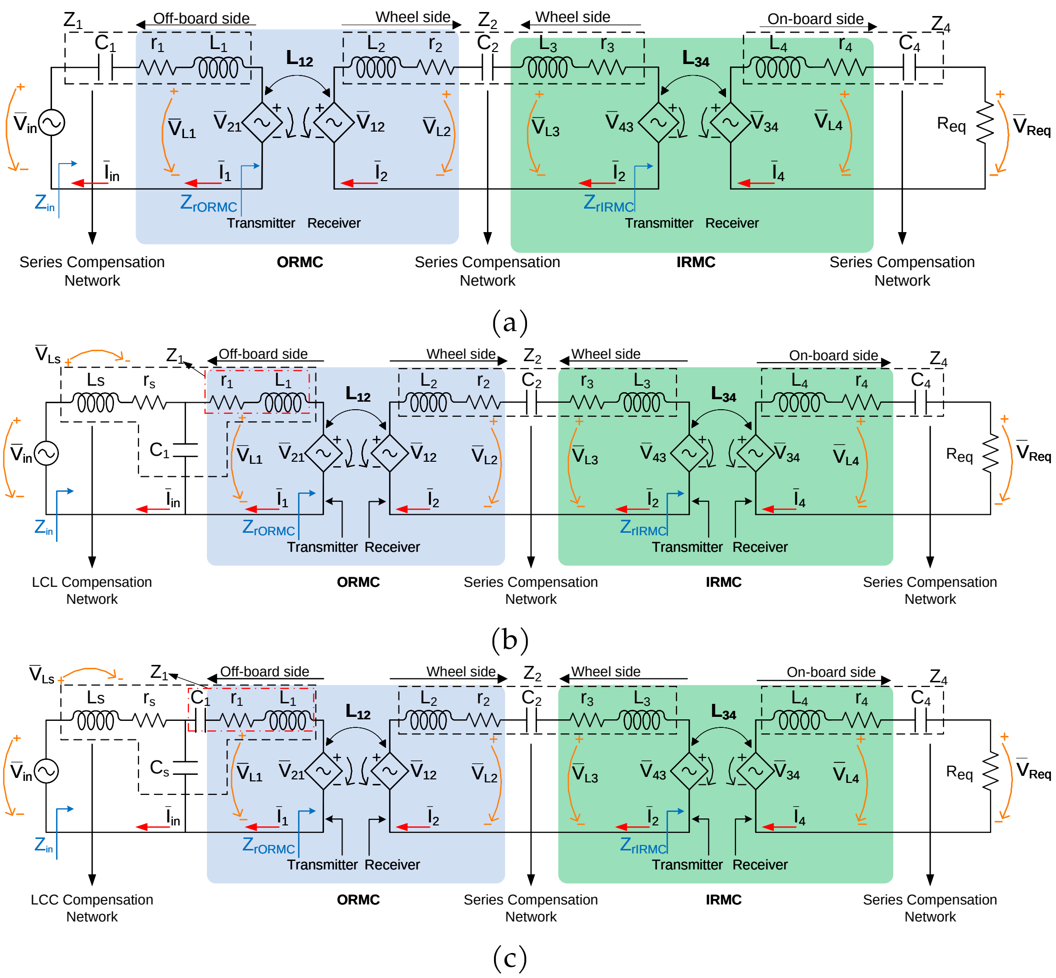


Figure 3.2: Equivalent circuit model for double coupling inWIPT for: (a) S-S-S topology, (b) LCL-S-S topology and (c) LCC-S-S topology.

the ORMC receiver side mesh and the reflected voltage from the ORMC receiver side mesh onto the ORMC transmitter side mesh, respectively. On the other hand, $\overline{V}_{34}$ and $\overline{V}_{43}$ represent the same for IRMC.

Each compensation network circuit is designed to operate under resonance, meaning that the filter natural frequency $f_0$ is equal to the inverter switching frequency $f_s$, therefore the natural angular frequency $\omega_0$ is also equal to the inverter switching angular frequency $\omega$ (where $\omega_0 = 2.\pi.f_0$ and $\omega = 2.\pi.f_s$). As a result, the imaginary part of the input impedance $Z_{in}$ is zero, thus the load viewed from the input behaves linearly. When the converter operates under resonance, maximum power transferring capability is achieved, leading to higher overall efficiency. Operating under resonance leads to $\overline{I}_1$, $\overline{I}_2$, $\overline{I}_3$ and $\overline{I}_4$ having a sinusoidal waveform although the converter is fed by a square wave voltage. This implies that only the fundamental component of the input voltage $\overline{V}_{in}$ is responsible for the power transfer to the equivalent load, as a result the design is typically done using FHA. Taking account into the mentioned information, the compensation networks like S-S-S, LCL-S-S and LCC-S-S are addressed in this work to study them in resonance mode, in order to evaluate their intrinsic characteristics and advantages.

According to Fig 3.2, the three circuits with different resonant compensations are under analysis for DIPT operation. These circuits are comprised by: $L_1$ and $L_2$ are the self-inductances of the ORMC and, $L_3$ and $L_4$ are the self-inductances of the IRMC and, $L_{12}$ and $L_{34}$ correspond to the mutual inductances of the ORMC and IRMC, respectively. The LCL-S-S and LCC-S-S resonant configurations add the inductor $L_s$, which is the self-inductance on the input side illustrated in Fig 3.2 (b) and (c). The subscript numbers in the variables indicate to which side the variable is related. The subscript letter s represents the input inductor placed after the voltage source to form the LCL-S-S and also placing the capacitor $C_s$ to form the LCC-S-S resonant tank presented in Fig 3.2 (b) and (c), respectively. The parameters $r_s$, $r_1$, $r_2$, $r_3$ and $r_4$ denote the equivalent resistance of the input series inductor $L_s$ and of each transmitter and receiver coil of the ORMC and IRMC, respectively, and include Joule and iron losses (if applicable).

In these circuits, the different meshes incorporate resonant tanks represented by the elements $L_x$ and $C_x$, containing distinct angular resonant frequencies, $\omega_s$, $\omega_1$, $\omega_2$, $\omega_4$. When these specified parameters are interconnected, they are denoted $Z_1$, $Z_2$, and $Z_4$, designated by the equivalent impedances of the resonant tanks on the transmitter, wheel and receiver sides, respectively. Furthermore, the concept of reflected impedance in IPT systems refers to the equivalent impedance of one side seen at the terminals of the opposite pad. Therefore, the proposed circuits have two reflected impedances named $Z_{r_{IRMC}}$ and $Z_{r_{ORMC}}$ and an equivalent impedance seen by the power source $Z_{in}$, as illustrated in Fig 3.2. The $Z_{r_{IRMC}}$ consists of the reflected impedance from the the on-board side onto the wheel side, while the $Z_{r_{ORMC}}$ is the reflected impedance from the wheel side onto the off-board side.

Moreover, at the output of these circuits, the variable $R_{eq}$ is the equivalent resistance of the batteries $(R_{bat})$ before rectifier action and it is given by

$$R_{eq} = \frac{8.R_{bat}}{\pi^2} = \frac{8.V_{bat}}{\pi^2.I_{bat}}, \tag{3.4}$$

where $V_{bat}$ and $I_{bat}$ are the voltage and current values in the batteries, respectively and assuming an output filter capacitor between the rectifier and the batteries. For mathematical purposes, we assume the equivalent resistance of the batteries before the rectifier action $R_{eq}$.

Existing regulations limit the induced voltages across the IRMC and ORMC coils to 1000 $V_{rms}$ in Europe and 400 $V_{rms}$ in Asia [47]. The use of capacitors in series with the coils surpasses these limitations, but at the cost of additional components. The induced voltages across the coils are expressed by

$$|\overline{V}_{L_s}| = |\overline{I}_{in}.(r_s + j.\omega.L_s)| \tag{3.5}$$

$$|\overline{V}_{L_1}| = |\overline{I}_1.(r_1 + j.\omega.L_1 + Z_{r_{ORMC}})| \tag{3.6}$$

$$|\overline{V}_{L_2}| = |\overline{I}_2.(r_2 + j.\omega.L_3 + 1/(j.\omega.C_2) + Z_{r_{IRMC}})| \tag{3.7}$$

$$|\overline{V}_{L_3}| = |\overline{I}_2.(r_3 + j.\omega.L_3 + Z_{r_{IRMC}})| \tag{3.8}$$

$$|\overline{V}_{L_4}| = |\overline{I}_4.(R_{eq} + 1/(j.\omega.C_4))| \tag{3.9}$$

The voltage, current and transconductance gain functions analysis infer inherent capabilities of a given resonant configuration like operation in CC and/or CV modes fundamental for charging process of lithium batteries. Fig. 3.3 [31] demonstrates the charging strategy of an EV lithium battery established on its SoC level. During 10-85 %, a CC

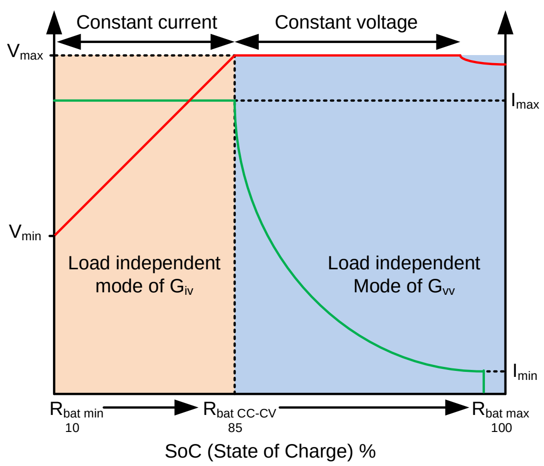


Figure 3.3: Charging profile of a EV lithium battery [31].

stage is applied, while the CV stage is set between the 85-100 % with the main function of equalization. Therefore, it is relevant to study, for each resonant configuration, to identify their intrinsic CC and CV features. The IPT system provides, under specific conditions, the voltage source characteristic when the voltage gain function ($G_{vReqvin}$) is in LIO. On the other hand, the system shows the current source characteristic when the transconductance gain function ($G_{i4vin}$) is in LIO. Moreover, the transconductance gain function ($G_{i1vin}$) can also be used as a requirement for the system project in DIPT mode, only when the off-board compensation side is known. Therefore, it is guaranteed a CC in ORMC transmitter current when there is no-coupling mode. In addition, the alternative transconductance gain function $G_{i2vin}$ can also be used as a requirement for the system project, only when the off-board compensation side is known. Therefore, it is guaranteed the compatibility of the same energy transfer capacities of the proposed system with electric pads previously installed.

The following subsections that are related to the mathematical analysis of the aforementioned resonant topologies are detailed in the Appendix section.

## 3.2 Analysis of S-S-S topology

By incorporating a second MC, a new resonant compensation is introduced, altering the resonant properties of traditional IPT setups, specifically between the ORMC and the IRMC. The decision to introduce a series compensation provides a new way for operation on the off-board, wheel, and on-board aspects. In this configuration, the primary and secondary coils are connected in series with capacitors forming resonant circuits. The S-S-S topology [31] exhibits the highest power transfer capability and,

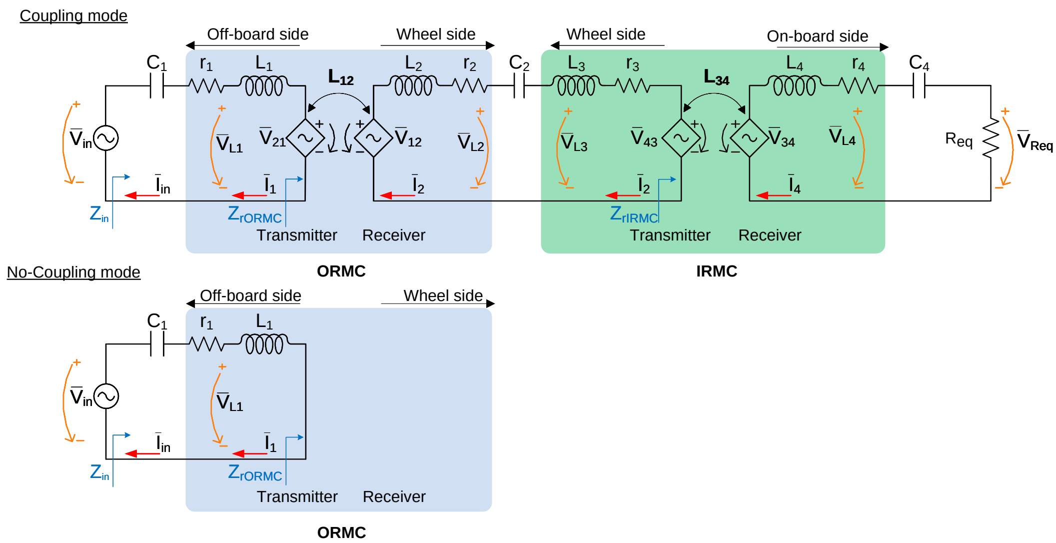


Figure 3.4: Equivalent circuit model of a double coupling inWIPT for S-S-S resonant compensation for: (a) coupling mode and (b) no-coupling mode [31].

under resonance, LIO for SIPT applications. In contrast, in DIPT applications, due to low or no-coupling operation, it presents the disadvantage of high circulating currents in the transmitter side due to the decrease of $|Z_{in}|$, that can lead to converter failure illustrated in Fig 3.4.

The following subsections present the mathematical equations of the mentioned resonant configuration.

### 3.2.1 Circuit analysis

The equivalent circuit model of a double coupling for S-S-S resonant configuration is presented in Fig. 3.2 (a).

Applying the Kirchoff's laws to the circuit, the following equations are obtained:

$$\overline{V}_{in} = r_1.\overline{I}_{in} + j.\omega((L_1 - 1/(\omega^2.C_1))\overline{I}_{in} - L_{12}.\overline{I}_2), \tag{3.10}$$

$$0 = (r_2 + r_3).\overline{I}_2 + j.\omega((L_2 + L_3 - 1/(\omega^2.C_2))\overline{I}_2 - L_{12}.\overline{I}_1 - L_{34}.\overline{I}_4), \tag{3.11}$$

$$0 = (R_{eq} + r_4).\overline{I}_4 + j.\omega((L_4 - 1/(\omega^2.C_4))\overline{I}_4 - L_{34}.\overline{I}_2), \tag{3.12}$$

The capacitors [31] values are given by

$$C_1 = 1/(\omega_1^2.L_1), \tag{3.13}$$

$$C_2 = 1/(\omega_2^2.(L_2 + L_3)), \tag{3.14}$$

$$C_4 = 1/(\omega_4^2.L_4). \tag{3.15}$$

Solving (3.10) to (3.12) provides the current equations that accurately define the S-S-S model:

$$\overline{I}_{in} = \frac{\overline{V}_{in}}{Z_{in}} = \frac{\overline{V}_{in}}{(Z_1 + Z_{r_{ORMC}})}, \tag{3.16}$$

$$\overline{I}_2 = \overline{I}_{in}\frac{j.\omega.L_{12}}{(Z_2 + Z_{r_{IRMC}})}, \tag{3.17}$$

$$\overline{I}_4 = \overline{I}_2\frac{j.\omega.L_{34}}{(Z_4 + R_{eq})}. \tag{3.18}$$

where $Z_1$, $Z_2$ and $Z_4$ are given by

$$Z_1 = r_1 + j.\omega(L_1 - 1/(\omega^2.C_1)), \tag{3.19}$$

$$Z_2 = (r_2 + r_3) + j.\omega.(L_2 + L_3 - 1/(\omega^2.C_2)), \tag{3.20}$$

$$Z_4 = r_4 + j.\omega(L_4 - 1/(\omega^2.C_4)). \tag{3.21}$$

The reflected impedance from the on-board side onto the wheel side ($Z_{r_{IRMC}}$) is defined in (3.22), while the reflected impedance from the wheel side onto the off-board side ($Z_{r_{ORMC}}$) is described in (3.23).

$$Z_{r_{IRMC}} = \frac{\overline{V}_{43}}{\overline{I}_3} = \frac{(\omega^2.L_{34}^2)}{(Z_4 + R_{eq})}, \tag{3.22}$$

$$Z_{r_{ORMC}} = \frac{\overline{V}_{21}}{\overline{I}_1} = \frac{(\omega^2.L_{12}^2(Z_4 + R_{eq})}{(Z_2(Z_4 + R_{eq}) + \omega^2.L_{34}^2)}. \tag{3.23}$$

### 3.2.2 Transfer functions

The following equations are found by rearranging (3.16)-(3.18).

The voltage transfer function ($G_{vReqvin}$) correlates the output voltage of the equivalent resistance of the batteries ($\overline{V}_{Req}$) with the input voltage ($\overline{V}_{in}$). This function is calculated into

$$G_{vReqvin} = \frac{\overline{V}_{R_{eq}}}{\overline{V}_{in}} = -\frac{\omega^2.R_{eq}.L_{12}.L_{34}}{(R_{eq} + Z_4)(Z_2 + Z_{r_{IRMC}})(Z_1 + Z_{r_{ORMC}})}. \tag{3.24}$$

If the system losses are neglected ($r_1 = r_2 = r_3 = r_4 = 0\ \Omega$) and the system is under resonance ($\omega = \omega_x$), using MATLAB simplify function, (3.24) is defined by

$$G_{vReqvin} = -\frac{L_{34}}{L_{12}}. \tag{3.25}$$

As is demonstrated by (3.25), when $G_{vReqvin}$ satisfies the specified conditions, it can be classified as being in LIO and this topology does exhibit the operation point with CV characteristics.

The transconductance function ($G_{i4vin}$) correlates the output current of on-board receiver side ($\overline{I}_4$) with $\overline{V}_{in}$ and it is given by

$$G_{i4vin} = \frac{\overline{I}_4}{\overline{V}_{in}} = -\frac{\omega^2.L_{12}.L_{34}}{(R_{eq} + Z_4)(Z_2 + Z_{r_{IRMC}})(Z_1 + Z_{r_{ORMC}})}. \tag{3.26}$$

If the system losses are neglected ($r_1 = r_2 = r_3 = r_4 = 0\ \Omega$) and the system is under resonance ($\omega = \omega_x$), using MATLAB simplify function, (3.26) is defined by

$$G_{i4vin} = -\frac{L_{34}}{R_{eq}.L_{12}}. \tag{3.27}$$

As is showed by (3.27), when fulfills the specified conditions, $G_{i4vin}$ is not in LIO and this topology does not exhibit the operation point with CC characteristics.

The transconductance function ($G_{i1vin}$) correlates the input current ($\overline{I}_1$) with $\overline{V}_{in}$ and is defined by

$$G_{i1vin} = \frac{\overline{I}_1}{\overline{V}_{in}} = \frac{1}{(Z_1 + Z_{r_{ORMC}})}. \tag{3.28}$$

If the system losses are neglected ($r_1 = r_2 = r_3 = r_4 = 0\ \Omega$) and the system is under resonance ($\omega = \omega_x$), using MATLAB simplify function, (3.28) is defined by

$$G_{i1vin} = \frac{L_{34}^2}{R_{eq}.L_{12}^2}. \tag{3.29}$$

For this configuration (3.29), $G_{i1vin}$ is not independent of $L_{12}$ as mentioned before. Therefore, $\overline{I}_1$ is not constant and this characteristic consists an issue to control it when the system is in no-coupling condition.

The input impedance ($Z_{in}$) is the equivalent impedance seen by the power supply and it is the aggregated of the reflected impedance from IRMC and the receiver side ORMC onto the transmitter side ORMC and the equivalent impedances of the transmitter side ORMC and input side. The equation of $Z_{in}$ is shown by

$$Z_{in} = Z_1 + Z_{r_{ORMC}}. \tag{3.30}$$

If the system losses are neglected ($r_1 = r_2 = r_3 = r_4 = 0\ \Omega$) and the system is under resonance ($\omega = \omega_x$), using MATLAB simplify function, (3.30) is defined by

$$Z_{in} = \frac{R_{eq}.L_{12}^2}{L_{34}^2}. \tag{3.31}$$

Assuming the mentioned conditions, (3.31) is purely resistive and depends on the ratio of $L_{34}^2/L_{12}^2$.

## 3.3 Analysis of LCL-S-S topology

In typical SIPT applications, the inverter PHS angle is adjusted in order to control the power delivered to the load [47]. Nonetheless, considering DIPT operation, the inherent EV movement can lead to fast changes in the system coupling, and so a fast controller will need to be used to control the inverter operation. To simplify the control of the input voltage for the DIPT operation and take advantage of the characteristic of the current source of the hybrid LCL topology (at $L_1$), which implies that $|\overline{I}_1|$ will remain constant for the same $\overline{V}_{in}$ independently of the variation in load and coupling, the value of $\overline{V}_{in}$ remains constant throughout the process.

The following subsections present the mathematical equations of the mentioned resonant configuration.

### 3.3.1 Circuit analysis

The equivalent circuit model of a double coupling for LCL-S-S resonant configuration is presented in Fig. 3.2 (b).

Applying the Kirchoff's laws to the circuit, the following equations are obtained:

$$\overline{V}_{in} = r_s.\overline{I}_{in} + j.\omega((L_s - 1/(\omega^2.C_1))\overline{I}_{in} + 1/(\omega^2.C_1)\overline{I}_1), \tag{3.32}$$

$$0 = r_1.\overline{I}_1 + j.\omega(1/(\omega^2.C_1)\overline{I}_{in} + (L_1 - 1/(\omega^2.C_1))\overline{I}_1 - L_{12}.\overline{I}_2), \tag{3.33}$$

$$0 = (r_2 + r_3).\overline{I}_2 + j.\omega((L_2 + L_3 - 1/(\omega^2.C_2))\overline{I}_2 - L_{12}.\overline{I}_1 - L_{34}.\overline{I}_4), \tag{3.34}$$

$$0 = (R_{eq} + r_4).\overline{I}_4 + j.\omega((L_4 - 1/(\omega^2.C_4))\overline{I}_4 - L_{34}.\overline{I}_2), \tag{3.35}$$

The capacitors [48] values are given by

$$C_1 = 1/(\omega_1^2.L_1) = 1/(\omega_1^2.L_s), \tag{3.36}$$

$$C_2 = 1/(\omega_2^2.(L_2 + L_3)), \tag{3.37}$$

$$C_4 = 1/(\omega_4^2.L_4), \tag{3.38}$$

Solving (3.32) to (3.35) provides the current equations that accurately define the LCL-S-S model:

$$\overline{I}_{in} = \frac{\overline{V}_{in}}{Z_{in}} = \frac{\overline{V}_{in}}{r_s + j.\omega.L_s + \frac{1}{(j.\omega.C_1)} + \frac{1}{\omega^2.C_1^2\left(Z_1 + Z_{r_{ORMC}} + \frac{1}{(j.\omega.C_1)}\right)}}, \tag{3.39}$$

$$\overline{I}_1 = -\overline{I}_{in}\frac{j}{\omega.C_1\left(Z_1 + Z_{r_{ORMC}} + \frac{1}{(j.\omega.C_1)}\right)}, \tag{3.40}$$

$$\overline{I}_2 = \overline{I}_1\frac{j.\omega.L_{12}}{(Z_2 + Z_{r_{IRMC}})}, \tag{3.41}$$

$$\overline{I}_4 = \overline{I}_2\frac{j.\omega.L_{34}}{(Z_4 + R_{eq})}, \tag{3.42}$$

where $Z_1$, $Z_2$ and $Z_4$ are given by

$$Z_1 = r_1 + j.\omega.L_1, \tag{3.43}$$

$$Z_2 = (r_2 + r_3) + j.\omega.(L_2 + L_3 - 1/(\omega^2.C_2)), \tag{3.44}$$

$$Z_4 = r_4 + j.\omega(L_4 - 1/(\omega^2.C_4)), \tag{3.45}$$

The reflected impedance from the on-board side onto the wheel side ($Z_{r_{IRMC}}$) is defined in (3.22), while the reflected impedance from the wheel side onto the off-board side

$(Z_{r_{ORMC}})$ is described in (3.23).

### 3.3.2 Transfer functions

The following equations are found by rearranging (3.39)-(3.42).

The voltage transfer function $(G_{vReqvin})$ correlates the output voltage of the equivalent resistance of the batteries $(\overline{V}_{Req})$ with the input voltage $(\overline{V}_{in})$. This function is calculated into

$$G_{vReqvin} = \frac{\overline{V}_{Req}}{\overline{V}_{in}} = \frac{j.\omega.R_{eq}.L_{12}.L_{34}}{C_1(R_{eq}+Z_4)\left(Z_1+Z_{r_{ORMC}}+\frac{1}{(j.\omega.C_1)}\right)(Z_2+Z_{r_{IRMC}})\left(r_s+j.\omega.L_s+\frac{1}{(j.\omega.C_1)}+\frac{1}{C_1^2.\omega^2\left(Z_1+Z_{r_{ORMC}}+\frac{1}{(j.\omega.C_1)}\right)}\right)}. \quad (3.46)$$

If the system losses are neglected $(r_s = r_1 = r_2 = r_3 = r_4 = 0\ \Omega)$, the system is under resonance $(\omega = \omega_x)$ and $L_s = L_1$, using MATLAB simplify function, (3.46) is defined by

$$G_{vReqvin} = \frac{j.R_{eq}.L_{12}}{L_1.L_{34}.\omega}. \quad (3.47)$$

As is demonstrated by (3.47), when $G_{vReqvin}$ satisfies the specified conditions, it cannot be classified as being in LIO and this topology does not exhibit the operation point with CV characteristics.

The transconductance function $(G_{i4vin})$ correlates the output current of on-board receiver side $(\overline{I}_4)$ with $\overline{V}_{in}$ and it is given by

$$G_{i4vin} = \frac{\overline{I}_4}{\overline{V}_{in}} = \frac{j.\omega.L_{12}.L_{34}}{C_1(R_{eq}+Z_4)\left(Z_1+Z_{r_{ORMC}}+\frac{1}{(j.\omega.C_1)}\right)(Z_2+Z_{r_{IRMC}})\left(r_s+j.\omega.L_s+\frac{1}{(j.\omega.C_1)}+\frac{1}{C_1^2.\omega^2\left(Z_1+Z_{r_{ORMC}}+\frac{1}{(j.\omega.C_1)}\right)}\right)}. \quad (3.48)$$

If the system losses are neglected $(r_s = r_1 = r_2 = r_3 = r_4 = 0\ \Omega)$, the system is under resonance $(\omega = \omega_x)$ and $L_s = L_1$, using MATLAB simplify function, (3.48) is defined by

$$G_{i4vin} = \frac{j.L_{12}}{L_1.L_{34}.\omega}. \quad (3.49)$$

As is showed by (3.49), when fulfills the specified conditions, $G_{i4vin}$ is in LIO and this topology exhibits the operation point with CC characteristics.

The transconductance function $(G_{i1vin})$ correlates the input current $(\overline{I}_1)$ with $\overline{V}_{in}$ and is defined by

$$G_{i1vin} = \frac{\overline{I}_1}{\overline{V}_{in}} = -\frac{j}{C_1.\omega\left(Z_1+Z_{r_{ORMC}}+\frac{1}{(j.\omega.C_1)}\right)\left(r_s+j.\omega.L_s+\frac{1}{(j.\omega.C_1)}+\frac{1}{C_1^2.\omega^2\left(Z_1+Z_{r_{ORMC}}+\frac{1}{(j.\omega.C_1)}\right)}\right)}. \quad (3.50)$$

If the system losses are neglected $(r_s = r_1 = r_2 = r_3 = r_4 = 0\ \Omega)$, the system is under resonance $(\omega = \omega_x)$ and $L_s = L_1$, using MATLAB simplify function, (3.50) is defined by

$$G_{i1vin} = -\frac{j}{\omega.L_1}. \tag{3.51}$$

For this configuration (3.51), $G_{i1vin}$ is independent of $L_{12}$ as mentioned previously. Therefore, $\overline{I}_1$ is constant (CC characteristics). This characteristic consists a possible solution to control $\overline{I}_1$ when the system is in no-coupling condition.

The input impedance ($Z_{in}$) is the equivalent impedance seen by the power supply and it is the aggregated of the reflected impedance from IRMC and the receiver side ORMC onto the transmitter side ORMC and the equivalent impedances of the transmitter side ORMC and input side. The equation of $Z_{in}$ is shown by

$$Z_{in} = r_s + j.\omega.L_s + \frac{1}{(j.\omega.C_1)} + \frac{1}{\omega^2.C_1^2\left(Z_1 + Z_{r_{ORMC}} + \frac{1}{(j.\omega.C_1)}\right)}. \tag{3.52}$$

If the system losses are neglected ($r_s = r_1 = r_2 = r_3 = r_4 = 0\ \Omega$), the system is under resonance ($\omega = \omega_x$) and $L_s = L_1$, using MATLAB simplify function, (3.52) is defined by

$$Z_{in} = \frac{\omega^2.L_1^2.L_{34}^2}{L_{12}^2.R_{eq}}. \tag{3.53}$$

Assuming the mentioned conditions, (3.53) is purely resistive and depends on the ratio of $L_{34}^2/L_{12}^2$, $L_1^2$ and $\omega^2$.

## 3.4 Analysis of LCC-S-S topology

The LCC-S-S configuration is presented as a variation of LCL-S-S where an extra capacitor $C_1$ is added in series with the transmitter coil $L_1$ of the MC and altering the resonant properties of the traditional IPT setups and being proposed for different applications, such as automation applications and IPT pickup compensation [49]. In the alternative compensation, the proposed LCC topology [49] offers a significant advantage as the resonant frequency remains unaffected by both the coupling coefficient and the load condition. This means that regardless of the load's characteristics, the system maintains a consistent resonant frequency for power transfer. Additionally, the resonant configuration of the proposed LCC topology ensures ZPA. At the switching frequency $f_s$, the reactance of the input inductor $L_s$, parallel capacitor $C_s$, and the combination of track inductance and series capacitance are all equal.

The following subsections present the mathematical equations of the mentioned resonant configuration.

### 3.4.1 Circuit analysis

The equivalent circuit model for the double coupling for LCC-S-S resonant configuration is presented in Fig. 3.2 (c).

Applying the Kirchoff's laws to the circuit, the following equations are obtained:

$$\overline{V}_{in} = r_s.\overline{I}_{in} + j.\omega((L_s - 1/(\omega^2.C_s))\overline{I}_{in} + 1/(\omega^2.C_s)\overline{I}_1), \tag{3.54}$$

$$0 = r_1.\overline{I}_1 + j.\omega(1/(\omega^2.C_s)\overline{I}_{in} + (L_1 - 1/(\omega^2.C_1) - 1/(\omega^2.C_s))\overline{I}_1 - L_{12}.\overline{I}_2), \tag{3.55}$$

$$0 = (r_2 + r_3).\overline{I}_2 + j.\omega((L_2 + L_3 - 1/(\omega^2.C_2))\overline{I}_2 - L_{12}.\overline{I}_1 - L_{34}.\overline{I}_4), \tag{3.56}$$

$$0 = (R_{eq} + r_4).\overline{I}_4 + j.\omega((L_4 - 1/(\omega^2.C_4))\overline{I}_4 - L_{34}.\overline{I}_2), \tag{3.57}$$

The capacitors [50] values are given by

$$C_s = 1/(\omega_s^2.L_s), \tag{3.58}$$

$$C_1 = 1/(\omega_1^2.(L_1 - L_s)), \tag{3.59}$$

$$C_2 = 1/(\omega_2^2.(L_2 + L_3)), \tag{3.60}$$

$$C_4 = 1/(\omega_4^2.L_4), \tag{3.61}$$

Solving (3.54) to (3.57) provides the current equations that accurately define the LCC-S-S model:

$$\overline{I}_{in} = \frac{\overline{V}_{in}}{Z_{in}} = \frac{\overline{V}_{in}}{r_s + j.\omega.L_s + \frac{1}{(j.\omega.C_s)} + \frac{1}{\omega^2.C_s^2\left(Z_1 + Z_{r_{ORMC}} + \frac{1}{(j.\omega.C_s)}\right)}}, \tag{3.62}$$

$$\overline{I}_1 = -\overline{I}_{in}\frac{j}{\omega.C_s\left(Z_1 + Z_{r_{ORMC}} + \frac{1}{(j.\omega.C_s)}\right)}, \tag{3.63}$$

$$\overline{I}_2 = \overline{I}_1\frac{j.\omega.L_{12}}{(Z_2 + Z_{r_{IRMC}})}, \tag{3.64}$$

$$\overline{I}_4 = \overline{I}_2\frac{j.\omega.L_{34}}{(Z_4 + R_{eq})}, \tag{3.65}$$

where $Z_1$, $Z_2$ and $Z_4$ are given by

$$Z_1 = r_1 + j.\omega(L_1 - 1/(\omega^2.C_1)), \tag{3.66}$$

$$Z_2 = (r_2 + r_3) + j.\omega.(L_2 + L_3 - 1/(\omega^2.C_2)), \tag{3.67}$$

$$Z_4 = r_4 + j.\omega(L_4 - 1/(\omega^2.C_4)), \tag{3.68}$$

The reflected impedance from the on-board side onto the wheel side ($Z_{r_{IRMC}}$) is defined in (3.22), while the reflected impedance from the wheel side onto the off-board side ($Z_{r_{ORMC}}$) is described in (3.23).

### 3.4.2 Transfer functions

The following equations are found by rearranging (3.62)-(3.65).

The voltage transfer function ($G_{vReqvin}$) correlates the output voltage of the equivalent resistance of the batteries ($\overline{V}_{Req}$) with the input voltage ($\overline{V}_{in}$). This function is calculated into

$$G_{vReqvin} = \frac{\overline{V}_{Req}}{\overline{V}_{in}} = \frac{j.\omega.R_{eq}.L_{12}.L_{34}}{C_s(R_{eq}+Z_4)\left(Z_1+Z_{r_{ORMC}}+\frac{1}{(j.\omega.C_s)}\right)(Z_2+Z_{r_{IRMC}})\left(r_s+j.\omega.L_s+\frac{1}{(j.\omega.C_s)}+\frac{1}{C_s^2.\omega^2\left(Z_1+Z_{r_{ORMC}}+\frac{1}{(j.\omega.C_s)}\right)}\right)}. \quad (3.69)$$

If the system losses are neglected ($r_s = r_1 = r_2 = r_3 = r_4 = 0\ \Omega$) and the system is under resonance ($\omega = \omega_x$), using MATLAB simplify function, (3.69) is defined by

$$G_{vReqvin} = \frac{j.R_{eq}.L_{12}}{L_s.L_{34}.\omega}. \quad (3.70)$$

As is demonstrated by (3.70), when $G_{vReqvin}$ satisfies the specified conditions, it cannot be classified as being in LIO and this topology does not exhibit the operation point with CV characteristics.

The transconductance function ($G_{i4vin}$) correlates the output current of on-board receiver side ($\overline{I}_4$) with $\overline{V}_{in}$ and it is given by

$$G_{i4vin} = \frac{\overline{I}_4}{\overline{V}_{in}} = \frac{j.\omega.L_{12}.L_{34}}{C_s(R_{eq}+Z_4)\left(Z_1+Z_{r_{ORMC}}+\frac{1}{(j.\omega.C_s)}\right)(Z_2+Z_{r_{IRMC}})\left(r_s+j.\omega.L_s+\frac{1}{(j.\omega.C_s)}+\frac{1}{C_s^2.\omega^2\left(Z_1+Z_{r_{ORMC}}+\frac{1}{(j.\omega.C_s)}\right)}\right)}. \quad (3.71)$$

If the system losses are neglected ($r_s = r_1 = r_2 = r_3 = r_4 = 0\ \Omega$) and the system is under resonance ($\omega = \omega_x$), using MATLAB simplify function, (3.71) is defined by

$$G_{i4vin} = \frac{j.L_{12}}{L_s.L_{34}.\omega}. \quad (3.72)$$

As shown by (3.72), when the specified conditions are met, $G_{i4vin}$ is in LIO and this topology exhibits the operation point with CC characteristics.

The transconductance function ($G_{i1vin}$) correlates the input current ($\overline{I}_1$) with $\overline{V}_{in}$ and is defined by

$$G_{i1vin} = \frac{\overline{I}_1}{\overline{V}_{in}} = -\frac{j}{C_s.\omega\left(Z_1+Z_{r_{ORMC}}+\frac{1}{(j.\omega.C_s)}\right)\left(r_s+j.\omega.L_s+\frac{1}{(j.\omega.C_s)}+\frac{1}{C_s^2.\omega^2\left(Z_1+Z_{r_{ORMC}}+\frac{1}{(j.\omega.C_s)}\right)}\right)}. \quad (3.73)$$

If the system losses are neglected ($r_s = r_1 = r_2 = r_3 = r_4 = 0\ \Omega$) and the system is under resonance ($\omega = \omega_x$), using MATLAB simplify function, (3.73) is defined by

$$G_{i1vin} = -\frac{j}{\omega.L_s}. \tag{3.74}$$

For this configuration (3.74), $|G_{i1vin}|$ is independent of $L_{12}$ as mentioned before. Therefore, $\overline{I}_1$ is constant (CC characteristics). This characteristic consists of a possible solution to control $\overline{I}_1$ when the system is in no-coupling condition.

The input impedance ($Z_{in}$) is the equivalent impedance seen by the power supply and it is the aggregated of the reflected impedance from IRMC and the receiver side ORMC onto the transmitter side ORMC and the equivalent impedances of the transmitter side ORMC and input side. The equation of $Z_{in}$ is shown by

$$Z_{in} = r_s + j.\omega.L_s + \frac{1}{(j.\omega.C_s)} + \frac{1}{\omega^2.C_s^2\left(Z_1 + Z_{r_{ORMC}} + \frac{1}{(j.\omega.C_s)}\right)}. \tag{3.75}$$

If the system losses are neglected ($r_s = r_1 = r_2 = r_3 = r_4 = 0\ \Omega$) and the system is under resonance ($\omega = \omega_x$), using MATLAB simplify function, (3.75) is defined by

$$Z_{in} = \frac{\omega^2.L_s^2.L_{34}^2}{L_{12}^2.R_{eq}}. \tag{3.76}$$

Assuming the mentioned conditions, (3.76) is purely resistive and depends on the ratio of $L_{34}^2/L_{12}^2$, $L_s^2$ and $\omega^2$.

Table 3.1 presents a summary of all the transfer functions and $Z_{in}$ equations of the aforementioned resonant configurations under resonance operation. In the case of $G_{vReqvin}$, S-S-S only shows LIO and depends of the mutual inductances of the system and the angular frequency of the system. However, both LCL-S-S and LCC-S-S does not present this characteristic of load independence and depend of the same ratio of mutual inductances and of a self-inductance $L_1$ and $L_s$, respectively. For $G_{i4vin}$, both LCL-S-S and LCC-S-S present LIO and depend of the mentioned self and mutual inductances and angular frequency of the system. However, the S-S-S topology does not exhibit LIO as the previous topologies. As for $G_{i1vin}$, LCL-S-S and LCC-S-S show a load and both mutual inductance independence, which validates the proposal of these new resonant configurations for the DIPT operation. On the other hand, the S-S-S presents the opposite behaviour and does not allow zero coupling allowance like the other topologies. According to the input impedance $Z_{in}$, all resonant compensations show a dependence of most of the aforementioned parameters, varying the module of $Z_{in}$.

Table 3.1: Transfer functions and $Z_{in}$ equation for all resonant configurations under resonant condition

| | S-S-S | LCL-S-S | LCC-S-S |
|---|---|---|---|
| $G_{vReqvin}$ | $-\dfrac{L_{34}}{L_{12}}$ | $\dfrac{j.R_{eq}.L_{12}}{L_1.L_{34}.\omega}$ | $\dfrac{j.R_{eq}.L_{12}}{L_s.L_{34}.\omega}$ |
| $G_{i4vin}$ | $-\dfrac{L_{34}}{R_{eq}.L_{12}}$ | $\dfrac{j.L_{12}}{L_1.L_{34}.\omega}$ | $\dfrac{j.L_{12}}{L_s.L_{34}.\omega}$ |
| $G_{i1vin}$ | $\dfrac{L_{34}^2}{R_{eq}.L_{12}^2}$ | $-\dfrac{j}{\omega.L_1}$ | $-\dfrac{j}{\omega.L_s}$ |
| $Z_{in}$ | $\dfrac{R_{eq}.L_{12}^2}{L_{34}^2}$ | $\dfrac{\omega^2.L_1^2.L_{34}^2}{L_{12}^2.R_{eq}}$ | $\dfrac{\omega^2.L_s^2.L_{34}^2}{L_{12}^2.R_{eq}}$ |

## 3.5 Resonant compensation behavioural analysis

The voltage, transconductance, input impedance $Z_{in}$ and equivalent resistance $R_{eq}$ power functions are analysed under different $R_{eq}$ (two different SoC values) and $L_{12}$ values in Fig. 3.5 and Fig. 3.6. This assessment was made to validate and identify intrinsic CC and CV modes for all the resonant configurations analysed earlier. In this system, $k_{34}$ is kept constant for all plots, since the air gap in the IRMC design (solenoid geometry) is constant and independent of any charging positions. Additionally, the module and phase of $Z_{in}$ are analysed to assess the conditions of ZPA, zero voltage switching (ZVS), and zero current switching (ZCS) to measure the overall efficiency of the system according to the switching losses on the inverter. This comparative analysis was carried out by simulating the gain functions, input impedance $Z_{in}$ and equivalent resistance $R_{eq}$ power of the different resonant configurations in accordance with certain system specifications for the fundamental harmonic component and under resonance and ideal conditions ($r_s = r_1 = r_2 = r_3 = r_4 = 0\ \Omega$) presented in Table 3.2. Moreover, the MATLAB plots were made while varying a range of $L_{12}$ values, which the used capacitors of the following case studies were designed to operate under resonance and for full-coupling condition $L_{12_{max}}$. Table 3.2 presents two case studies $L_s \approx L_1 (L_s = 0.999 \times L_1)$ and $L_s = 0.5 \times L_1$, which allowed the use of new capacitors for each case study. The first case study was chosen to meet the requirement of different values of $L_s$ and $L_1$ to calculate a possible $C_1$ of the LCC-S-S topology corresponding to (3.59). On the other hand, the second condition was selected to understand the behaviour of the system under the mentioned specification and compare the differences between both conditions.

Fig. 3.5 (a) and Fig. 3.6 (a) illustrate the phase of $Z_{in}$. This variable presents ZPA and this happens independently of $R_{eq}$ and $L_{12}$ for all resonant configurations in Fig. 3.5 (a). This behaviour exhibits again with the exception of the LCL-S-S topology at higher $L_{12}$ values to achieve maximum energy transfer in Fig. 3.6 (a). This is explained due to the inequality of $L_s$ and $L_1$ values for the calculation of the capacitor $C_1$ previously mentioned in (3.36), which presents a deviation of the expected ZPA, presenting a restraint for the design with this configuration. On the other hand, the LCC-S-S configuration remains the ZPA condition and it is independent of the mentioned condition of self-inductances. Furthermore, the module of $Z_{in}$ demonstrates higher values for low $L_{12}$ values and different $R_{eq}$ values in both LCL-S-S and LCC-S-S topologies. Therefore, when the system is in no-coupling condition, $|Z_{in}|$ is higher as shown in Fig. 3.5 (b) and Fig. 3.6 (b) and as a result, there is no high circulating currents. However, for the S-S-S topology, this characteristic is not achieved and being a significant drawback for DIPT operation.

According to Fig. 3.5 (c), the voltage gain ($G_{VReqVin}$) shows an exponential behaviour for lower $L_{12}$ values in the S-S-S topology. In addition, S-S-S is independent of $R_{eq}$ values. Although, for both LCL-S-S and LCC-S-S configurations, the behaviour is linear and is not independent for different $R_{eq}$ values, assuming the condition $L_s = L_1$ for the LCL-S-S, which only LCC-S-S presents the aforementioned behaviour in Fig. 3.6 (c). Moreover, the transconductance gain $G_{I4Vin}$ exhibits a linear characteristic, independently of $R_{eq}$ values in both LCL-S-S and LCC-S-S topologies in Fig. 3.5 (d), if the previous condition is ensured only for the LCL-S-S topology. This condition is not ac-

Table 3.2: Electrical and magnetic specifications for the plots of different variables under dynamic operation for inWIPT system

| Parameter | Value |
|---|---|
| Electrical system specifications | |
| $V_{DC}$ | 200 V (from $1\phi$ grid) |
| $f_s$ | 85 kHz |
| $C_s$ (LCC-S-S) | 82.17 and 164.17 $nF$ |
| $C_1$ (LCC-S-S) | 82.09 $\mu F$ and 164.17 $nF$ |
| $C_1$ (S-S-S and LCL-S-S) | 82.09 $nF$ |
| $C_2$ | 61.62 $nF$ |
| $C_4$ | 253.50 $nF$ |
| $R_{bat}/R_{eq}$ | 2.4/1.9 and 100/81.1 $\Omega$ |
| Magnetic system specifications | |
| $k_{12}$ | 0.147 |
| $k_{34}$ | 0.460 |
| $L_{12}$ | 6.1 $\mu H$ |
| $L_{34}$ | 6.9 $\mu H$ |
| $L_s$ | 42.67 and 21.35 $\mu H$ |
| $L_1$ | 42.71 $\mu H$ |
| $L_2$ | 40.45 $\mu H$ |
| $L_3$ | 16.45 $\mu H$ |
| $L_4$ | 13.83 $\mu H$ |

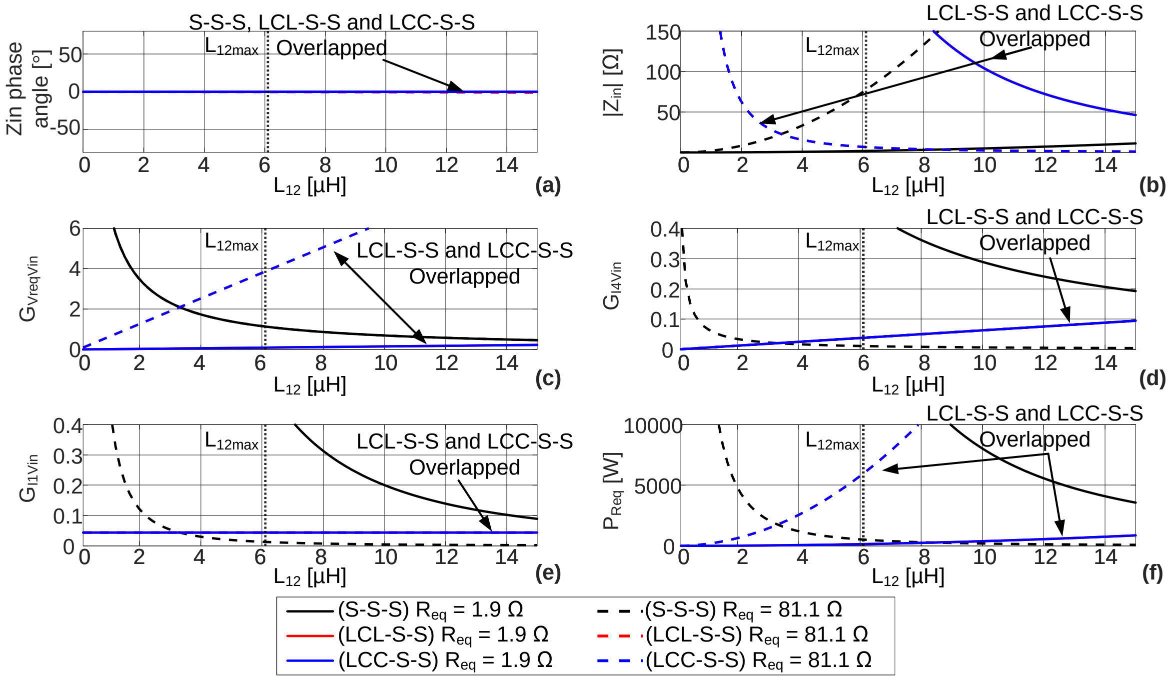


Figure 3.5: MATLAB plots using the condition $L_s \approx L_1 (L_s = 0.999 \times L_1)$ for: (a) Phase, (b) module of $Z_{in}$, (c) voltage gain $G_{VReqVin}$, (d) transconductance gain $G_{I4Vin}$, (e) transconductance gain $G_{I1Vin}$ and (f) equivalent resistance power $P_{Req}$ as function of mutual inductance of ORMC $L_{12}$.

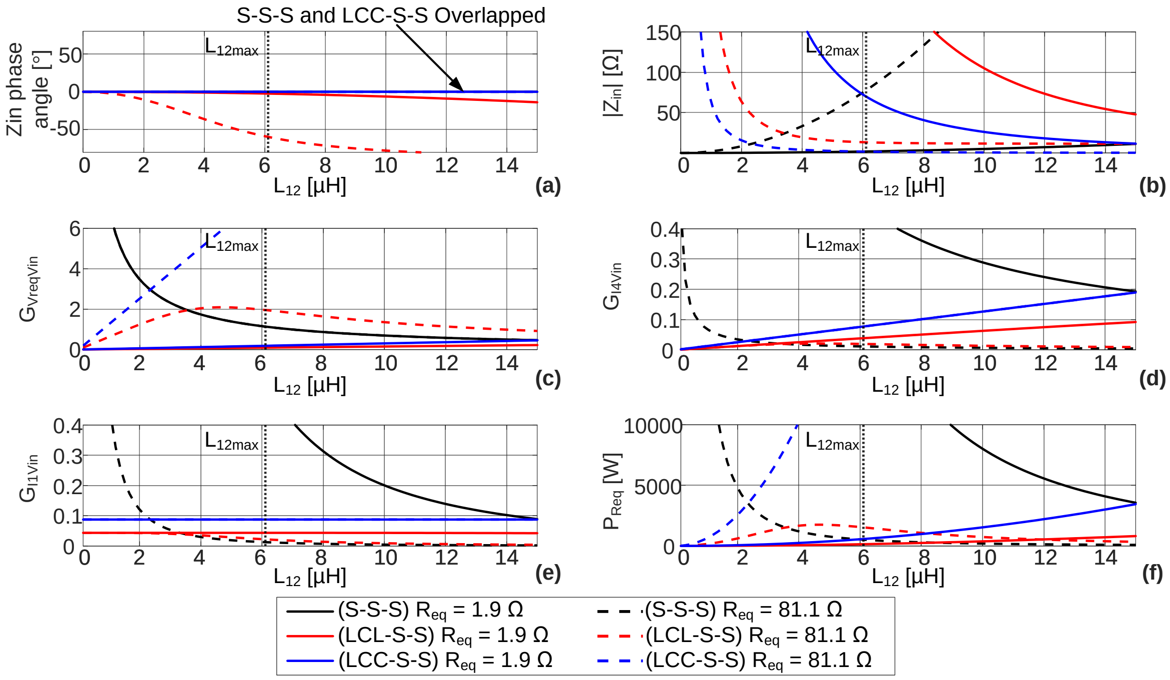


Figure 3.6: MATLAB plots using the condition $L_s = 0.5 \times L_1$ for: (a) Phase, (b) module of $Z_{in}$, (c) voltage gain $G_{VReqVin}$, (d) transconductance gain $G_{I4Vin}$, (e) transconductance gain $G_{I1Vin}$ and (f) equivalent resistance power $P_{Req}$ as function of mutual inductance of ORMC $L_{12}$.

complished in Fig. 3.6 (d) and it loses LIO, but it maintains the linear behaviour. On the other hand, the S-S-S topology shows an exponential behaviour and increases for lower $L_{12}$ values, but it depends on the $R_{eq}$ and $L_{12}$ values.

For both LCL-S-S and LCC-S-S resonant configurations, the transconductance gain $G_{I1Vin}$ shows constant characteristic, regardless of $R_{eq}$ and $L_{12}$ proven by Fig 3.5 (e). Therefore, the ORMC transmitter current ($\overline{I}_1$) is a CC and these topologies ensure a desirable feature for DIPT operation. In Fig 3.6 (e), the LCL-S-S topology presents a variation of $\overline{I}_1$ and as a result, it is not LIO comparing with in Fig 3.5 (e). In case of the LCC-S-S, this topology maintains the same properties mentioned earlier for DIPT operation. For $R_{eq}$ power, the S-S-S topology presents an exponential behaviour for lower $L_{12}$ values and decreases with the increasing $L_{12}$ as shown in Fig 3.5 (f), being dependent of $R_{eq}$ values. Furthermore, assuming the mentioned condition for the LCL-S-S topology, the remaining topologies show the opposite behaviour of the S-S-S topology and are independent of the $R_{eq}$ values. On the other hand, the LCL-S-S achieves a maximum power transfer between 4 and 6 $\mu H$, however, this variable decreases with the increase of $L_{12}$ due to the inequality of the previous condition as demonstrated in Fig 3.6 (f).

Table 3.3 summarizes the main characteristics of the three resonant configurations, in such conditions expressed in Table 3.2 and shown in Fig 3.5 and Fig 3.6. As mentioned earlier and except for the S-S-S topology, both LCL-S-S and LCC-S-S configurations allow zero coupling conditions and the input impedance phase $Z_{in}$ are independent of the equivalent resistance $R_{eq}$ and ORMC mutual inductance $L_{12}$, as shown in the previous figures. In the case of the LCL-S-S configuration, it offers the ZPA of the input impedance phase $Z_{in}$ mentioned if both $L_s$ and $L_1$ are the same. Although if the condition is not met, the LCL-S-S loses LIO, but it has a small variation of the $\overline{I}_1$ for no-coupling condition. On the other hand, the LCC-S-S configuration presents the same characteristics as LCL-S-S, however both $L_s$ and $L_1$ do not need to be equal, presenting an advantage comparing with LCL-S-S.

For CV and CC mode of battery charging, the S-S-S topology exhibits an exponential decay behaviour for the ORMC mutual inductance $L_{12}$. Although, it presents an output voltage independent load value for each value of $L_{12}$ and it was validated in [31], enabling the SIPT with a constant output voltage. On the other hand, LCL-S-S and LCC-S-S do not present any independence for CV, although both topologies present a constant output current for each $L_{12}$ value and overall, presenting a linear behaviour if LCL-S-S is fulfilled the condition of self-inductances. Once more, the LCC-S-S does not need to fulfill the mentioned condition and it is not restraint like the LCL-S-S.

According to the $R_{eq}$ power, the S-S-S configuration enables higher values for smaller $L_{12}$ values and decreases with the increase of the same variable. Alternatively, LCL-S-S and LCC-S-S exhibit an exponential behaviour with the increase of $L_{12}$.

Table 3.3: Comparison of the three resonant configurations

| Parameter \ Topology | S-S-S | LCL-S-S | LCC-S-S |
|---|---|---|---|
| Independence on $L_{12}$ and $R_{eq}$ for ZPA | Yes | Yes and LIO if $L_s = L_1$ | Yes and LIO |
| Zero coupling allowance ($\overline{I}_1$ constant) | No | Yes and LIO if $L_s = L_1$ | Yes and LIO |
| Independence on $L_{12}$ and $R_{eq}$ for CV | Exponential decay for $L_{12}$ and LIO | No | No |
| Independence on $L_{12}$ and $R_{eq}$ for CC | No | Linear for $L_{12}$ and LIO, if $L_s = L_1$ | Linear for $L_{12}$ and LIO |
| $R_{eq}$ power | Exponential decay for $L_{12}$ | Exponential growth for $L_{12}$, if $L_s = L_1$ | Exponential growth for $L_{12}$ |

# 4 Simulation and analysis of system model results

In this chapter, the validation of the mathematical equations is made comparing theoretical and simulated electric results under fundamental harmonic component, comparing also the electric results under fundamental harmonic component and square wave condition using MATLAB and MATLAB/Simulink softwares. In addition, behavioural analysis of the aforementioned resonant configurations under different coupling conditions is made to assess the applicability of the new proposed topologies for DIPT operation compared with the basic S-S-S topology. Furthermore, the experimental results using LCL-S-S resonant power converter are presented to validate safe operation for the full range of coupling and load operating conditions, full to no-coupling (inherent to dynamic mode).

## 4.1 Simulation model analysis

In order to validate the mathematical models of the resonant configurations and the electrical circuits analysis, an implementation of MATLAB/Simulink was done. According to Fig. 4.1, three electric circuit models are built to simulate the equivalent circuits of three topologies previously studied, considering the electric and magnetic components depicted in Chapter 3.1 and illustrated in Fig. 3.2.

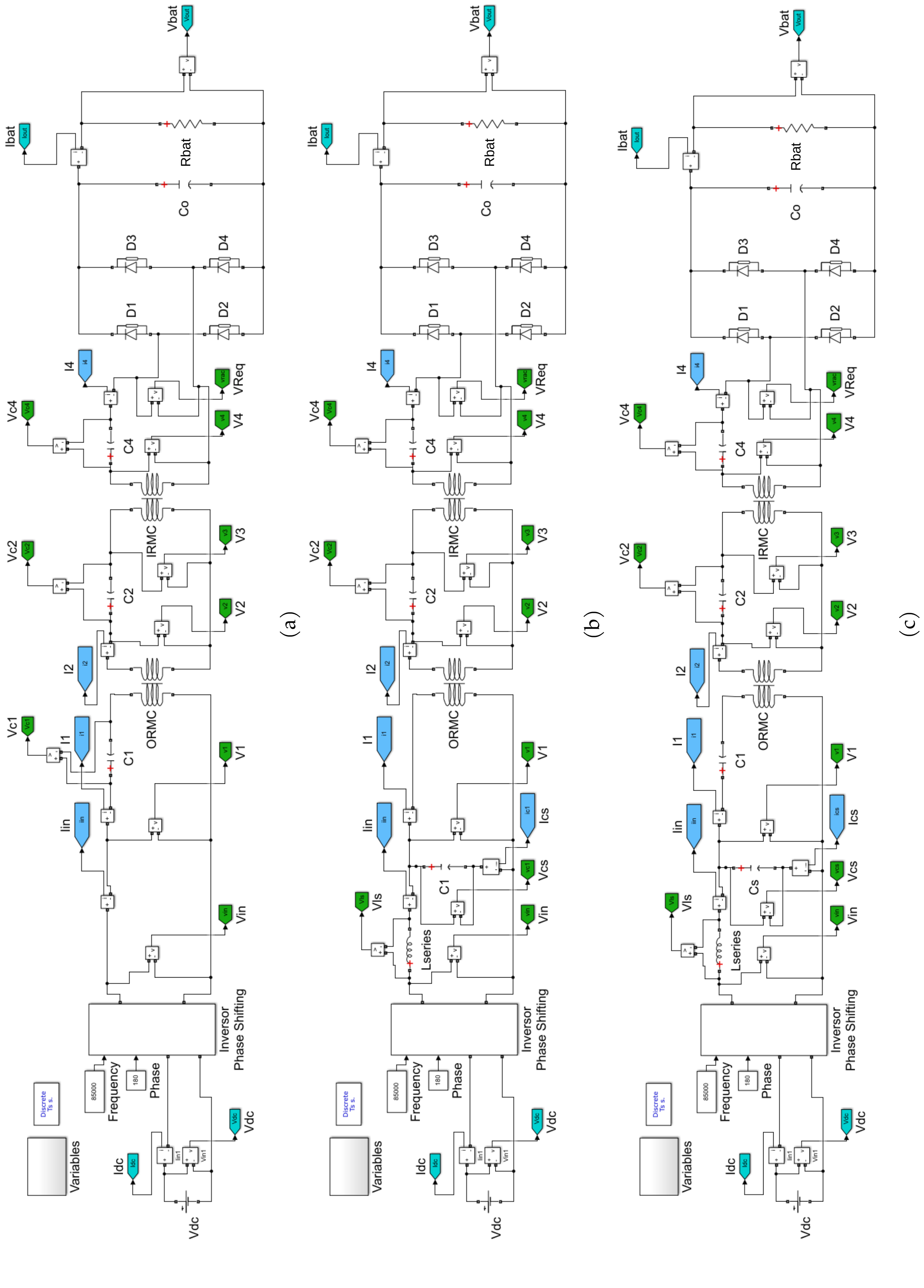


Figure 4.1: Simulation model of the equivalent electrical circuit of the proposed system with different resonant compensations in MATLAB/Simulink for: (a) S-S-S topology, (b) LCL-S-S topology and (c) LCC-S-S topology.

Table 4.1: Electrical and magnetic specifications for the inWIPT simulation model

| Parameter | Value |
|---|---|
| Electrical system specifications | |
| $V_{DC}$ | 200 V (from $1\phi$ grid) |
| $f_s$ | 85 kHz |
| $C_s$ (LCC-S-S) | 82.17 $nF$ |
| $C_1$ (LCC-S-S) | 82.09 $\mu F$ |
| $C_1$ (S-S-S and LCL-S-S) | 82.09 $nF$ |
| $C_2$ | 61.62 $nF$ |
| $C_4$ | 253.50 $nF$ |
| $R_{bat}/R_{eq}$ | 2.4/1.9 $\Omega$ |
| Magnetic system specifications | |
| $k_{12}$ | 0.147 |
| $k_{34}$ | 0.460 |
| $L_{12}$ | 6.1 $\mu H$ |
| $L_{34}$ | 6.9 $\mu H$ |
| $L_s$ | 42.67 $\mu H$ |
| $L_1$ | 42.71 $\mu H$ |
| $L_2$ | 40.45 $\mu H$ |
| $L_3$ | 16.45 $\mu H$ |
| $L_4$ | 13.83 $\mu H$ |
| Simulation model specifications | |
| $T_{stop}$ | 0.2 and 0.3 $s$ |
| $T_{step}$ | $T/200$ and $T/500$ $s$ |

In this way and with the support of the MATLAB/Simulink software, the electric circuits under study are implemented using the existing blocks in the Simscape Electrical library. Fig. 4.1 represents three different simulation models, with the different resonant configurations. In each one, there is a block named "Inversor Phase Shifting". This block represents the HF H-bridge inverter responsible for regulating the output frequency and providing the square wave signal to be applied to each resonant tank. To simulate only the fundamental harmonic component, the AC source signal block with the specific electrical setup can be used. Moreover, the input, ORMC and IRMC transmitter and receiver meshes for each resonant configuration, are built with self-inductances and their equivalent resistance, capacitors and equivalent resistance $R_{eq}$. To represent the MC structures, within the Simscape Electrical library, a MATLAB/Simulink block was used to represent the dependent voltage sources for self and mutual inductances. The magnetic fixed values together with the other electric components and the remaining specifications of the proposed system for the simulation are presented in Table 4.1. On the right side of each circuit in Fig. 4.1, it is presented an output HF AC-DC converter with a capacitor and a load resistor to represent the battery. The fundamental harmonic component analysis was made to validate the mathematical equations of the resonant configurations and assess their intrinsic characteristics and other variables. However, the square wave condition analysis was made to measure the electric variables and assess the performance of the system close to the real implementation scenario.

Through simulations of the MATLAB/Simulink models presented in Fig. 4.1, it was possible to obtain the results shown in Table 4.2 and Table 4.3. These simulations were made considering operation at resonance with ideal conditions ($r_s = r_1 = r_2 = r_3 = r_4 = 0\ \Omega$). Therefore, the capacitors were calculated considering resonance operation in the full-coupling condition $L_{12_{max}}$ as explained in Chapter 3.

According to Table 4.2, a comparative analysis was made for the results of RMS currents and their phases in MATLAB and the results obtained in MATLAB/Simulink using the simulated electric model with the AC fundamental component block. In addition, this analysis considers $L_{12} = 100\ \%$ (full-coupling condition), demonstrating the scenario when the wheel is aligned. The results allow validating the mathematical equations, while evaluating the associated error between them. According to these obtained results, both theoretical and simulated values are approximately equal and their associated error is minimal.

Table 4.3 presents another comparative analysis for the results of RMS currents, voltages and power under fundamental harmonic component and using the square wave signal, and their associated error, for the same operating conditions (resonance and full-coupling). This analysis was performed to compare the differences between the simulations using only an AC source and $R_{eq}$ opposed to considering all harmonic components through an inverter and output rectifier with $R_{bat}$, according to the real-implemented scenario. As a result, Table 4.3 presents a considerable deviation of results between the results generated under the fundamental harmonic component and the square wave input signal. This is explained due to the sum of harmonic components with the fundamental harmonic component, which introduces a considerable deviation. These deviations are even higher when the respected waveforms are highly distorted.

Table 4.2: Results of the RMS currents and phases in MATLAB and MATLAB/Simulink under the fundamental harmonic component

| | S-S-S | | | LCL-S-S | | | LCC-S-S | | |
|---|---|---|---|---|---|---|---|---|---|
| | Theoretical | Simulated | Error | Theoretical | Simulated | Error | Theoretical | Simulated | Error |
| $I_{in_{RMS}}$ | 132.57 A | 132.6 A | 0.027 % | 0.580 A | 0.580 A | - % | 0.581 A | 0.581 A | - % |
| $I_{1_{RMS}}$ | 132.57 A | 132.6 A | 0.027 % | 8.768 A | 8.769 A | 0.011 % | 8.777 A | 8.778 A | 0.011 % |
| $I_{2_{RMS}}$ | 61.29 A | 61.28 A | 0.016 % | 4.054 A | 4.054 A | - % | 4.058 A | 4.058 A | - % |
| $I_{4_{RMS}}$ | 116.75 A | 116.7 A | 0.043 % | 7.721 A | 7.722 A | 0.013 % | 7.729 A | 7.730 A | 0.013 % |
| $\theta I_{in}$ | 0.000 ° | 0.530 ° | - | 0.004 ° | -0.920 ° | - | 0.000 ° | 0.178 ° | - |
| $\theta I_1$ | 0.000 ° | 0.530 ° | - | -89.996 ° | -90.399 ° | 0.021 % | -90.000 ° | -90.028 ° | 0.031 % |
| $\theta I_2$ | 90.000 ° | 89.924 ° | 0.085 % | 0.004 ° | -0.995 ° | - | 0.000 ° | -0.596 ° | - |
| $\theta I_4$ | 180.000 ° | 179.904 ° | 0.053 % | 90.004 ° | 88.984 ° | 0.715 % | 90.000 ° | 89.386 ° | 0.682 % |

Table 4.3: Results of the RMS voltages and currents, and average powers in MATLAB/Simulink under the fundamental harmonic and the $n_{th}$ harmonic components

| | S-S-S | | | LCL-S-S | | | LCC-S-S | | |
|---|---|---|---|---|---|---|---|---|---|
| | Fund. Component | $n_{th}$ Components | Error | Fund. Component | $n_{th}$ Components | Error | Fund. Component | $n_{th}$ Components | Error |
| $V_{C_{s_{RMS}}}$ | - V | - V | - % | - V | - V | - % | 200.5 V | 181.7 V | 10.35 % |
| $V_{C_{1_{RMS}}}$ | 3024 V | 2701 V | 11.96 % | 200.5 V | 181.7 V | 10.37 % | 0.2002 V | 0.6081 V | 67.07 % |
| $V_{C_{2_{RMS}}}$ | 1862 V | 1668 V | 11.63 % | 123.2 V | 122.1 V | 0.90 % | 123.3 V | 122.2 V | 0.90 % |
| $V_{C_{4_{RMS}}}$ | 862.2 V | 769.4 V | 12.06 % | 57.03 V | 51.29 V | 11.19 % | 57.09 V | 51.39 V | 11.09 % |
| $V_{DC_{RMS}}$ | - V | 200 V | - % | - V | 200 V | - % | - V | 200 V | - % |
| $I_{DC_{RMS}}$ | - A | 118.4 A | - % | - A | 1.222 A | - % | - A | 1.274 A | - % |
| $P_{DC}$ | - W | 2.13E4 W | - % | - W | 104.1 W | - % | - W | 109.1 W | - % |
| $V_{in_{RMS}}$ | 200 V | 199.8 V | 0.10 % | 200 V | 200 V | 0 % | 200 V | 200 V | 0 % |
| $I_{in_{RMS}}$ | 132.6 A | 118.4 A | 11.99 % | 0.58 A | 1.221 A | 52.49 % | 0.5812 A | 1.273 A | 53.34 % |
| $P_{in}$ | 2.65E4 W | 2.13E4 W | 24.75 % | 116 W | 103.7 W | 11.86 % | 116.2 W | 108.7 W | 6.89 % |
| $V_{L_{s_{RMS}}}$ | - V | - V | - % | 13.22 V | 94.96 V | 86.07 % | 13.24 V | 95.00 V | 86.06 % |
| $I_{1_{RMS}}$ | 132.6 A | 118.4 A | 11.99 % | 8.769 A | 7.896 A | 11.05 % | 8.778 A | 7.911 A | 10.95 % |
| $I_{C_{s_{RMS}}}$ | - A | - A | - % | - A | - A | - % | 8.798 A | 8.06 A | 9.16 % |
| $I_{C_{1_{RMS}}}$ | 132.6 A | 118.4 A | 11.99 % | 8.789 A | 8.051 A | 9.17 % | 8.778 A | 7.911 A | 10.95 % |
| $V_{1_{RMS}}$ | 3031 V | 2719 V | 11.47 % | 200.5 V | 181.7 V | 10.35 % | 200.7 V | 181.9 V | 10.33 % |
| $I_{2_{RMS}}$ | 61.28 A | 54.86 A | 11.70 % | 4.054 A | 4.02 A | 0.84 % | 4.058 A | 4.021 A | 0.92 % |
| $V_{2_{RMS}}$ | 1393 V | 1269 V | 9.77 % | 92.13 V | 92.52 V | 0.42 % | 92.22 V | 92.47 V | 0.27 % |
| $V_{3_{RMS}}$ | 690.5 V | 602 V | 14.70 % | 45.67 V | 42.24 V | 8.12 % | 45.72 V | 42.28 V | 8.13 % |
| $I_{4_{RMS}}$ | 116.7 A | 104.2 A | 11.99 % | 7.722 A | 6.952 A | 11.07 % | 7.73 A | 6.934 A | 11.47 % |
| $V_{4_{RMS}}$ | 891.6 V | 794.7 V | 12.19 % | 58.98 V | 53.15 V | 10.96 % | 59.04 V | 53.10 V | 11.18 % |
| $V_{R_{eq_{RMS}}}$ | 227.1 V | 226.1 V | 0.44 % | 15.02 V | 16.49 V | 8.91 % | 15.04 V | 16.51 V | 8.90 % |
| $P_{R_{eq}}$ | 2.65E4 W | 2.12E4 W | 25.28 % | 116 W | 102.9 W | 12.73 % | 116.2 W | 102.6 W | 13.25 % |
| $I_{R_{bat\,RMS}}$ | - A | 93.53 A | - % | - A | 6.218 A | - % | - A | 6.224 A | - % |
| $V_{R_{bat\,RMS}}$ | - V | 224.5 V | - % | - V | 14.92 V | - % | - V | 14.94 V | - % |
| $P_{R_{bat}}$ | - W | 2.10E4 W | - % | - W | 92.78 W | - % | - W | 92.98 W | - % |

After this initial analysis, an assessment was made regarding output batteries power ($P_{R_{bat}} = \int (v_{R_{bat}} \times i_{R_{bat}})\, dt$) for all resonant configurations. This assessment considers the real implementation scenario (square wave and output rectifier and calculated capacitor values at full-coupling). The following results were obtained through multiple simulations generated in MATLAB/Simulink software. These simulations were made under a full range of ORMC mutual inductance $L_{12}$ (transition between full-coupling to no-coupling modes) using the nominal resistance value $R_{bat} = 2.4\,\Omega$ as shown in Fig 4.2 (a) and Fig 4.2 (b) and three battery resistance values $R_{bat}$ (2.4 Ω, 25 Ω and 100 Ω) as shown in Fig 4.2 (c) and Fig 4.2 (d). Each figure considers different percentages of self-inductance $L_s$ (10 %, 25 %, 50 % and 99.9 %). In the real implemented scenario, since the design of the pads affects the magnetic pads parameters, it is relevant to assess different situations for designing a better system. For a better display (scale), it was generated two plots (a and b or c and d) with similar information. Fig. 4.2 (a) and Fig. 4.2 (c) allow comparing the scenario with all topologies. Fig. 4.2 (b) and Fig. 4.2 (d) only show the hybrid topologies (LCL-S-S and LCC-S-S).

In case of Fig. 4.2 (a), the S-S-S topology presents higher values of batteries power $P_{bat}$ for all conditions, however, this topology is not a viable solution for the DIPT operation due to the high circulating currents in no-coupling mode. The LCC-S-S topology exhibits higher values of $P_{bat}$ for conditions with self-inductance $L_s$ lower than self-inductance $L_1$, compared with the LCL-S-S topology for all conditions in Fig. 4.2 (b). Moreover for the LCL-S-S topology to operate in resonance, it must fulfill the condition of equality between both self-inductances $L_s$ and $L_1$. In contrast, the LCC-S-S topology does not present this condition and for lower values of $L_s$, it presents a better option for

DIPT operation. According to Fig. 4.2 (c), the S-S-S topology shows the lower values of the battery power $P_{bat}$ under all conditions. In Fig. 4.2 (d), the LCC-S-S topology demonstrates higher values of $P_{bat}$ for conditions with the self-inductance $L_s$ lower than the self-inductance $L_1$, comparing with the LCL-S-S topology for all conditions.

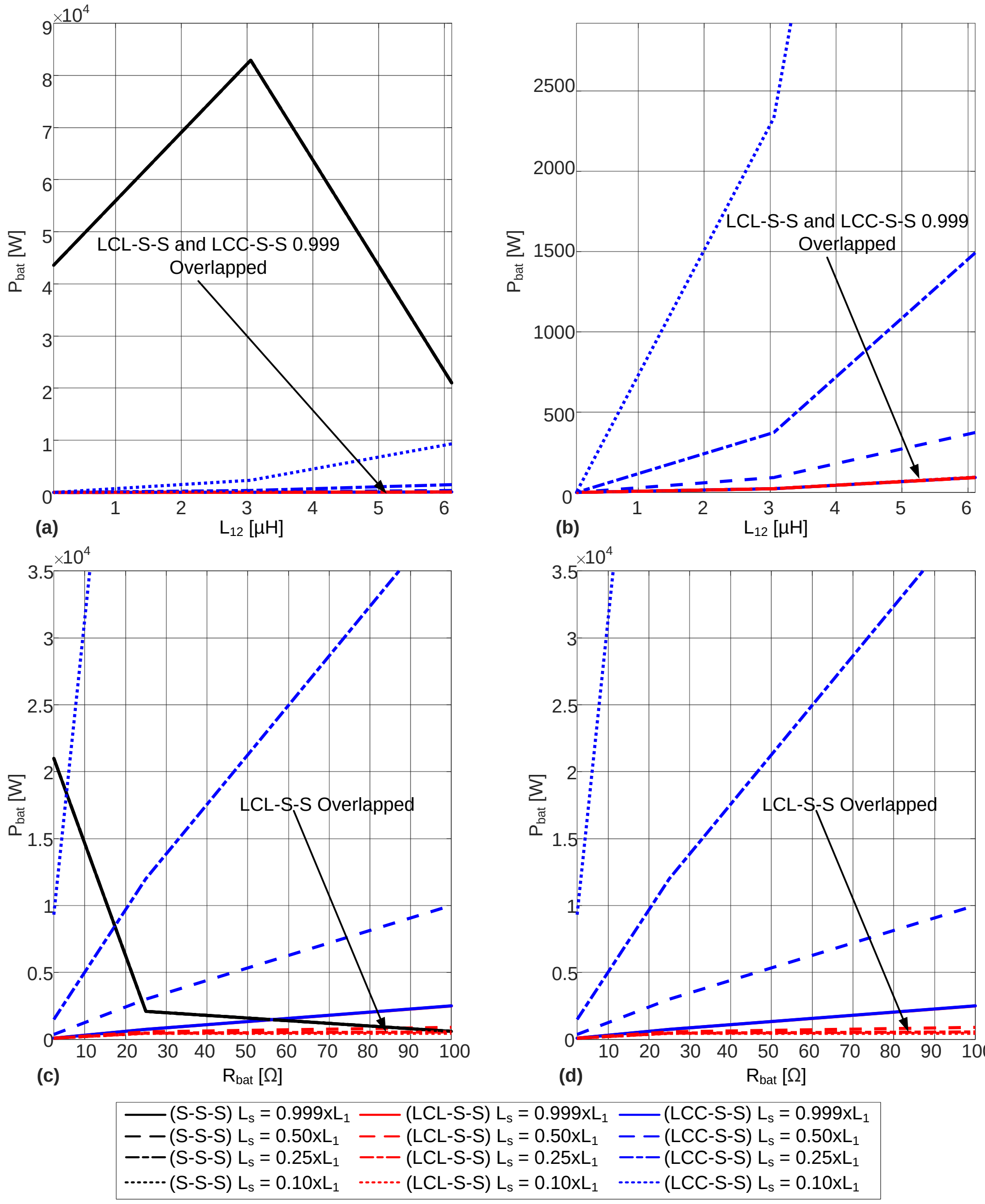


Figure 4.2: MATLAB plots using different percentages for $L_s$ for: (a) $P_{bat}$ with all resonant topologies and (b) $P_{bat}$ with LCL-S-S and LCC-S-S as function of mutual inductance of ORMC $L_{12}$, and (c) $P_{bat}$ with all resonant topologies and (d) $P_{bat}$ with LCL-S-S and LCC-S-S as function of battery resistances $R_{bat}$ and full-coupling mode $L_{12_{max}}$.

## 4.2 Operational waveforms

The electric circuits models in Fig. 4.1, are simulated to analyse the operational waveforms for currents, voltages and output power in both DIPT scenarios when $L_{12} = 100~\%$ (full-coupling condition) and $L_{12} = 1~\%$ (no-coupling condition). Fig. 4.3 (a), Fig. 4.3 (b) and Fig. 4.3 (c) correspond, respectively, to the S-S-S, LCL-S-S and LCC-S-S topologies, when the wheel is aligned with the outside pad embedded with the road ($L_{12} = 100~\%$). Fig. 4.4 (a), Fig. 4.4 (b) and Fig. 4.4 (c) correspond, respectively, to the S-S-S, LCL-S-S and LCC-S-S topologies, when the wheel is not coupled with the outside pad embedded with the road ($L_{12} = 1~\%$).

Considering the selected magnetic parameters, it is possible to observe from Fig. 4.3 (a), that the results for the S-S-S, already show high values for the voltages, currents and output power. In comparison, Fig. 4.4 (a) shows even higher values. These results are explained due to the transition of the system from full-coupling condition to a no-coupling condition in the first MC (ORMC), resulting in a decrease of $|Z_{in}|$ for lower coupling values, which means $k_{12} \to 0$, leading to $|Z_{in}| \to 0$. Therefore, it results in high transmitter currents, making the S-S-S topology undesirable for DIPT applications and validating the plots of Fig. 3.5 (b) and Fig. 3.5 (e).

In case of the S-S-S output power $P_{bat}$, it is inversely dependent of the ORMC mutual inductance $L_{12}$. As previously presented in Fig. 3.5 (f), it presents an exponential growth with a decrease of $L_{12}$. As a result, between the both mentioned conditions, the output power will increase significantly.

On the other hand, LCL-S-S and LCC-S-S present a natural current limiting $\overline{I}_1$ behaviour as shown in Fig 4.3 (b) and Fig 4.3 (c), and Fig 4.4 (b) and Fig 4.4 (c), when there are different coupling conditions. This is explained by an increase of $|Z_{in}|$ for low coupling values, which means that $k_{12} \to 0$ leads to $|Z_{in}| \to \infty$. The input current $\overline{I}_{in}$, in both topologies, is not sinusoidal due to the $\overline{V}_{in}$ harmonics (square wave voltage), although this effect can be minimized if the inverter phase-shift angle is adjusted to reduce the current total harmonic distortion (THD), improving the efficiency of the converter.

In addition, both topologies present approximately the same voltages and currents due to the equality between the $L_s$ and $L_1$. If these values were considerably different, the LCL-S-S would still show the CC characteristic, but would lose LIO.

Moreover, the IRMC receiver current $\overline{I}_4$ on both hybrid topologies has shown an independence of the equivalent resistance $R_{eq}$ and exhibited a linear behaviour for a range of $L_{12}$ values. For both conditions, $|\overline{I}_4|$ is constant and in no-coupling condition, the waveform presents a distortion due to absence of the EV, therefore there is a small variation of values.

For output power $P_{bat}$, the LCL-S-S and LCC-S-S have a similar range of values due to equality of $L_s$ and $L_1$, showing a small deviation between the hybrid topologies and the LCC-S-S has a higher power than LCL-S-S. Nevertheless, the difference is very low due to the considered magnetic parameters of the system.

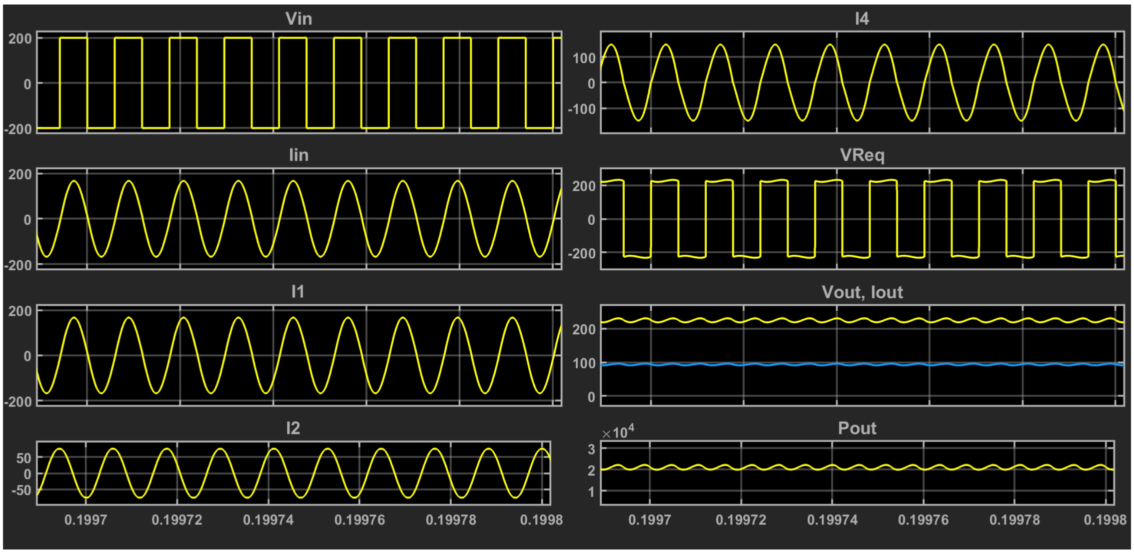


(a)

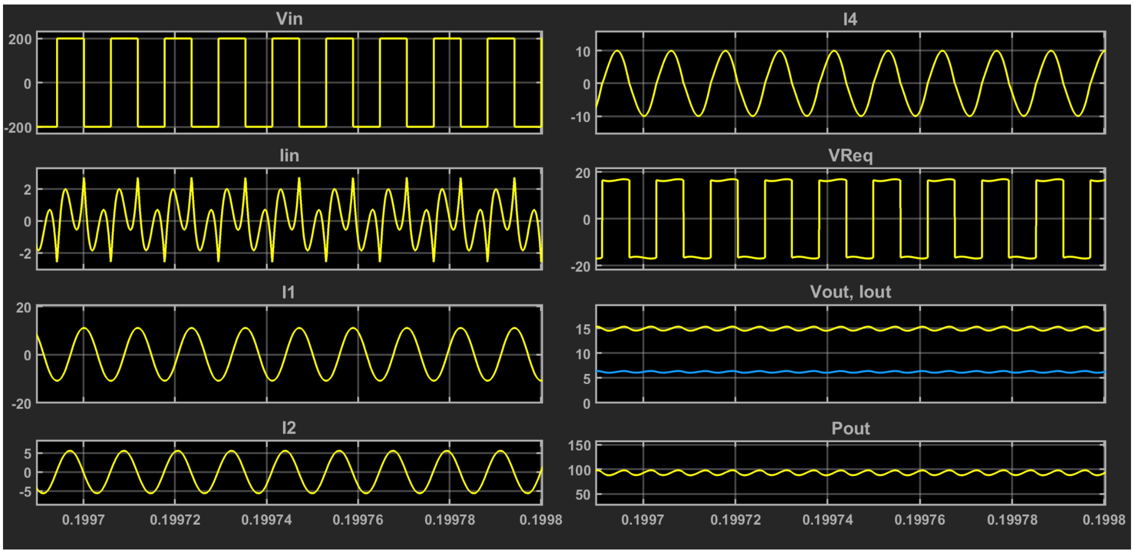


(b)

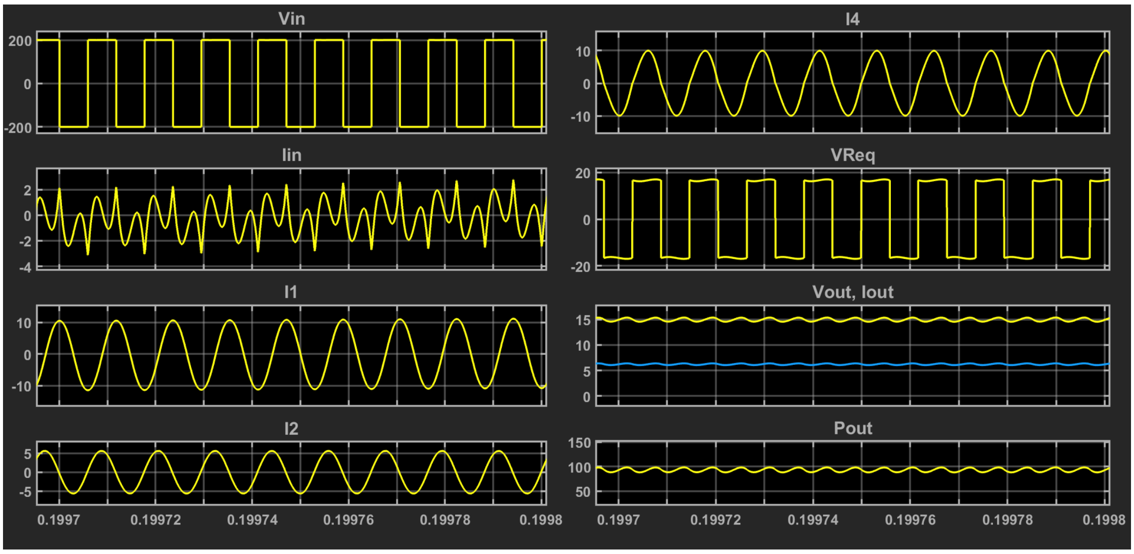


(c)

Figure 4.3: Simulation results for the double coupling inWIPT, considering $L_{12} = 100\,\%$ (full-coupling condition) for: (a) S-S-S topology, (b) LCL-S-S topology and (c) LCC-S-S topology.

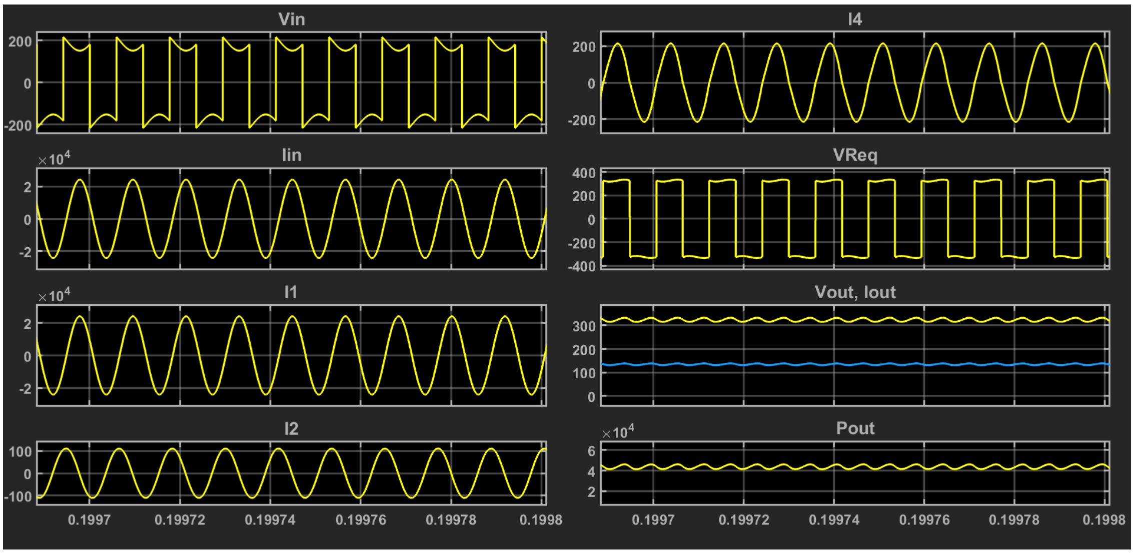


(a)

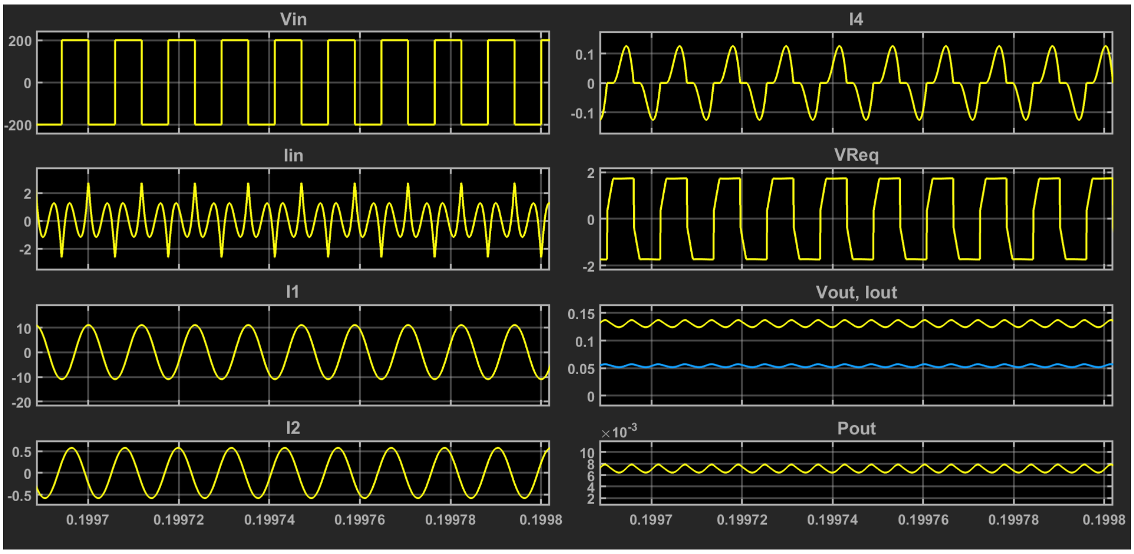


(b)

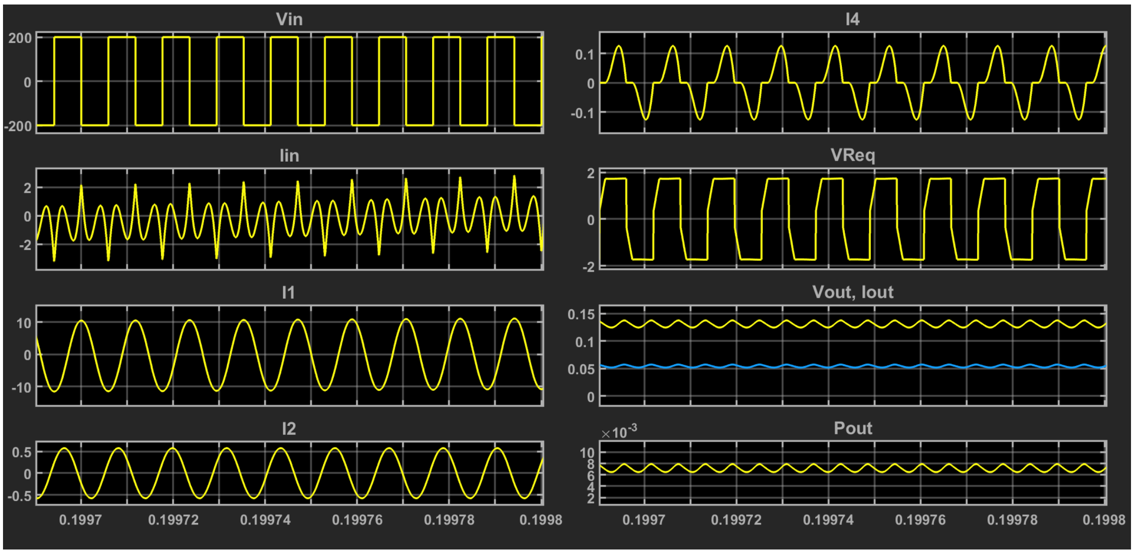


(c)

Figure 4.4: Simulation results for the double coupling inWIPT, considering $L_{12} = 1\ \%$ (no-coupling condition) for: (a) S-S-S topology, (b) LCL-S-S topology and (c) LCC-S-S topology.

In order to present some dynamic behaviour, another simulation is presented in Fig. 4.5. This figure corresponds to another electric circuit model simulated in MATLAB/Simulink, which introduces a scenario with a transition of full-coupling to no-coupling conditions. This model was made by another student from the inWheel project team. This specific simulation includes a lookup table that emulates the changing mutual inductance profile according to the EV movement. Therefore, it can simulate two scenarios when the wheel is aligned with the off-board pad and when it is not aligned, varying the ORMC mutual inductance $L_{12}$. In addition, the three plots of Fig. 4.5 were simulated to have the transition of full-coupling to no-coupling condition at the time instant of 0.25 $s$ of the selected $T_{stop}$. In overall, these simulations are made using the inWIPT system connected with a HF H-bridge inverter to introduce a square wave signal and an output rectifier with the $R_{bat}$ to represent a SoC of the equivalent battery of the EV and other system specifications presented in Table 4.1.

In reference to Fig. 4.5, the three plots validate what was previously mentioned about the natural current limiting operation for $\overline{I}_1$ presented in both hybrid topologies and the absence of it in the S-S-S topology. In Fig. 4.5 (a), there is an exponential growth of all voltages and currents at $T = 0.25\ s$, specifically in both off-board input and transmitter currents $\overline{I}_{in}$ and $\overline{I}_1$. In contrast, LCL-S-S and LCC-S-S topologies show a small variation of the mentioned currents between both full and no-coupling conditions as illustrated in Fig. 4.5 (b) and Fig. 4.5 (c). Therefore, it is verified the applicability of both hybrid topologies in DIPT operation. Additionally, it is expected the a significantly decrease of on-board voltages and currents due to the absence of the EV.

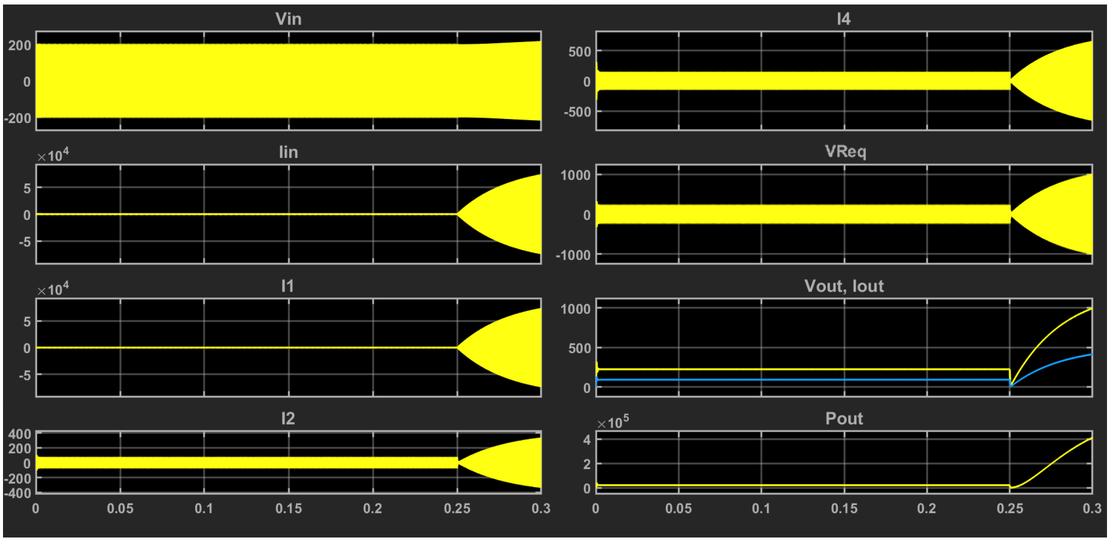


(a)

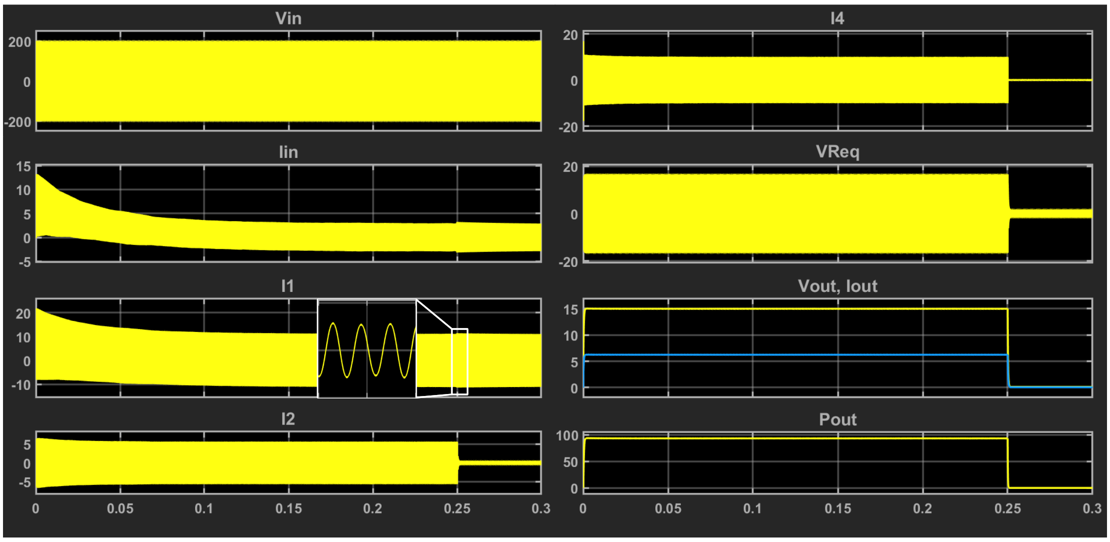


(b)

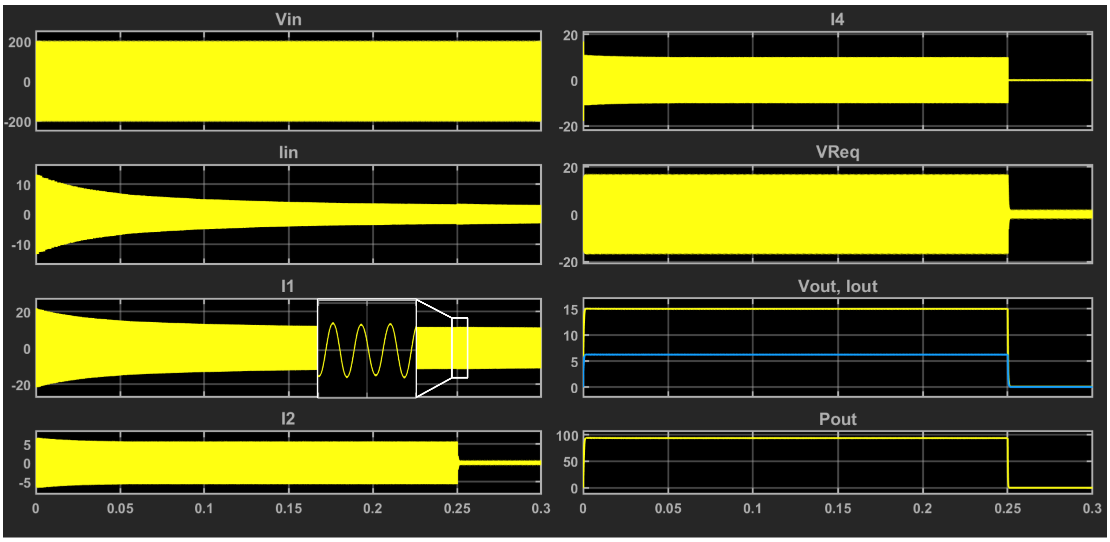


(c)

Figure 4.5: Simulation results for the double coupling inWIPT, considering variation of $L_{12}$ for: (a) S-S-S topology, (b) LCL-S-S topology and (c) LCC-S-S topology (Used MATLAB/Simulink model not shown in this study).

## 4.3 Experimental analysis

*The work presented in this section was done under the framework of the Project inWheel Inductive Power Charging for Sustainable Mobility with reference 2022.06192.PTDC. and it was conducted with collaboration of all team members. This experimental tests have led to the publication of a paper in the ECCE 2023 conference [51].*

The double coupling inWIPT prototype using an LCL-S-S resonant power converter is built and tested, as in Fig. 4.6 to validate the previous analysis of LCL-S-S and its electrical and magnetic parameters are presented in Table 4.4. The experimental prototype presents the same electric circuit as illustrated and explained in Fig. 3.2 (b) and Fig. 4.1 (b). The MC configurations consider a structure built with IRMC of solenoid pad (SP)-SP configuration in both transmitter and receiver sides, mounted in aluminium shields and the coil diameters are, $d_{L3} = 360\ mm$ and $d_{L4} = 320\ mm$. Inside of shields, 12 equally spaced ferrite cores of 43x24x4 $mm.$ are placed and the IRMC contains an air gap $g_{34} = 20\ mm.$ The transmitter and receiver have 8 and 6 turns, respectively. Furthermore, the ORMC is built using bipolar pad (BPP)-BPP configuration with a transmitter containing two coils of 10 turns without ferrite cores. The ORMC receiver is also placed around the outer perimeter of an aluminium rim, with 12 spaced ferrite cores of 129x24x4 $mm.$ and having two coils with 8 turns and a radius $r_{L2} = 250\ mm.$ The air gap between ORMC is $g_{12} \approx 20\ mm.$

The proposed system is supplied with a DC bus, which is generated via rectifier fed

Table 4.4: Electrical and magnetic specifications for the inWIPT experimental prototype system

| Parameter | Value |
|---|---|
| Electrical system specifications | |
| $V_{DC}$ | 200 V (from $1\phi$ grid) |
| $f_s$ | 85 kHz |
| $C_1$ | 82.5 $nF$ |
| $C_2$ | 62.2 $nF$ |
| $C_4$ | 252.6 $nF$ |
| Magnetic system specifications | |
| $k_{12}$ | 0.14 |
| $k_{34}$ | 0.46 |
| $L_{12}$ | 6.1 $\mu H$ |
| $L_{34}$ | 7.1 $\mu H$ |
| $L_s$ | 43.5 $\mu H$ |
| $L_1$ | 42.7 $\mu H$ |
| $L_2$ | 40.5 $\mu H$ |
| $L_3$ | 16.5 $\mu H$ |
| $L_4$ | 13.8 $\mu H$ |

by an autotransformer connected to the electrical grid. The HF power supply represents the H-bridge inverter, using C3M0065090D SiC MOSFETs controlled with a digital signal processor (DSP) from Texas Instruments TMDSCNCD28335 and gate drivers PT62SCMD17 from CREE/Wolfspeed. Furthermore, the output signal of the inverter is supplying the inWIPT electric circuit implemented, firstly in the input inductor $L_s$ and ORMC transmitter pad made by copper wire, and ORMC receiver pad and IRMC made by Litz wire, used in order to avoid problem of losses and skin effect at high frequency. Lastly, the output signal of the IRMC receiver is converted to a DC signal through a output rectifier and connected with a resistive load, representing one SoC of the battery. The output H-bridge rectifier uses C2M0080120D Sic MOSFETS that includes anti-parallel diodes. For data acquisition, it was used Tektronix oscilloscope, voltage and current probes are used to obtain the experimental results.

The input of the converter is fed by a full-bridge square wave inverter, $V_{DC} = 200\ V$ and considers at the output a HF full-bridge rectifier connected to a resistive load, $R_{bat}$. Experimental results considering full and no-coupling conditions are presented in Fig. 4.7 (a) and Fig. 4.7 (b). Yellow and blue waveforms represent the input voltage and current, $\overline{V}_{in}$ and $\overline{I}_{in}$, respectively. Pink waveform represents the current in the ORMC transmitter $\overline{I}_1$ and, green waveform represents the current at the IRMC receiver $\overline{I}_4$. Fig. 4.7 (a) considers full-coupling condition with a load $R_{bat}$ step $[2.4\ \Omega \rightarrow 4.8\ \Omega \rightarrow 2.4\ \Omega]$. The input current $\overline{I}_{in}$ is limited in the full range of coupling variation $0 < k_{12} < k_{12max}$ and the current is not sinusoidal as expected. In addition, $\overline{I}_1$ exhibits CC characteristics in the ORMC transmitter and remains approximately constant ($< 0.15\ \%$ variation) independent of coupling and load variations, in this case, $|\overline{I}_1| = 7.75\ A$ approximately. Furthermore, $\overline{I}_4$ remains approximately constant, with a variation at full-coupling around $< 15\ \%$, between the simulation with pads series resistances close to zero and experimental results. Experimentally the observed variation is natural due to the actual coils quality factor. These results allow validating the LCL-S-S double-coupling inWIPT ability for DIPT battery charging applications.

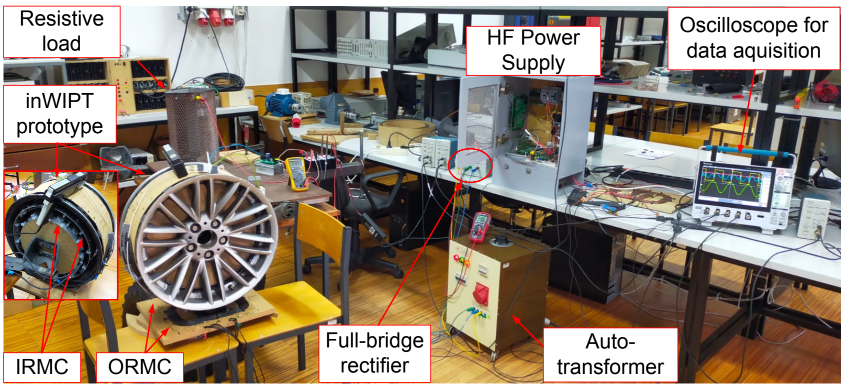


Figure 4.6: Double coupling inWIPT prototype with LCL-S-S resonant power converter.

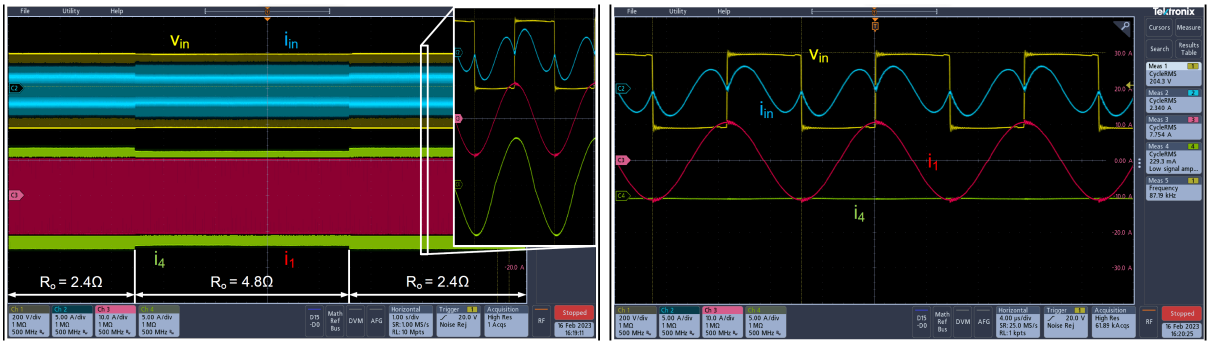


(a) Full-coupling condition with load-step

(b) No-coupling condition

Figure 4.7: Experimental results for the double coupling inWIPT with LCL-S-S resonant convert. $\overline{V}_{in}[200V/div]$ CH1 (yellow), $\overline{I}_{in}[5A/div]$ CH2 (blue), $\overline{I}_1[10A/div]$ CH3 (pink), $\overline{I}_4[5A/div]$ CH4 (green). (a) Time $[1s/div]$ and, (b) Time $[4\mu s/div]$

# 5 Characterization of different integrated pad geometries for in-Wheel EV IPT applications

This chapter presents the characterization of an embedded inWIPT system for on-board charging by considering multiple integrated pad geometries for ORMC and IRMC. The self and mutual inductance profiles of the different pad geometries were evaluated experimentally for different core and coil arrangements as a function of both vertical and lateral displacements and wheel's rotation. The MC characterization in terms of self and mutual inductances and coupling factor is made considering the impact of the space between turns, number of turns, volume of core and air gap, as well as vertical and lateral displacements and wheel's rotation. Different prototypes are built to perform behavioural analysis under different conditions.

## 5.1 Magnetic coupling experimental calculations and measurements

The characterization of the MC of an IPT system plays a crucial role that involves experimental measurements using specialized equipment such as LCR meter. These measurements are important for comprehending the MC profile of the system. It also allows the possibility of using this information for system design. This profile involves measuring and analysing factors such as self-inductance, mutual inductance and the coupling coefficient. Mutual inductance quantifies the magnetic coupling between the transmitter and receiver coils, while the coupling coefficient is related to the power transfer capability.

Based on the operating principle of a transformer, as shown in Fig. 2.1, the self-inductance of the transmitter and receiver windings will be measured. Using these measured values, the mutual inductance and coupling factor of the windings are calculated. The experimental mutual inductance and coupling factor is given by

$$L_T = L_1 + L_2 \pm 2.M \tag{5.1}$$

$$M_+ = \frac{L_{T_+} - L_1 - L_2}{2} \tag{5.2}$$

$$M_- = \frac{L_1 + L_2 - L_{T_-}}{2} \tag{5.3}$$

$$k_+ = \frac{M_+}{\sqrt{L_1.L_2}} \tag{5.4}$$

$$k_- = \frac{M_-}{\sqrt{L_1.L_2}} \tag{5.5}$$

where $L_T$ is the total inductance obtained, experimentally, by the series and anti-series connection $(L_{T_+}\ and\ L_{T_-})$ between transmitter and receiver windings. Fig. 5.1 illustrates the connections to measure the mentioned variables and the experimental measurement using LCR meter. For both $M_+, M_-$ and $k_+, k_-$, the selection of the mutual inductance $M$ and the coupling factor $k$ was done by calculating the average value between $M$ and $k$ values and therefore, it is used for the results of behaviour analysis.

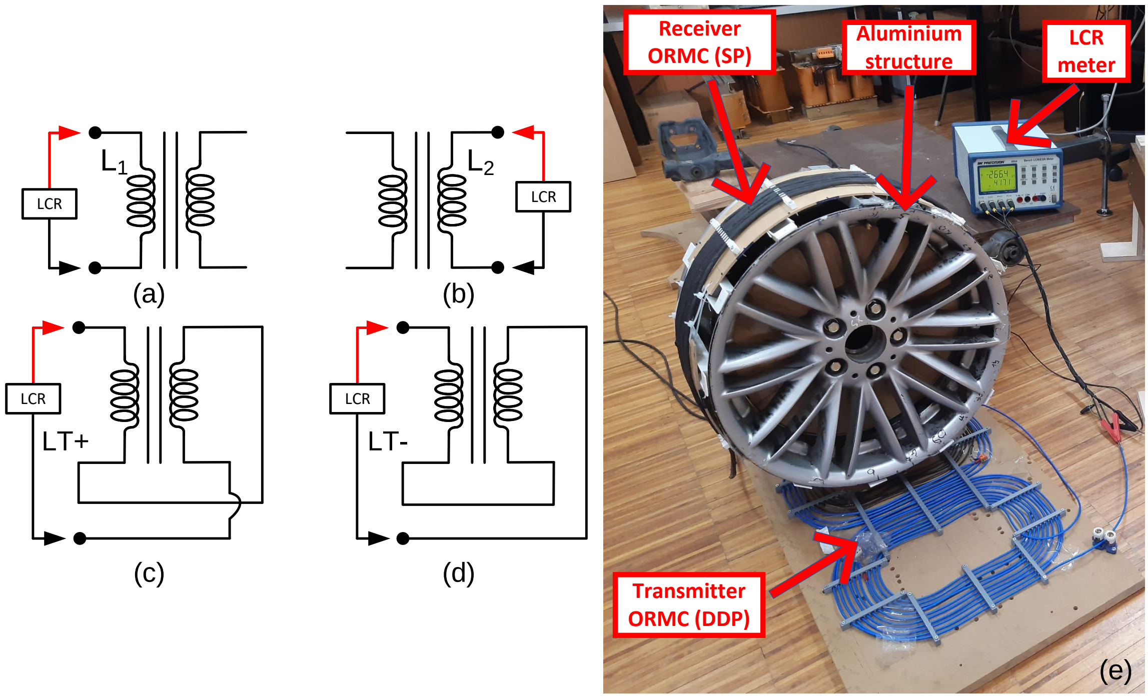


Figure 5.1: (a) Circuit to measure $L_1$, (b) circuit to measure $L_2$, (c) series circuit to measure $L_{T_+}$, (d) anti-series circuit to measure $L_{T_-}$ and (e) experimental measurement using LCR meter.

## 5.2 inWIPT configuration

The inWIPT, as previously stated, uses the wheel as an intermediary stage to transfer energy into the vehicle and ensuring, in the process, a low air gap almost independent of the vehicle type. To achieve this, two MCs (ORMC and IRMC) are used, maintaining a minimal air gap throughout the energy transfer process.

Therefore, conventional IPT systems geometries, like the Double-D pad (DDP), BPP or Circular pad (CP), can be applied in the transmitter pad of the ORMC. The application of the mentioned geometries on the receiver side results in different coupling values from conventional IPT systems due to the rim's curvature and must ensure a 360° coverage since the placement of the coils depends on the main flux path orientation of the transmitter pad. Furthermore, the ferromagnetic material is placed in the outer rim surface to mitigate the shield effect caused by the aluminium. Due to the advantages of the inWIPT ORMC from conventional IPT systems, this system has a lower air gap between the transmitter and receiver pads and it depends only of the thickness of the tyre and this value remains constant for majority of vehicle classes. Nevertheless, the wheel's rotation introduces a new degree of freedom which will influence the coupling profile of the ORMC, depending on the type of geometry and its placement around the rim. On the other hand, the air gap between the placement of transmitter and receiver pads of the IRMC is constant and independent of any charging positions. Therefore, the coupling factor remains constant and can be adjusted accordingly during the design to meet the system specifications.

### 5.2.1 IRMC and ORMC geometry selection

The cylindrical shape of the rim influences the coupling behaviour of the ORMC. In [52], the authors used an optimized version of the CP geometry in both pads. However, this geometry still does not entirely optimize the surface of the tyre and therefore, the wheel's rotation does not enable coupling charging scenarios, according to the relative position between the wheel and the transmitter pad. In this context, a receiver pad geometry named saddle BPP ($Sad_{BPP}$) [45] is used in this work. The $Sad_{BPP}$, demonstrated in Fig. 5.2, is composed by saddle coils (similar to those used in motors) overlapped and similar to a BPP, hence the $Sad_{BPP}$ designation. Moreover, this geometry presents a ferromagnetic material placed between the outer surface of the rim and coils to lower the shield effect of the aluminium and enable a single-sided magnetic flux pattern characteristics. On the other hand, the Double-D (DDP) geometry was selected for the transmitter side due to its interoperability with $Sad_{BPP}$. However, the orientation between both geometries must be along the $y$ axis according to the main flux pattern of $Sad_{BPP}$, as illustrated in Fig. 5.2.

The literature proposes several coupling designs for devices with similar functions of the IRMC like slip rings [53, 54, 55, 56] or underwater chargers for AGV [57, 58, 59]. The SP geometry was selected for the IRMC due to the constant coupling profile for rotary applications regardless of the relative positioning between the transmitter and receiver pads.

In a previous work, a characterization in terms of self and mutual inductances and coupling factors for the IRMC was made using a FEA tool named Flux. A 3D model of the IRMC was built, and the mentioned magnetic parameters were analysed for different geometries, operating conditions and volume of ferromagnetic core. These simulations

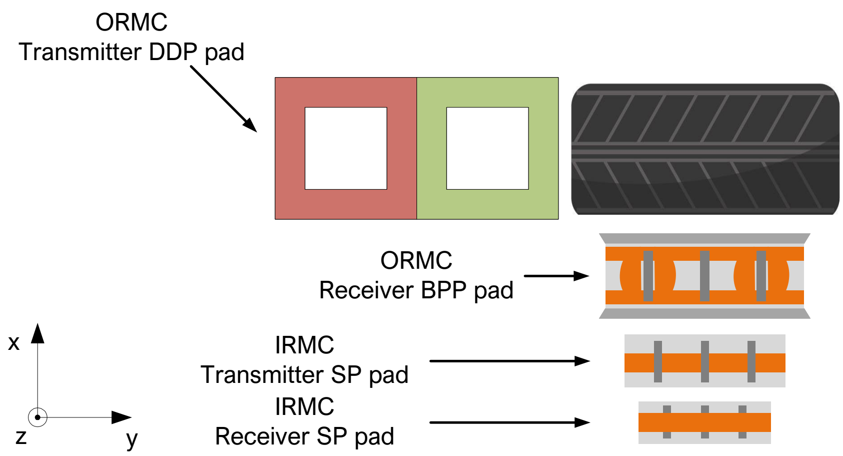


Figure 5.2: ORMC and IRMC placement on the wheel and roadway for the inWIPT system with DDP-BPP and SP-SP.

allowed a first approach and gave relevant information to consider and construct an experimental prototype of the inWIPT system. For the characterization presented here, certain variables and conditions such as the impact of the number of turns, volume of core, tolerance to both vertical (air gap) and lateral displacements (misalignments) and wheel's rotation were assessed, using a LCR meter for the measurements. Additionally, an experimental prototype was built taking into account the real implementation scenario. Therefore, the IRMC was mounted inside the aluminium rim and it is demonstrated in Fig. 5.3. These IRMC aluminium shields were used for magnetic shielding and provide a structure for the placement of the coil, presented in the bottom right corner in Fig. 5.3.

This system was built according to the following experimental setup specifications presented in Table 5.1. The variables expressed with $d_{L_4}, d_{L_3}, d_{L_2}$ present the length of both

Table 5.1: Experimental setup specifications

| Parameter | Value | Parameter | Value |
|---|---|---|---|
| IRMC: SP-SP | | ORMC receiver: BPP | |
| $d_{L3}$ ($g_{34a} = 15\ mm$) | $364\ mm$ | $d_{L2}$ ($g_{12} = 20\ mm$) | $530\ mm$ |
| $d_{L4}$ ($g_{34a} = 15\ mm$) | $322\ mm$ | $Coil_l$ | $390\ mm$ |
| $d_{L3}$ ($g_{34b} = 10\ mm$) | $359\ mm$ | $Coil_w$ | $142\ mm$ |
| $d_{L4}$ ($g_{34b} = 10\ mm$) | $327\ mm$ | $Coil_{lint}$ | $274\ mm$ |
| ORMC transmitter: DDP | | $Coil_{wint}$ | $28\ mm$ |
| $Coil_l$ | $280\ mm$ | $Coil_{lintcomb}$ | $554\ mm$ |
| $Coil_w$ | $390\ mm$ | $Coil_{loverlap}$ | $122\ mm$ |
| $Coil_{lint}$ | $115\ mm$ | $Coil_{lintoverlap}$ | $10\ mm$ |
| $Coil_{wint}$ | $220\ mm$ | | |
| $Coil_{lintcomb}$ | $395\ mm$ | | |

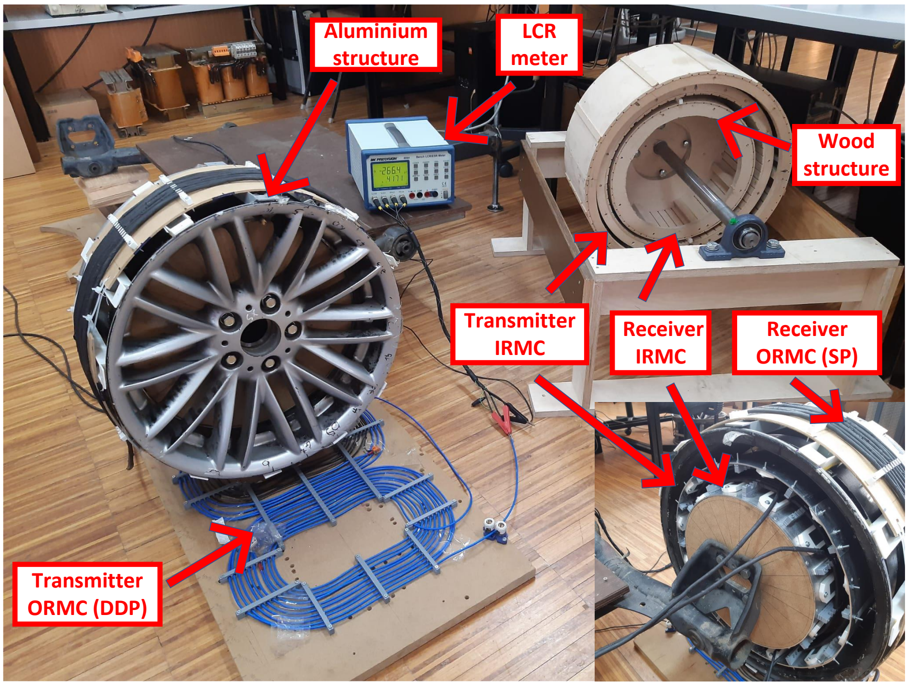


Figure 5.3: Experimental in-Wheel IPT setup. The aluminium structure is on the left, the preliminary wood structure is on the top right, and the back side of the aluminium structure on the bottom right corner.

IRMC transmitter and receiver, and ORMC receiver coils, respectively. Additionally, these variables were measured using certain air gaps of IRMC and ORMC represented with $g_{34a}, g_{34b}, g_{12}$, respectively. For DDP and BPP pad geometries, other parameters are presented to explain the dimensions of coils and are illustrated in Fig. 5.7 (a). The exterior length and width of the coils are expressed with $Coil_l, Coil_w$. On the other hand, the interior length and width of the coils are represented with $Coil_{lint}, Coil_{wint}$ and the combination between coils of the same pad geometry is expressed with $Coil_{lintcomb}$. In case of BPP geometry, it is also expressed variables to present the dimensions of the overlapped coils. Therefore, $Coil_{loverlap}, Coil_{lintoverlap}$ are overlapped length and interior length of BPP coils, respectively.

### 5.2.2 Inner rim magnetic coupler

For the IRMC, the assessment of the selected SP geometry is introduced with the analysis of different core arrangements, followed by the evaluation of size relations for both the ferromagnetic core and coil. The air gap for IRMC ($g_{34}$) is established between 10 and 15 $mm$ to ensure a safe distance regarding special scenarios during the experimental tests. Additionally, the ferromagnetic core is composed by the N87 material from Epcos and it was installed in the IRMC section of the prototype using holding cases for the cores. The cores increase the mutual inductance and coupling factor, which are low due to the significant magnetic reluctance of the large air gap and misalignment. Ferrite cores have high permeability in which magnetic fluxes can pass through easily, reducing the flux dispersion. Other requirements are the high resistivity and low hysteresis loss, due to high switching frequencies and the levels of power transferred [60].

In Fig. 5.4 (a) and Fig. 5.4 (b), the IRMC pad geometry and placement schematic is presented for two different views (Front view and Top view) and the real implementation and a close view of IRMC section for the following parameters, respectively. Both transmitter and receiver coils are represented by orange colour and the coils diameter are $d_{L3}$ and $d_{L4}$ respectively, and both coils are separated by $g_{34}$. The dark grey rectangles represent the 12 ferrite strips equally placed along the circumference formed by each SP. The light grey circles represent aluminium shields with double function: to provide electromagnetic shielding and to provide physical protection against external elements like dust or water. The Top view illustrated in Fig. 5.4 (a) shows the coil ($coil_w$) and ferrite ($core_w$) width together with the space between turns (SBT). These variables are varied to evaluate the values that offer better coupling factors.

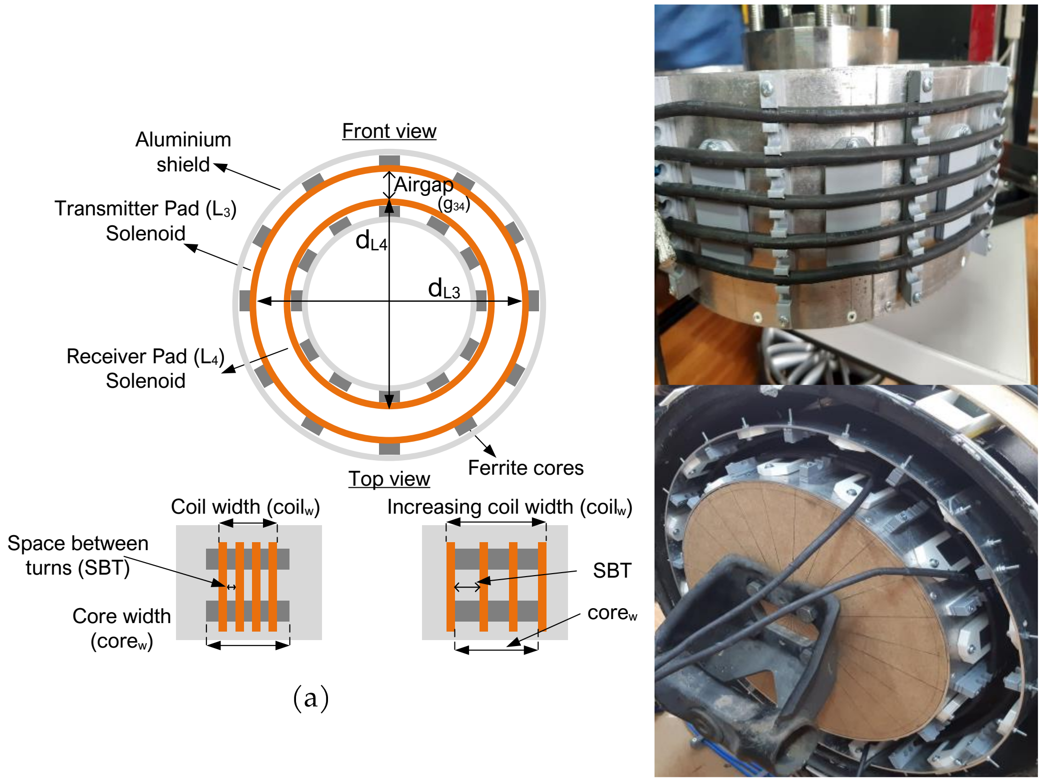


Figure 5.4: (a) IRMC pad geometry and placement, and (b) real implementation of the IRMC.

Fig. 5.5 demonstrates the experimental results of $L_3$, $L_4$, $L_{34}$ and $k_{34}$ for the IRMC structure as function of $coil_w$ and SBT. The structure is implemented to evaluate the impact of the SBT on the IRMC characteristics. The SP coils are built with 5 turns in each pad varying the SBT from 2 to 36 mm, which means a coil width from 42 $mm$ to 169 $mm$ as

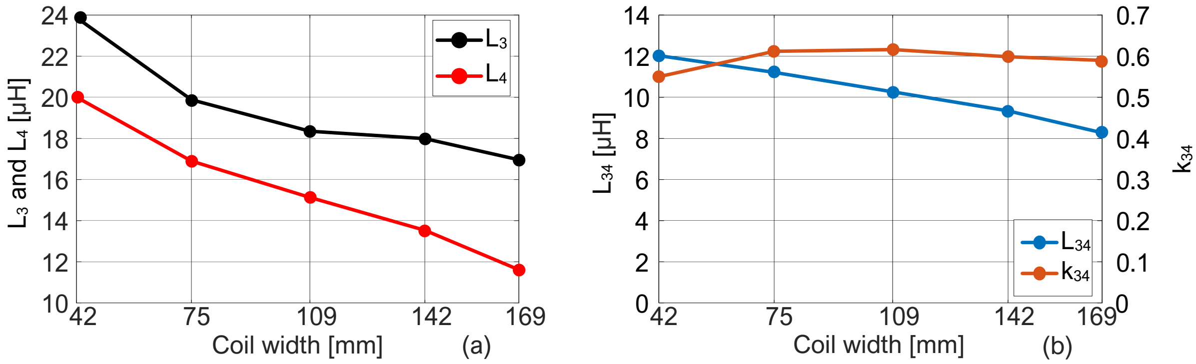


Figure 5.5: Experimental results for IRMC as function of coil width/space between turns for (a) Self-inductances $L_3$ and $L_4$ and, (b) Mutual inductance $L_{34}$ and Coupling factor $k_{34}$.

in Fig. 5.5. No ferrite cores are used and it was used a wood structure to neglect the shielding effect of the aluminium. In Fig. 5.5 (a), the results show a maximum decrease below $42\%$ in both self-inductances $L_3$ and $L_4$ and below $32\%$ for $L_{34}$ in Fig. 5.5 (b). This is caused due to the wider distance between two consecutive turns (SBT increase) which implies higher reluctance values thus resulting in lower self-inductance values. Although a higher value of $coil_w$ provides a better coupling and it tends to stabilize around 0.6 as Fig. 5.5 (b) demonstrates.

Fig. 5.6 shows the experimental results of $L_3$, $L_4$ and $k_{34}$ for the IRMC structure as function of the number of turns and, considering two different core volumes and $g_{34}$. The number of turns of the SP coils varies between 2 and 10 turns. Two core arrangements are used, 43x24x4$mm$ and 86x24x4$mm$, which result in a $core_w$ of 43 $mm$ or 86 $mm$. These arrangements present an increase of ferromagnetic volume by double and as a result, it presents an enhance of magnetic field fluxes and the coupling behaviour between both pads. In addition, two air gaps are considered, $g_{34a}$ and $g_{34b}$ of 15 $mm$ and 10 $mm$, respectively. The results in Fig. 5.6 (a) and Fig. 5.6 (b) show, as expected, an increase of $L_3$, $L_4$ and $k_{34}$ with the increase of the number of turns. The air gap does not affect much the self-inductances, resulting in a maximum variation under $5\ \%$, but increases with the lower air gap. As an example, considering 10 turns and $core_{w1}$, from the blue curve to the pink curve, an increase of $k_{34}$ around $30\ \%$ is obtained. In addition, the increase of core material results in an increase of both self-inductances and coupling factor. In this case, for 10 turns, the increase of $L_3$ and $L_4$ is close to $100\ \%$ and for $k_{34}$ around $75\ \%$ for $g_{34a}$, from blue to red curve.

### 5.2.3 Outer rim magnetic coupler

According to the ORMC, it presents an unique design compared with the conventional IPT systems. This design is the implementation of the receiver pad around the rim, as illustrated in Fig. 5.7. The simplest solution is to maintain the same SP geometry as used for the IRMC pads. However, planar coils are used for conventional IPT systems and for this work, it is used the DDP-BPP geometries for both transmitter and receiver pads. In addition, cylindrical shape of the rim forces the receiver BPP coils to have a bending shape (referred as saddle coils).

Both the rotary movement of the wheels and the shape of the rim add a new challenge to assess the mutual coupling since it originates a new movement between the transmitter and receiver pads of the ORMC, besides the air gap and lateral displacements. Different orientations for the relative position between transmitter and receiver pads are necessary to test DDP-BPP due to ensure the coupling between the pads. Fig. 5.7 and Fig. 5.2 depicts the mentioned issue. The transmitter DDP pad is referred as $L_1$ and it is represented in red and green colour and the receiver pad is referred as $L_2$ and represented by orange colour for both BPP topology, and are spaced by an air gap $g_{12}$, with the specifications in Table 5.1. Twelve ferrite cores (dark grey rectangles) with same characteristics mentioned earlier are equally spaced in the receiver pad perimeter for both structures. Ferrite cores with dimensions 43x24x4$mm$ (length x width x height) are used. Two combinations of core arrangements are used in the analysis. The light grey circles, represent the wheel rim that acts also as an aluminium shields to provide electromagnetic shield and provide a physical mount to the ferrite cores and receiver coils.

The ORMC characteristics for $L_1$, $L_2$ and $k_{12}$ are presented in Fig. 5.8, for DDP-BPP topology. The $L_1$, $L_2$ and $k_{12}$ curves are presented as function of the wheel's rotation angle. This angle $\theta_s$, is defined for the DDP-BPP topology, where a zero angle value corresponds to the perfect alignment between the BPP receiver and the DDP transmitter as depicted in Fig. 5.7. The number of turns for the transmitter DDP coils is 10 turns per coil (10+10), and for the BPP receiver 8 turns per coil (8+8). The $\theta_s$ angle is varied between $-60°$ and $+60°$. Two core arrangements are used, 93x28x16 $mm$ and

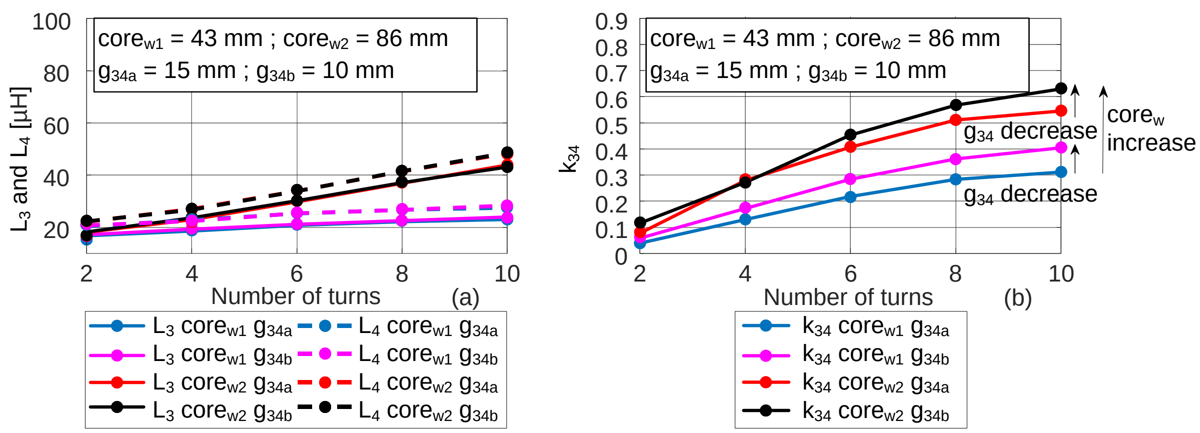


Figure 5.6: Experimental results for IRMC as function of the number of turns, considering different air gaps and, ferrite widths, for (a) Self-inductances $L_3$ and $L_4$ and, (b) Mutual inductance $L_{34}$ and Coupling factor $k_{34}$.

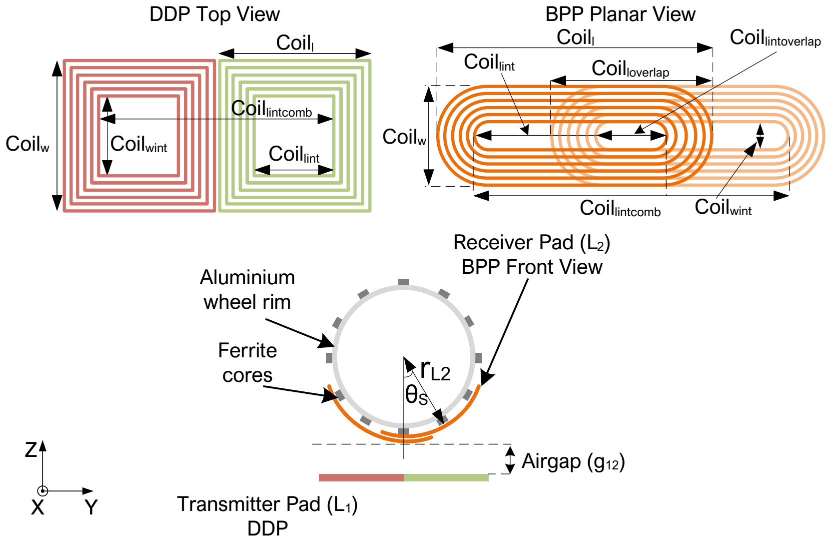


(a)

(b)

Figure 5.7: (a) ORMC pad geometry and placement with DDP-BPP, and (b) real implementation of the ORMC

186x28x16 $mm$ which result in $core_w$ of 93 $mm$ or 186 $mm$. As mentioned for IRMC, these arrangements for ORMC present an increase of ferromagnetic volume by double and as a result, it presents an enhance of magnetic field fluxes and the coupling behaviour between both pads. Two lateral displacements $M_x$, of -50$mm$ and +50 $mm$ are considered.

In Fig. 5.8 (a), the results maintain a constant self-inductance value, independently of different misalignments and wheel's rotation for the transmitter and receiver pads and the core width. For $L_1$, the self-inductance is overlapped for both core widths and presenting a small difference between them and showing independence of all displacements and angles of rotation. On the other hand, the $L_2$ presents overlapped misalignments for each core width. Nonetheless, the coupling factor $k_{12}$ exhibits a different behaviour as in Fig. 5.8 (b). The $k_{12}$ is wheel's rotation ($\theta_s$) dependent, achieving its maximum value for an aligned condition ($M_x = 0\ mm$). According to the wheel's rotation, different $\theta_s$ values are presented and a no-coupling condition can be found,

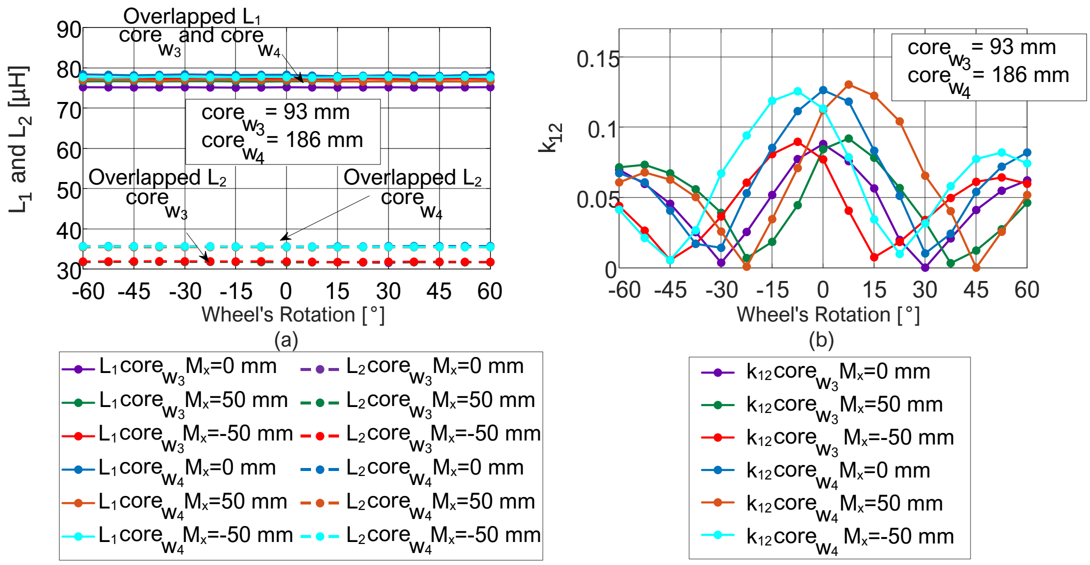


Figure 5.8: Experimental results for ORMC with DDP-BPP topology as function as function of wheel's rotation angles, with different misalignments in $x$ axis and different core widths, for (a) Self-inductances $L_1$ and $L_2$ and, (b) Coupling factor $k_{12}$.

where $k_{12}$ is close to zero, due to coil geometry. This is also shown in SIPT systems under lateral misalignments, when using planar DDP-BPP configuration. Furthermore, lateral displacements (-50 $mm$ and +50 $mm$) do not affect much the maximum achievable coupling, however a shifting effect of the curve is observed, where the maximum coupling is now observed for a $\theta_s$ different from zero. Additionally, and similarly to the previous case, $k_{12}$ decreases for lower $core_w$.

### 5.2.4 Results analysis

The double coupling structure of the inWIPT presents additional challenges and construction requirements regarding placement of the pads and their geometries. This chapter presents an analysis of the different MC considering for the IRMC an SP-SP topology, and a DDP-BPP topology for ORMC. This characterization takes into account the impact of increasing the coil width in the integrated system, the amount and size of ferrite material, as well as the number of turns. Furthermore, misalignments are common in IPT applications and this also need to be evaluated. It is important to identify the ORMC behaviour under different operating conditions, to asses their tolerance to misalignments.

According to the IRMC, the results of on-board SP topologies show an increasing coupling value under the increase of number of turns and core width. Moreover, the self-inductance values are decreased with the increase of coil width due to higher reluctance values, nevertheless, the coupling values increase, initially, and tend to stabilize for a higher value of coil width. On the ORMC, the DDP-BPP configuration can achieve considerable coupling factors, but it is not tolerant to misalignments and presents construction complexity. Nonetheless, only a small portion of the bottom of the wheel is energized, closer to the roadway and meets with the ICNIRP standards regarding to EMI and EMF issues, compared with the SP geometry which will lead to an energized pad over the full perimeter of the wheel.

The characterization of the magnetic parameters of the proposed prototypes contributes to improve the overall system performance, enabling the identification and assessment of the magnetic behaviour of the different integrated pad geometries. The acquired data describes the coupling profile for each geometry pad under specific conditions. These coupling profiles (or mutual inductance profiles) can be used to simulate magnetic behaviour of the IPT system. This allows having the capability to include in the simulation the impact of the different mutual inductances profiles for the electric variables in the overall electric circuit. The experimental results obtained in Fig. 5.8 already show a coupling factor profile as function of the wheel's rotation angle. If further studies are done that account for the motion of the wheel, a complete magnetic coupling analysis is done. This is essential to emulate the EV movement in DIPT operation under different EV displacements and load conditions. A more complexed system model can be built in MATLAB/Simulink to include this behaviour. It needs four inputs, EV speed $[km/h]$, initial position relative to the alignment to the transmitter $[mm]$, variation of air gap under a time interval and the same for the lateral displacements. The coupling profile can be added via a lookup table. With this block, it could be possible to simulate a constant EV speed during a time interval with the coupling variation of the data acquired previously, with different load steps (different SoC values). Through this experimental work, it is possible to assess the real impact of the proposed system under these DIPT conditions by doing a mix of experimental and simulation data.

# 6 Conclusions

IPT technology provides a potential solution for different charging applications, mainly in EVs, enabling charging without any physical connections through magnetic coupling between inductive coils. IPT is available for static charging due to its convenience, safety and interoperability advantages. The inWIPT technology is an alternative variant that facilitates off-board to wheel energy transfer using two MC to minimize the air gap, almost independent of the vehicle. However, this technology presents various challenges in dynamic mode due to the real implementation of the dynamic system on existing infrastructures and, especially, to inherent displacements, misalignments and others conditions leading to different coupling conditions. The S-S-S resonant converter faced issues with high transmitter side currents and voltages, resulting in a no-coupling condition in the first MC. Therefore, new options needed to be assessed to minimize the outcome of these issues and optimize the efficiency of these systems. To address this, this master's work investigated and examined new resonant topologies for DIPT applications, performed simulation and experimental tests to validate the proposed work. Moreover, a study of the behaviour of different magnetic geometries for the experimental prototype was made to assess other configurations (different integrated pad geometries) for the inWIPT DIPT application.

The main work enabled a comparative analysis of three resonant configurations (S-S-S, LCL-S-S and LCC-S-S) for the inWIPT system in dynamic operation with the intent to limit the transmitter side current and voltages to admissible values. As a result, both LCL-S-S and LCC-S-S topologies show a capability for operation in the full range of coupling and load variation in a IPT dynamic applications, serving as a substitutes for the S-S-S topology. Considering the mathematical analysis, both topologies present a CC behaviour in the ORMC transmitter $\overline{I}_1$, a linear behaviour transconductance gain equation $G_{I4Vin}$ and ZPA characteristic and tolerance to high transmitter side current and voltages for, respectively, phase of $Z_{in}$ and module $Z_{in}$. The LCL-S-S topology depends of the values of ORMC self-inductances and they need to be approximately equal to achieve the characteristics, such as ZPA of the $Z_{in}$ phase and LIO of $\overline{I}_1$ and $\overline{I}_4$. On the other hand, the LCC-S-S topology does not present this drawback, therefore, it presents an advantage in comparison of the previous topology. Furthermore, simulations and LCL-S-S resonant converter experimental results validate the aforementioned inherent characteristics of LCL-S-S and LCC-S-S mentioned in theoretical results. In simulations, the S-S-S topology presents a higher value of output batteries power $P_{bat}$ under ORMC mutual inductance $L_{12}$ and battery resistance $R_{bat}$, although it is not a viable solution for DIPT due to main issue of high circulating currents in no-coupling mode. Between LCL-S-S and LCC-S-S, the LCC-S-S presents the higher values of output batteries power $P_{bat}$ for the same conditions, presenting an advantage in comparison with the LCL-S-S.

Additional studies were conducted to examine the magnetic behaviour of both ORMC and IRMC. For the ORMC, a DDP transmitter pad with BPP in the wheel and for the IRMC, a second MC constructed with two SP pads. Their tolerance to displacements, wheel's rotation, core volume, characterization of self/mutual inductance and coupling factor was done under various conditions. This characterization demonstrated a possible combination of coils geometry to be applied in the dynamic inWIPT. The results of on-board SP topology show a decreasing of self-inductances and an increasing coupling value under different conditions of construction and magnetic view. The selected DDP-BPP configuration is a feasible solution for a dynamic inWIPT system. However, it is less tolerant to misalignments (when compared to other possible geometries, such as DDP-SP) and presents some construction complexity.

This work presents an electrical, mathematical and simulation studies of the system under analysis in order to enhance its capabilities in dynamic mode. It also presents relevant experimental work regarding different possible in-wheel pad geometries and their magnetic behaviour. The contributions made in this project can create new research opportunities, such as:

- Study of new resonant configurations for inWIPT system, such as new topologies of three-coil system to improve its capabilities and meeting with the given set of specifications and constraints.
- Analysis of new geometries pads or new factors involving the actual system under different conditions of construction and magnetic view to better understand the behaviour in different scenarios of dynamic mode.
- Simulation of a MATLAB/Simulink DIPT system model, introducing a coupling variation in order to emulate its behaviour under different EV displacements, EV speed, initial positions and other conditions.
- Development of a design methodology to obtain the MC parameters of the converter in terms of mutual inductances and coupling factors with a set of electrical specifications.

This master's work and the contributions made for two published articles were done as part of the research conducted during a scholarship supported by Instituto de Telecomunicações under the framework of Project inWheel Inductive Power Charging for Sustainable Mobility with reference 2022.06192.PTDC. The two mentioned publications are entitled "Double Coupling in-Wheel Dynamic IPT for EV Charging", at the *Institute of Electrical and Electronics Engineers* (IEEE) *Energy Conversion Congress & Expo*

(ECCE) 2023 conference and "Characterization of Multiple Integrated Pad Geometries for in-Wheel EV IPT Applications", at the IEEE *Vehicle Power and Propulsion* (VPPC) 2023.

# References


[1] D. Wang, J. Zhang, S. Cui, Z. Bie, K. Song, C. Zhu, and M. I. Matveevich, "Modern advances in magnetic materials of wireless power transfer systems: A review and new perspectives," *Nanomaterials*, vol. 12, no. 20, 2022. [Online]. Available: https://www.mdpi.com/2079-4991/12/20/3662

[2] X. Wei, Z. Wang, and H. Dai, "A critical review of wireless power transfer via strongly coupled magnetic resonances," *Energies*, vol. 7, no. 7, pp. 4316–4341, 2014. [Online]. Available: https://www.mdpi.com/1996-1073/7/7/4316

[3] J. Van Mulders, D. Delabie, C. Lecluyse, C. Buyle, G. Callebaut, L. Van der Perre, and L. De Strycker, "Wireless power transfer: Systems, circuits, standards, and use cases," *Sensors*, vol. 22, no. 15, 2022. [Online]. Available: https://www.mdpi.com/1424-8220/22/15/5573

[4] K. Detka and K. Górecki, "Wireless power transfer;a review," *Energies*, vol. 15, no. 19, 2022. [Online]. Available: https://www.mdpi.com/1996-1073/15/19/7236

[5] M. I. T. News. [Online]. Available: https://news.mit.edu/2007/wireless-0607

[6] E. G. Marques, A. M. dos Santos Mendes, M. M. S. D. Perdigão, and V. S. Costa, "Inductive power transfer: Past, current, and future research," in *The Dynamics of Vehicles - Basics, Simulation and Autonomous Systems*, D. H. T. Arat, Ed. Rijeka: IntechOpen, 2022, ch. 5. [Online]. Available: https://doi.org/10.5772/intechopen.108484

[7] V. Shevchenko, O. Husev, R. Strzelecki, B. Pakhaliuk, N. Poliakov, and N. Strzelecka, "Compensation topologies in ipt systems: Standards, requirements, classification, analysis, comparison and application," *IEEE Access*, vol. 7, pp. 120 559–120 580, 2019.

[8] C. Zhu, K. Liu, C. Yu, R. Ma, and H. Cheng, "Simulation and experimental analysis on wireless energy transfer based on magnetic resonances," in *2008 IEEE Vehicle Power and Propulsion Conference*, 2008, pp. 1–4.

[9] Wibotic. Wibotic autonomous charging. [Online]. Available: https://www.wibotic.com/

[10] Witricity. Automotive solutions. [Online]. Available: https://witricity.com/

[11] Warstila. Wärtsilä wireless vessel charging system. [Online]. Available: https://www.wartsila.com/marine/products/ship-electrification-solutions/

shore-power/charging

[12] Y. Xu, "Heating system based on wireless charging qi standards," Apr. 2014, cN Patent 203,554,077 U.

[13] O. Lucia, J. Acero, C. Carretero, and J. M. Burdio, "Induction heating appliances: Toward more flexible cooking surfaces," *IEEE Industrial Electronics Magazine*, vol. 7, no. 3, pp. 35–47, 2013.

[14] A. Namin, E. Chaidee, S. Tanang, K. Chaikam, and P. Jansuya, "Mutual impedance adaptation for maximum power point tracking on led tv wireless power transfer vary with distance," in *2018 15th International Conference on Electrical Engineering/Electronics, Computer, Telecommunications and Information Technology (ECTI-CON)*, 2018, pp. 501–504.

[15] G. A. Covic and J. T. Boys, "Modern trends in inductive power transfer for transportation applications," *IEEE Journal of Emerging and Selected Topics in Power Electronics*, vol. 1, no. 1, pp. 28–41, 2013.

[16] C. Qiu, K. T. Chau, T. W. Ching, and C. Liu, "Overview of wireless charging technologies for electric vehicles," *Journal of Asian Electric Vehicles*, vol. 12, no. 1, pp. 1679–1685, 2014.

[17] G. Guidi, J. A. Suul, F. Jenset, and I. Sorfonn, "Wireless charging for ships: High-power inductive charging for battery electric and plug-in hybrid vessels," *IEEE Electrification Magazine*, vol. 5, no. 3, pp. 22–32, 2017.

[18] S. Wu, C. Cai, X. Liu, W. Chai, and S. Yang, "Compact and free-positioning omnidirectional wireless power transfer system for unmanned aerial vehicle charging applications," *IEEE Transactions on Power Electronics*, vol. 37, no. 8, pp. 8790–8794, 2022.

[19] X. Li, G. Zhu, M. Pang, K. Xiang, J. Lu, and W. Yue, "Analysis and design of wireless power transfer system for robot joints," in *2022 IEEE 5th International Electrical and Energy Conference (CIEEC)*, 2022, pp. 1826–1830.

[20] X. Lu, P. Wang, D. Niyato, D. I. Kim, and Z. Han, "Wireless charging technologies: Fundamentals, standards, and network applications," *IEEE Communications Surveys and Tutorials*, vol. 18, no. 2, pp. 1413–1452, 2016.

[21] H. Kim, J. Ahn, J. Rhee, and S. Ahn, "Application of wireless power transfer technology to implantable medical devices," in *2022 IEEE MTT-S International Microwave Biomedical Conference (IMBioC)*, 2022, pp. 299–301.

[22] V. B. Gore and D. H. Gawali, "Wireless power transfer technology for medical applications," in *2016 Conference on Advances in Signal Processing (CASP)*, 2016, pp. 455–460.

[23] G. Yilmaz and C. Dehollain, "An efficient wireless power link for implanted biomedical devices via resonant inductive coupling," in *2012 IEEE Radio and Wireless Symposium*, 2012, pp. 235–238.

[24] qiwireless, "Qiwireless.com is the no.1 online source for wireless charging technologies information," 2022.

[25] C. EVs. Electreon to deploy public wireless ev charging road in germany. [Online]. Available: https://chargedevs.com/newswire/electreon-to-deploy-public-wireless-ev-charging-road-in-germany/

[26] Electreon. Wirelessly charge electric vehicles | electreon. [Online]. Available: https://electreon.com/

[27] V. S. Costa, E. Marques, A. P. Mendes, M. S. Perdigao, and A. M. S. Mendes, "Magnetic couplers for dynamic ipt systems," in *2019 IEEE Vehicle Power and Propulsion Conference (VPPC)*, 2019, pp. 1–6.

[28] A. A. S. Mohamed, A. A. Shaier, H. Metwally, and S. I. Selem, "An overview of dynamic inductive charging for electric vehicles," *Energies*, vol. 15, no. 15, 2022. [Online]. Available: https://www.mdpi.com/1996-1073/15/15/5613

[29] E. G. Marques and A. M. S. Mendes, "Optimization of transmitter magnetic structures for roadway applications," in *2017 IEEE Applied Power Electronics Conference and Exposition (APEC)*, 2017, pp. 959–965.

[30] C. Panchal, S. Stegen, and J. Lu, "Review of static and dynamic wireless electric vehicle charging system," *Engineering Science and Technology, an International Journal*, vol. 21, no. 5, pp. 922–937, 2018. [Online]. Available: https://www.sciencedirect.com/science/article/pii/S221509861830154X

[31] E. G. Marques, V. S. Costa, M. Torres, B. Rios, A. Mendes, and M. S. Perdigão, "Double coupling ipt systems for ev charging applications," in *2021 IEEE Vehicle Power and Propulsion Conference (VPPC)*, 2021, pp. 1–6.

[32] S. K. Chawrasia, C. Kumar Chanda, and S. Banerjee, "Design and analysis of in-wheel motor for an electric vehicle," in *2020 IEEE Calcutta Conference (CALCON)*, 2020, pp. 351–355.

[33] E. F. Aloeyi, N. Ali, and Q. Wang, "A review of in-wheel motors for electric vehicle propulsion," in *2022 IEEE Transportation Electrification Conference and Expo, Asia-Pacific (ITEC Asia-Pacific)*, 2022, pp. 1–6.

[34] M. Sato, G. Yamamoto, D. Gunji, T. Imura, and H. Fujimoto, "Development of wireless in-wheel motor using magnetic resonance coupling," *IEEE Transactions on Power Electronics*, vol. 31, no. 7, pp. 5270–5278, 2016.

[35] O. Shimizu, T. Imura, H. Fujimoto, D. Gunji, K. Akutagawa, and G. Guidi, "Mutual inductance modeling of in-wheel arc-shaped coil for in-motion wpt," in *2019*

*IEEE Wireless Power Transfer Conference (WPTC)*, 2019, pp. 624–628.

[36] V. Z. Barsari, D. J. Thrimawithana, and G. A. Covic, "An inductive coupler array for in-motion wireless charging of electric vehicles," *IEEE Transactions on Power Electronics*, vol. 36, no. 9, pp. 9854–9863, 2021.

[37] W. Li, H. Zhao, J. Deng, S. Li, and C. C. Mi, "Comparison study on ss and double-sided lcc compensation topologies for ev/phev wireless chargers," *IEEE Transactions on Vehicular Technology*, vol. 65, no. 6, pp. 4429–4439, 2016.

[38] P. Fonte, "Apontamentos de eletromagnetismo," Instituto Superior de Engenharia de Coimbra, Coimbra, Tech. Rep., 2013.

[39] E. G. Marques, *Mitigate the Effect of Coupling Factor Variations in Inductive Power Transfer Systems*, 2023.

[40] J. Zhang, X. Yuan, C. Wang, and Y. He, "Comparative analysis of two-coil and three-coil structures for wireless power transfer," *IEEE Transactions on Power Electronics*, vol. 32, no. 1, pp. 341–352, 2017.

[41] D.-W. Seo, "Comparative analysis of two- and three-coil wpt systems based on transmission efficiency," *IEEE Access*, vol. 7, pp. 151 962–151 970, 2019.

[42] L. Chen, G. R. Nagendra, J. T. Boys, and G. A. Covic, "Double-coupled systems for ipt roadway applications," *IEEE Journal of Emerging and Selected Topics in Power Electronics*, vol. 3, no. 1, pp. 37–49, 2015.

[43] C. Cheng, F. Lu, Z. Zhou, W. Li, C. Zhu, H. Zhang, Z. Deng, X. Chen, and C. C. Mi, "Load-independent wireless power transfer system for multiple loads over a long distance," *IEEE Transactions on Power Electronics*, vol. 34, no. 9, pp. 9279–9288, 2019.

[44] D. M. Niculae, M. Stanculescu, S. Deleanu, M. Iordache, and L. Bobaru, "Wireless power transfer systems optimization using multiple magnetic couplings," *Electronics*, vol. 10, no. 20, 2021. [Online]. Available: https://www.mdpi.com/2079-9292/10/20/2463

[45] E. G. Marques, V. S. Costa, M. S. Perdigão, and A. M. S. Mendes, "Double coupling in-wheel ipt system for electric vehicles," *IEEE Transactions on Vehicular Technology*, vol. 72, no. 10, pp. 12 757–12 769, 2023.

[46] Y. limited. [Online]. Available: https://www.yasa.com/

[47] E. G. Marques, A. M. S. Mendes, M. S. Perdigão, and V. S. Costa, "Design methodology of a three coil ipt system with parameters identification for evs," *IEEE Transactions on Vehicular Technology*, vol. 70, no. 8, pp. 7509–7521, 2021.

[48] D. Xin, L. Weiyi, L. Yanling, S. Yugang, T. Chunsen, W. Zhihui, and S. Yue, "Improved lcl resonant network for inductive power transfer system," in *2015 IEEE*

*PELS Workshop on Emerging Technologies: Wireless Power (2015 WoW)*, 2015, pp. 1–5.

[49] Z. Pantic, S. Bai, and S. M. Lukic, "Zcs $lcc$-compensated resonant inverter for inductive-power-transfer application," *IEEE Transactions on Industrial Electronics*, vol. 58, no. 8, pp. 3500–3510, 2011.

[50] M. Feliziani, T. Campi, S. Cruciani, F. Maradei, U. Grasselli, M. Macellari, and L. Schirone, "Robust lcc compensation in wireless power transfer with variable coupling factor due to coil misalignment," in *2015 IEEE 15th International Conference on Environment and Electrical Engineering (EEEIC)*, 2015, pp. 1181–1186.

[51] V. S. Costa, E. G. Marques, M. Torres, A. M. S. Mendes, and M. S. Perdigão, "Double coupling in-wheel dynamic ipt for ev charging," in *2023 IEEE Energy Conversion Congress and Exposition (ECCE)*, 2023, pp. 1725–1730.

[52] Y. J. Hwang and J. Y. Jang, "Design and analysis of a novel magnetic coupler of an in-wheel wireless power transfer system for electric vehicles," *Energies*, vol. 13, no. 2, 2020. [Online]. Available: https://www.mdpi.com/1996-1073/13/2/332

[53] J. Zhou, P. Yao, Y. Chen, K. Guo, S. Hu, and H. Sun, "Design considerations for a self-latching coupling structure of inductive power transfer for autonomous underwater vehicle," *IEEE Transactions on Industry Applications*, vol. 57, no. 1, pp. 580–587, 2021.

[54] M. A. Houran, X. Yang, and W. Chen, "Two-degree-of-freedom wpt system using cylindrical-joint structure for applications with movable parts," *IEEE Transactions on Circuits and Systems II: Express Briefs*, vol. 68, no. 1, pp. 366–370, 2021.

[55] Z. Yan, B. Song, Y. Zhang, K. Zhang, Z. Mao, and Y. Hu, "A rotation-free wireless power transfer system with stable output power and efficiency for autonomous underwater vehicles," *IEEE Transactions on Power Electronics*, vol. 34, no. 5, pp. 4005–4008, 2019.

[56] T. Kan, Y. Zhang, Z. Yan, P. P. Mercier, and C. C. Mi, "A rotation-resilient wireless charging system for lightweight autonomous underwater vehicles," *IEEE Transactions on Vehicular Technology*, vol. 67, no. 8, pp. 6935–6942, 2018.

[57] A. Abdolkhani, A. P. Hu, and N.-K. C. Nair, "A double stator through-hole type contactless slipring for rotary wireless power transfer applications," *IEEE Transactions on Energy Conversion*, vol. 29, no. 2, pp. 426–434, 2014.

[58] R. Trevisan and A. Costanzo, "A 1-kw contactless energy transfer system based on a rotary transformer for sealing rollers," *IEEE Transactions on Industrial Electronics*, vol. 61, no. 11, pp. 6337–6345, 2014.

[59] K. Song, B. Ma, G. Yang, J. Jiang, R. Wei, H. Zhang, and C. Zhu, "A rotation-lightweight wireless power transfer system for solar wing driving," *IEEE Trans-*

*actions on Power Electronics*, vol. 34, no. 9, pp. 8816–8830, 2019.

[60] E. G. Marques, *Transferência de Energia sem contactos para cargas de Baterias de Veículos Eléctricos*, 2014.

# Appendix

# Appendix A - Analysis of the proposed electrical circuit with S-S-S configuration

## 1. Generic equations

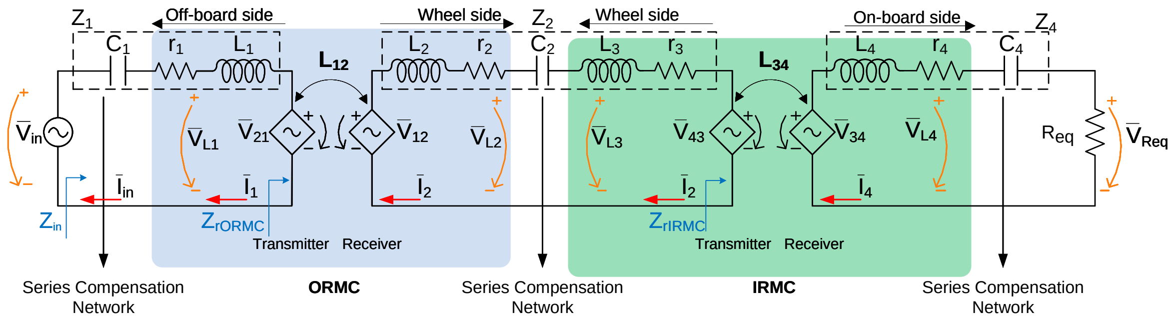


Figure 6.1: Equivalent circuit model of a double coupling inWIPT for S-S-S resonant compensation.

Applying Kirchhoff's laws to analyze the equivalent circuit of the S-S-S configuration, the following equations are obtained:

$$\overline{V}_{in} = \overline{V}_{L_1} + \overline{V}_{C_1} + \overline{V}_{r_1} + \overline{V}_{21}, \tag{6.1}$$

$$\overline{V}_{12} = \overline{V}_{L_2} + \overline{V}_{C_2} + \overline{V}_{r_2} + \overline{V}_{L_3} + \overline{V}_{r_3} + \overline{V}_{43}, \tag{6.2}$$

$$\overline{V}_{34} = \overline{V}_{L_4} + \overline{V}_{C_4} + \overline{V}_{r_4} + \overline{V}_{R_{eq}}, \tag{6.3}$$

$$\Leftrightarrow \text{Applying Laplace transforms } (s = j.\omega) \Leftrightarrow$$

$$\overline{V}_{in}(s) = s.L_1.\overline{I}_{in}(s) + \frac{1}{s.C_1}\overline{I}_{in}(s) + r_1.\overline{I}_{in}(s) - s.L_{12}.\overline{I}_2(s), \tag{6.1}$$

$$s.L_{12}.\overline{I}_{in}(s) = s.L_2.\overline{I}_2(s) + r_2.\overline{I}_{2_{(s)}} + \frac{1}{s.C_2}\overline{I}_2(s) + s.L_3.\overline{I}_2(s) + r_3.\overline{I}_2(s) - s.L_{34}.\overline{I}_4(s), \tag{6.2}$$

$$s.L_{34}.\overline{I}_2(s) = s.L_4.\overline{I}_4(s) + \frac{1}{s.C_4}\overline{I}_4(s) + r_4.\overline{I}_4(s) + R_{eq}.\overline{I}_4(s), \tag{6.3}$$

$$\Leftrightarrow \text{Assuming } \overline{I}_4(s) = \overline{I}_2(s)\frac{s.L_{34}}{(Z_4+R_{eq})} \Leftrightarrow$$

$$s.L_{12}.\overline{I}_{in}(s) = \overline{I}_2(s)\left(s.L_2 + r_2 + \frac{1}{s.C_2} + s.L_3 + r_3\right) - s.L_{34}\left(\overline{I}_2(s)\frac{s.L_{34}}{(Z_4 + R_{eq})}\right), \Leftrightarrow$$

$$s.L_{12}.\overline{I}_{in}(s) = \overline{I}_2(s)\left(s.L_2 + s.L_3 + r_2 + r_3 + \frac{1}{s.C_2} + s.L_3 + r_3 + \frac{1}{s.C_2} - \frac{s^2.L_{34}^2}{(Z_4 + R_{eq})}\right), \Leftrightarrow \tag{6.2}$$

$$\overline{I}_2(s) = \overline{I}_{in}(s)\frac{s.L_{12}}{(Z_2 + Z_{r_{IRMC}})},$$

$$\Leftrightarrow \text{Assuming } \overline{I}_2(s) = \overline{I}_{in}(s)\tfrac{s.L_{12}}{(Z_2+Z_{r_{IRMC}})} \Leftrightarrow$$

$$\overline{V}_{in}(s) = s.L_1.\overline{I}_{in}(s) + \frac{1}{s.C_1}\overline{I}_{in}(s) + s.r_1.\overline{I}_{in}(s), \Leftrightarrow$$

$$\overline{V}_{in}(s) = \overline{I}_{in}(s)(Z_1 + Z_{r_{ORMC}}), \tag{6.1}$$

$$\Leftrightarrow \text{Assuming } (s = j.\omega) \text{ to (6.1), (6.2) and (6.3)} \Leftrightarrow$$

$$\overline{V}_{in} = r_1.\overline{I}_{in} + j.\omega((L_1 - 1/(\omega^2.C_1))\overline{I}_{in} - L_{12}.\overline{I}_2), \tag{6.1}$$

$$0 = (r_2 + r_3).\overline{I}_2 + j.\omega((L_2 + L_3 - 1/(\omega^2.C_2))\overline{I}_2 - L_{12}.\overline{I}_1 - L_{34}.\overline{I}_4), \tag{6.2}$$

$$0 = (R_{eq} + r_4).\overline{I}_4 + j.\omega((L_4 - 1/(\omega^2.C_4))\overline{I}_4 - L_{34}.\overline{I}_2), \tag{6.3}$$

## 2. Generic equations for currents and voltages

Through (6.1), (6.2) and (6.3), the equations for the currents in the equivalent electrical circuit were defined to better define the S-S-S configuration. The equations for the currents are given by

$$\overline{I}_{in}(s) = \frac{\overline{V}_{in}(s)}{Z_{in}} = \frac{\overline{V}_{in}(s)}{(Z_1 + Z_{r_{ORMC}})}, \tag{6.4}$$

$$\overline{I}_2(s) = \overline{I}_{in}(s)\frac{s.L_{12}}{(Z_2 + Z_{r_{IRMC}})}, \tag{6.5}$$

$$\overline{I}_4(s) = \overline{I}_2(s)\frac{s.L_{34}}{(Z_4 + R_{eq})}, \tag{6.6}$$

$$\Leftrightarrow \text{Applying Laplace transforms } (s = j.\omega) \Leftrightarrow$$

$$\overline{I}_{in} = \frac{\overline{V}_{in}}{Z_{in}} = \frac{\overline{V}_{in}}{(Z_1 + Z_{r_{ORMC}})}, \tag{6.4}$$

$$\overline{I}_2 = \overline{I}_{in}\frac{j.\omega.L_{12}}{(Z_2 + Z_{r_{IRMC}})}, \tag{6.5}$$

$$\overline{I}_4 = \overline{I}_2\frac{j.\omega.L_{34}}{(Z_4 + R_{eq})}, \tag{6.6}$$

The induced voltages across the coils are expressed by

$$|\overline{V}_{L_1}(s)| = |\overline{I}_1(s).(r_1 + s.L_1 + Z_{r_{ORMC}})| \tag{6.7}$$

$$|\overline{V}_{L_2}(s)| = |\overline{I}_2(s).(r_2 + s.L_3 + 1/(s.C_2) + Z_{r_{IRMC}})| \tag{6.8}$$

$$|\overline{V}_{L_3}(s)| = |\overline{I}_2(s).(r_3 + s.L_3 + Z_{r_{IRMC}})| \tag{6.9}$$

$$|\overline{V}_{L_4}(s)| = |\overline{I}_4(s).(R_{eq} + 1/(s.C_4))| \tag{6.10}$$

$$\Leftrightarrow \text{Applying Laplace transforms } (s = j.\omega) \Leftrightarrow$$

$$|\overline{V}_{L_1}| = |\overline{I}_1.(r_1 + j.\omega.L_1 + Z_{r_{ORMC}})| \tag{6.7}$$

$$|\overline{V}_{L_2}| = |\overline{I}_2.(r_2 + j.\omega.L_3 + 1/(j.\omega.C_2) + Z_{r_{IRMC}})| \tag{6.8}$$

$$|\overline{V}_{L_3}| = |\overline{I}_2.(r_3 + j.\omega.L_3 + Z_{r_{IRMC}})| \tag{6.9}$$

$$|\overline{V}_{L_4}| = |\overline{I}_4.(R_{eq} + 1/(j.\omega.C_4))| \tag{6.10}$$

## 3. Equations for capacitors

The equations for capacitors allow us to determine the resonant frequency and control the energy transfer between the MC coils. Fig. 6.2 illustrates the different meshes where the following capacitors are placed.

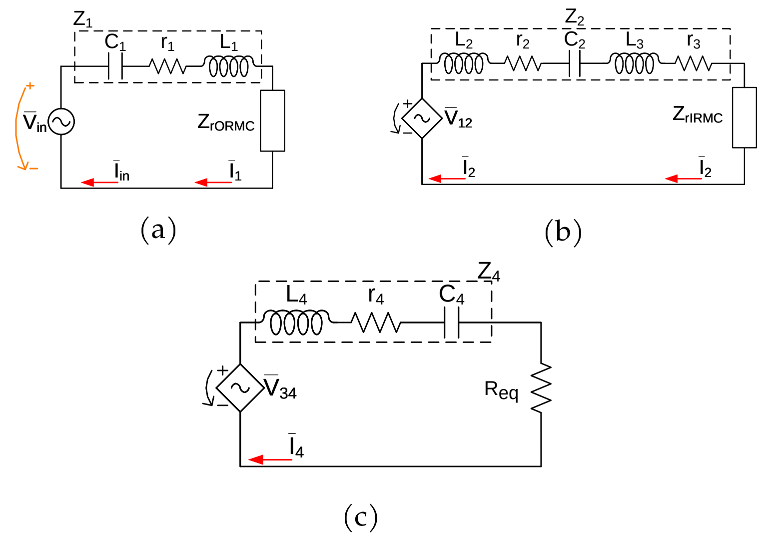


Figure 6.2: (a) $C_1$ mesh, (b) $C_2$ mesh and (c) $C_4$ mesh

According to the Fig. 6.2, the Kirchhoff's equations of the different meshes are

$$\overline{V}_{in}(s) = \left(s.L_1 + \frac{1}{s.C_1} + r_1\right)\overline{I}_{in}(s) + Z_{r_{ORMC}}.\overline{I}_{in}(s), \tag{6.11}$$

$$\overline{V}_{12}(s) = \left(s.L_2 + s.L_3 + \frac{1}{s.C_2} + r_2 + r_3\right)\overline{I}_2(s) + Z_{r_{IRMC}}.\overline{I}_2(s), \tag{6.12}$$

$$\overline{V}_{34}(s) = \left(s.L_4 + \frac{1}{s.C_4} + r_4\right)\overline{I}_4(s) + R_{eq}.\overline{I}_4(s), \tag{6.13}$$

$\Leftrightarrow$ Applying Laplace transforms $(s = j.\omega)$ and $(r_1 = r_2 = r_3 = r_4 = 0\ \Omega)$ $\Leftrightarrow$

$$\overline{V}_{in} = \left(j.\omega.L_1 + \frac{1}{j.\omega.C_1}\right)\overline{I}_{in} + Z_{r_{ORMC}}.\overline{I}_{in}, \tag{6.11}$$

$$\overline{V}_{12} = \left(j.\omega.L_2 + j.\omega.L_3 + \frac{1}{j.\omega.C_2}\right)\overline{I}_2 + Z_{r_{IRMC}}.\overline{I}_2, \tag{6.12}$$

$$\overline{V}_{34} = \left(j.\omega.L_4 + \frac{1}{j.\omega.C_4}\right)\overline{I}_4 + R_{eq}.\overline{I}_4, \tag{6.13}$$

From (6.11), (6.12) and (6.13) and assuming the imaginary part equal to 0, the following equations are expressed by

$$\omega_1.L_1 - \frac{1}{\omega_1.C_1} = 0 \tag{6.14}$$

$$\omega_2(L_2 + L_3) - \frac{1}{\omega_2.C_2} = 0 \tag{6.15}$$

$$\omega_4.L_4 - \frac{1}{\omega_4.C_4} = 0 \tag{6.16}$$

$\Leftrightarrow$ Assuming [31] $(\omega_1 = \omega_2 = \omega_4 = \omega)$ $\Leftrightarrow$

$$C_1 = 1/(\omega^2.L_1), \tag{6.14}$$

$$C_2 = 1/(\omega^2.(L_2 + L_3)), \tag{6.15}$$

$$C_4 = 1/(\omega^2.L_4). \tag{6.16}$$

## 4. Equations for impedances

The equations for impedances contribute to determining the equations for the voltage and transconductance gains, where these equations allow the identification of the loading profiles of each configuration. The equations for the impedances are given by

$$Z_1(s) = s.L_1 + r_1 + \frac{1}{s.C_1}, \tag{6.17}$$

$$Z_2(s) = s.L_2 + s.L_3 + r_2 + r_3 + \frac{1}{s.C_2}, \tag{6.18}$$

$$Z_4(s) = s.L_4 + r_4 + \frac{1}{s.C_4}, \tag{6.19}$$

$\Leftrightarrow$ Applying Laplace transforms $(s = j.\omega)$ and $\omega_x = \frac{1}{\sqrt{L_x.C_x}}$ $\Leftrightarrow$

$$Z_1 = r_1 + j.\omega(L_1 - 1/(\omega^2.C_1)), \tag{6.17}$$

$$Z_2 = (r_2 + r_3) + j.\omega.(L_2 + L_3 - 1/(\omega^2.C_2)), \tag{6.18}$$

$$Z_4 = r_4 + j.\omega(L_4 - 1/(\omega^2.C_4)), \tag{6.19}$$

## 5. Equations for reflected impedances under resonance and ideal conditions

The equations for the reflected impedances contribute to determining the equations for the voltage and transconductance gains, where these equations allow the identification of the loading profiles of each configuration. The equations for the reflected impedances are given by

$$Z_{r_{IRMC}}(s) = -\frac{s^2.L_{34}^2}{(Z_4 + R_{eq})}, \tag{6.20}$$

$$Z_{r_{ORMC}}(s) = -\frac{s^2.L_{12}^2}{(Z_2 + Z_{r_{IRMC}}(s))}, \tag{6.21}$$

$\Leftrightarrow$ Applying Laplace transforms ($s = j.\omega$) and
considering the conditions ($r_1 = r_2 = r_3 = r_4 = 0\ \Omega$) e ($\omega = \omega_x$) $\Leftrightarrow$

$$Z_{r_{IRMC}} = \frac{\omega^2.L_{34}^2}{R_{eq}}, \tag{6.20}$$

$$Z_{r_{ORMC}} = \frac{\frac{\omega^2.L_{12}^2}{1}}{\frac{\omega^2.L_{34}^2}{R_{eq}}} = \frac{\omega^2.L_{12}^2(Z_4 + R_{eq})}{(Z_2(Z_4 + R_{eq}) + \omega^2.L_{34}^2)} = \frac{L_{12}^2.R_{eq}}{L_{34}^2}, \tag{6.21}$$

## 6. Input impedance

The input impedance $Z_{in}$ is the equivalent impedance seen by the power supply and it is the aggregated of the reflected impedance from IRMC and the receiver side ORMC onto the transmitter side ORMC and the equivalent impedances of the transmitter side ORMC and input side. The equation of $Z_{in}$ is shown by

$$Z_{in} = Z_1 + Z_{r_{ORMC}}. \tag{6.22}$$

If the system losses are neglected ($r_1 = r_2 = r_3 = r_4 = 0\ \Omega$) and the system is under resonance ($\omega = \omega_x$), using MATLAB simplify function, (6.22) is defined by

$$Z_{in} = \frac{R_{eq}.L_{12}^2}{L_{34}^2}. \tag{6.23}$$

Assuming the mentioned conditions, (6.23) is purely resistive and depends on the ratio of $L_{34}^2/L_{12}^2$.

## 7. Voltage and transconductance gain equations

The equations of voltage gains and transconductance where these equations allow identifying the loading profiles of each configuration. Considering the current equations, it is possible to determine the equations for the gains that are given by

$$G_{vReqvin} = \frac{\overline{V}_{R_{eq}}}{\overline{V}_{in}}, \tag{6.24}$$

$$G_{i4vin} = \frac{\overline{I}_4}{\overline{V}_{in}}, \tag{6.25}$$

$$G_{i2vin} = \frac{\overline{I}_2}{\overline{V}_{in}}, \tag{6.26}$$

$$G_{i1vin} = \frac{\overline{I}_1}{\overline{V}_{in}}, \tag{6.27}$$

⇔ Applying the equalities between the equations of the currents and highlighting ⇔

$$G_{vReqvin}(s) = \frac{R_{eq}(s.L_{12})(s.L_{34})}{(Z_4 + R_{eq})(Z_2 + Z_{r_{IRMC}})(Z_1 + Z_{r_{ORMC}})}, \tag{6.24}$$

$$G_{i4vin}(s) = \frac{(s.L_{12})(s.L_{34})}{(Z_4 + R_{eq})(Z_2 + Z_{r_{IRMC}})(Z_1 + Z_{r_{ORMC}})}, \tag{6.25}$$

$$G_{i2vin}(s) = \frac{(s.L_{12})}{(Z_2 + Z_{r_{IRMC}})(Z_1 + Z_{r_{ORMC}})}, \tag{6.26}$$

$$G_{i1vin}(s) = \frac{1}{(Z_1 + Z_{r_{ORMC}})}, \tag{6.27}$$

⇔ Applying Laplace transforms $(s = j.\omega)$ ⇔

$$G_{vReqvin} = -\frac{\omega^2.R_{eq}.L_{12}.L_{34}}{(R_{eq} + Z_4)(Z_2 + Z_{r_{IRMC}})(Z_1 + Z_{r_{ORMC}})}. \tag{6.24}$$

$$G_{i4vin} = -\frac{\omega^2.L_{12}.L_{34}}{(R_{eq} + Z_4)(Z_2 + Z_{r_{IRMC}})(Z_1 + Z_{r_{ORMC}})}, \tag{6.25}$$

$$G_{i2vin} = \frac{j.\omega.L_{12}}{(Z_2 + Z_{r_{IRMC}})(Z_1 + Z_{r_{ORMC}})}, \tag{6.26}$$

$$G_{i1vin} = \frac{1}{(Z_1 + Z_{r_{ORMC}})}, \tag{6.27}$$

⇔ If the system is under resonance $(\omega = \omega_x)$ and $(r_1 = r_2 = r_3 = r_4 = 0\ \Omega)$,
using MATLAB simplify function ⇔

$$G_{vReqvin} = -\frac{L_{34}}{L_{12}}, \tag{6.24}$$

$$G_{i4vin} = -\frac{L_{34}}{R_{eq}.L_{12}}, \tag{6.25}$$

$$G_{i2vin} = \frac{j}{\omega.L_{12}}, \tag{6.26}$$

$$G_{i1vin} = \frac{L_{34}^2}{R_{eq}.L_{12}^2}, \tag{6.27}$$

# Appendix B - Analysis of the proposed electrical circuit with LCL-S-S configuration

## 1. Generic equations

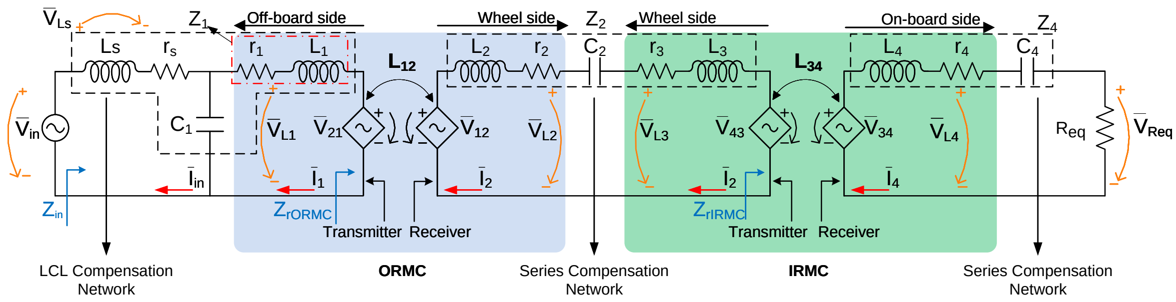


Figure 6.3: Equivalent circuit model of a double coupling inWIPT for LCL-S-S resonant compensation.

Applying Kirchhoff's laws to analyze the equivalent circuit of the LCL-S-S configuration, the following equations are obtained:

$$\overline{V}_{in} = \overline{V}_{L_s} + \overline{V}_{C_1} + \overline{V}_{r_s}, \tag{6.28}$$

$$\overline{V}_{C_1} = \overline{V}_{L_1} + \overline{V}_{r_1} + \overline{V}_{21}, \tag{6.29}$$

$$\overline{V}_{12} = \overline{V}_{L_2} + \overline{V}_{r_2} + \overline{V}_{C_2} + \overline{V}_{L_3} + \overline{V}_{r_3} + \overline{V}_{43}, \tag{6.30}$$

$$\overline{V}_{34} = \overline{V}_{L_4} + \overline{V}_{C_4} + \overline{V}_{r_4} + \overline{V}_{R_{eq}}, \tag{6.31}$$

$$\Leftrightarrow \text{Applying Laplace transforms } (s = j.\omega) \Leftrightarrow$$

$$\overline{V}_{in}(s) = s.L_s.\overline{I}_{in}(s) + \frac{1}{s.C_1}\overline{I}_{C_1}(s) + r_s.\overline{I}_{in}(s), \tag{6.28}$$

$$\overline{V}_{C_1}(s) = s.L_1.\overline{I}_1(s) + r_1.\overline{I}_1(s) - s.L_{12}.\overline{I}_2(s), \tag{6.29}$$

$$s.L_{12}.\overline{I}_1(s) = s.L_2.\overline{I}_2(s) + r_2.\overline{I}_2(s) + \frac{1}{s.C_2}\overline{I}_2(s) + s.L_3.\overline{I}_2(s) + r_3.\overline{I}_2(s) - s.L_{34}.\overline{I}_4(s), \tag{6.30}$$

$$s.L_{34}.\overline{I}_2(s) = s.L_4.\overline{I}_4(s) + \frac{1}{s.C_4}\overline{I}_4(s) + r_4.\overline{I}_4(s) + R_{eq}.\overline{I}_4(s), \tag{6.31}$$

$$\Leftrightarrow \text{Assuming } \overline{I}_4(s) = \overline{I}_2(s)\tfrac{s.L_{34}}{(Z_4+R_{eq})} \Leftrightarrow$$

$$s.L_{12}.\overline{I}_1(s) = \overline{I}_2(s)\left(s.L_2 + r_2 + \frac{1}{s.C_2} + s.L_3 + r_3\right) - s.L_{34}\left(\overline{I}_2(s)\frac{s.L_{34}}{(Z_4 + R_{eq})}\right), \Leftrightarrow$$

$$s.L_{12}.\overline{I}_1(s) = \overline{I}_2(s)\left(s.L_2 + s.L_3 + r_2 + r_3 + \frac{1}{s.C_2} + s.L_3 + r_3 + \frac{1}{s.C_2} - \frac{s^2.L_{34}^2}{(Z_4 + R_{eq})}\right), \Leftrightarrow \tag{6.30}$$

$$\overline{I}_2(s) = \overline{I}_1(s)\frac{s.L_{12}}{(Z_2 + Z_{r_{IRMC}})},$$

$$\Leftrightarrow \text{Assuming } \overline{I}_2(s) = \overline{I}_1(s)\tfrac{s.L_{12}}{(Z_2+Z_{r_{IRMC}})} \Leftrightarrow$$

$$\frac{\overline{I}_{in}}{(}s) - \overline{I}_1(s)s.C_1 = s.L_1.\overline{I}_1(s) + r_1.\overline{I}_1(s) - s.L_{12}.\overline{I}_1(s)\frac{s.L_{12}}{(Z_2 + Z_{r_{IRMC}})}, \Leftrightarrow$$

$$\overline{I}_{in}(s) = \overline{I}_1(s) + s.C_1.\overline{I}_1(s)(Z_1 + Z_{r_{ORMC}}), \Leftrightarrow \tag{6.29}$$

$$\overline{I}_{in}(s) = s.C_1.\overline{I}_1(s)\left(Z_1 + Z_{r_{ORMC}} + \frac{1}{s.C_1}\right),$$

$$\Leftrightarrow \text{Assuming } \overline{I}_1(s) = \overline{I}_{in}(s)\frac{1}{s.C_1\left(Z_1+Z_{r_{ORMC}}+\frac{1}{s.C_1}\right)} \Leftrightarrow$$

$$\overline{V}_{in}(s) = s.L_s.\overline{I}_{in}(s) + \frac{1}{s.C_1}\overline{I}_{C_1}(s) + s.r_s.\overline{I}_{in}(s), \Leftrightarrow$$

$$\overline{V}_{in}(s) = \overline{I}_{in}(s)\left(s.L_s + \frac{1}{s.C_1} + r_s - \frac{1}{s^2.C_1^2\left(Z_1 + Z_{r_{ORMC}} + \frac{1}{(s.C_1)}\right)}\right), \tag{6.28}$$

$$\Leftrightarrow \text{Assuming } (s = j.\omega) \text{ to (6.28), (6.29), (6.30) and (6.31)} \Leftrightarrow$$

$$\overline{V}_{in} = r_s.\overline{I}_{in} + j.\omega((L_s - 1/(\omega^2.C_1))\overline{I}_{in} + 1/(\omega^2.C_1)\overline{I}_1), \tag{6.28}$$

$$0 = r_1.\overline{I}_1 + j.\omega(1/(\omega^2.C_1)\overline{I}_{in} + (L_1 - 1/(\omega^2.C_1))\overline{I}_1 - L_{12}.\overline{I}_2), \tag{6.29}$$

$$0 = (r_2 + r_3).\overline{I}_2 + j.\omega((L_2 + L_3 - 1/(\omega^2.C_2))\overline{I}_2 - L_{12}.\overline{I}_1 - L_{34}.\overline{I}_4), \tag{6.30}$$

$$0 = (R_{eq} + r_4).\overline{I}_4 + j.\omega((L_4 - 1/(\omega^2.C_4))\overline{I}_4 - L_{34}.\overline{I}_2), \tag{6.31}$$

## 2. Generic equations for currents and voltages

Through (6.28), (6.29), (6.30) and (6.31), the equations for the currents in the equivalent electrical circuit were defined to better define the LCL-S-S configuration. The equations for the currents are given by

$$\overline{I}_{in}(s) = \frac{\overline{V}_{in}(s)}{Z_{in}} = \frac{\overline{V}_{in}}{r_s + s.L_s + \frac{1}{(s.C_1)} - \frac{1}{s^2.C_1^2\left(Z_1 + Z_{r_{ORMC}} + \frac{1}{(s.C_1)}\right)}}, \tag{6.32}$$

$$\overline{I}_1(s) = \overline{I}_{in}(s)\frac{1}{s.C_1(Z_1 + Z_{r_{ORMC}} + \frac{1}{(s.C_1)})}, \tag{6.33}$$

$$\overline{I}_2(s) = \overline{I}_1(s)\frac{s.L_{12}}{(Z_2 + Z_{r_{IRMC}})}, \tag{6.34}$$

$$\overline{I}_4(s) = \overline{I}_2(s)\frac{s.L_{34}}{(Z_4 + R_{eq})}, \tag{6.35}$$

$\Leftrightarrow$ Applying Laplace transforms $(s = j.\omega)$ $\Leftrightarrow$

$$\overline{I}_{in} = \frac{\overline{V}_{in}}{Z_{in}} = \frac{\overline{V}_{in}}{r_s + j.\omega.L_s + \frac{1}{(j.\omega.C_1)} + \frac{1}{\omega^2.C_1^2\left(Z_1 + Z_{r_{ORMC}} + \frac{1}{(j.\omega.C_1)}\right)}}, \tag{6.32}$$

$$\overline{I}_1 = -\overline{I}_{in}\frac{j}{\omega.C_1(Z_1 + Z_{r_{ORMC}})}, \tag{6.33}$$

$$\overline{I}_2 = \overline{I}_1\frac{j.\omega.L_{12}}{(Z_2 + Z_{r_{IRMC}})}, \tag{6.34}$$

$$\overline{I}_4 = \overline{I}_2\frac{j.\omega.L_{34}}{(Z_4 + R_{eq})}, \tag{6.35}$$

The induced voltages across the coils are expressed by

$$|\overline{V}_{L_s}(s)| = |\overline{I}_{in}(s).(r_s + s.L_s)| \tag{6.36}$$

$$|\overline{V}_{L_1}(s)| = |\overline{I}_1(s).(r_1 + s.L_1 + Z_{r_{ORMC}})| \tag{6.37}$$

$$|\overline{V}_{L_2}(s)| = |\overline{I}_2(s).(r_2 + s.L_3 + 1/(s.C_2) + Z_{r_{IRMC}})| \tag{6.38}$$

$$|\overline{V}_{L_3}(s)| = |\overline{I}_2(s).(r_3 + s.L_3 + Z_{r_{IRMC}})| \tag{6.39}$$

$$|\overline{V}_{L_4}(s)| = |\overline{I}_4(s).(R_{eq} + 1/(s.C_4))| \tag{6.40}$$

$\Leftrightarrow$ Applying Laplace transforms $(s = j.\omega)$ $\Leftrightarrow$

$$|\overline{V}_{L_s}| = |\overline{I}_{in}.(r_s + j.\omega.L_s)| \tag{6.36}$$

$$|\overline{V}_{L_1}| = |\overline{I}_1.(r_1 + j.\omega.L_1 + Z_{r_{ORMC}})| \tag{6.37}$$

$$|\overline{V}_{L_2}| = |\overline{I}_2.(r_2 + j.\omega.L_3 + 1/(j.\omega.C_2) + Z_{r_{IRMC}})| \tag{6.38}$$

$$|\overline{V}_{L_3}| = |\overline{I}_2.(r_3 + j.\omega.L_3 + Z_{r_{IRMC}})| \tag{6.39}$$

$$|\overline{V}_{L_4}| = |\overline{I}_4.(R_{eq} + 1/(j.\omega.C_4))| \tag{6.40}$$

## 3. Equations for capacitors

The equations for capacitors allow us to determine the resonant frequency and control the energy transfer between the MC coils. Fig. 6.4 illustrates the different meshes where the following capacitors are placed.

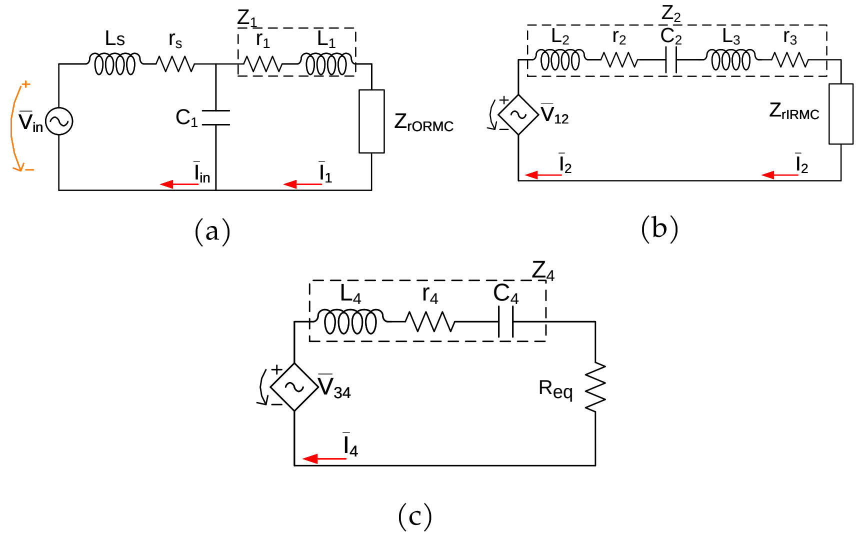


Figure 6.4: (a) $C_1$ mesh, (b) $C_2$ mesh and (c) $C_4$ mesh

According to the Fig. 6.4, the Kirchhoff's equations of the different meshes are

$$\overline{V}_{in}(s) = \left(s.L_s + \frac{1}{s.C_1} + r_s\right)\overline{I}_{in}(s) - \frac{1}{s.C_1}\overline{I}_1(s), \tag{6.41}$$

$$Z_{rORMC}.\overline{I}_1(s) = \frac{1}{s.C_1}\overline{I}_{in}(s) - \left(s.L_1 + \frac{1}{s.C_1} + r_1\right)\overline{I}_1(s), \tag{6.42}$$

$$\overline{V}_{12}(s) = \left(s.L_2 + s.L_3 + \frac{1}{s.C_2} + r_2 + r_3\right)\overline{I}_2(s) + Z_{rIRMC}.\overline{I}_2(s), \tag{6.43}$$

$$\overline{V}_{34}(s) = \left(s.L_4 + \frac{1}{s.C_4} + r_4\right)\overline{I}_4(s) + R_{eq}.\overline{I}_4(s), \tag{6.44}$$

$\Leftrightarrow$ Applying Laplace transforms $(s = j.\omega)$ and $(r_s = r_1 = r_2 = r_3 = r_4 = 0\ \Omega)$ $\Leftrightarrow$

$$\overline{V}_{in} = \left(j.\omega.L_s + \frac{1}{j.\omega.C_1}\right)\overline{I}_{in} - \frac{1}{j.\omega.C_1}.\overline{I}_{in}, \tag{6.41}$$

$$Z_{rORMC}.\overline{I}_1 = \frac{1}{j.\omega.C_1}\overline{I}_{in} - \left(j.\omega.L_1 + \frac{1}{j.\omega.C_1}\right)\overline{I}_1 \tag{6.42}$$

$$\overline{V}_{12} = \left(j.\omega.L_2 + j.\omega.L_3 + \frac{1}{j.\omega.C_2}\right)\overline{I}_2 + Z_{rIRMC}.\overline{I}_2, \tag{6.43}$$

$$\overline{V}_{34} = \left(j.\omega.L_4 + \frac{1}{j.\omega.C_4}\right)\overline{I}_4 + R_{eq}.\overline{I}_4, \tag{6.44}$$

From (6.41), (6.42), (6.43), (6.44) and assuming the imaginary part equal to 0, the following equations are expressed by

$$\begin{aligned} \omega_1.L_s - \frac{1}{\omega_1.C_1} &= 0 \\ \omega_1.L_1 - \frac{1}{\omega_1.C_1} &= 0 \end{aligned} \tag{6.45}$$

$$\omega_2(L_2 + L_3) - \frac{1}{\omega_2.C_2} = 0 \tag{6.46}$$

$$\omega_4.L_4 - \frac{1}{\omega_4.C_4} = 0 \tag{6.47}$$

$\Leftrightarrow$ Assuming $(\omega_1 = \omega_2 = \omega_4 = \omega)$ [48] $\Leftrightarrow$

$$C_1 = 1/(\omega^2.L_1) = 1/(\omega^2.L_s), \tag{6.45}$$

$$C_2 = 1/(\omega^2.(L_2 + L_3)), \tag{6.46}$$

$$C_4 = 1/(\omega^2.L_4). \tag{6.47}$$

## 4. Equations for impedances

The equations for impedances contribute to determining the equations for the voltage and transconductance gains, where these equations allow the identification of the loading profiles of each configuration. The equations for the impedances are given by

$$Z_1(s) = s.L_1 + r_1, \tag{6.48}$$

$$Z_2(s) = s.L_2 + s.L_3 + r_2 + r_3 + \frac{1}{s.C_2}, \tag{6.49}$$

$$Z_4(s) = s.L_4 + r_4 + \frac{1}{s.C_4}, \tag{6.50}$$

$\Leftrightarrow$ Applying Laplace transforms $(s = j.\omega)$ and $\omega_x = \frac{1}{\sqrt{L_x.C_x}}$ $\Leftrightarrow$

$$Z_1 = r_1 + j.\omega.L_1, \tag{6.48}$$

$$Z_2 = (r_2 + r_3) + j.\omega.(L_2 + L_3 - 1/(\omega^2.C_2)), \tag{6.49}$$

$$Z_4 = r_4 + j.\omega(L_4 - 1/(\omega^2.C_4)), \tag{6.50}$$

## 5. Equations for reflected impedances under resonance and ideal conditions

The equations for the reflected impedances contribute to determining the equations for the voltage and transconductance gains, where these equations allow the identification of the loading profiles of each configuration. The equations for the reflected impedances are given by

$$Z_{r_{IRMC}}(s) = -\frac{s^2.L_{34}^2}{(Z_4 + R_{eq})}, \tag{6.51}$$

$$Z_{r_{ORMC}}(s) = -\frac{s^2.L_{12}^2}{(Z_2 + Z_{r_{IRMC}}(s))}, \tag{6.52}$$

$\Leftrightarrow$ Applying Laplace transforms $(s = j.\omega)$ and
considering the conditions $(r_s = r_1 = r_2 = r_3 = r_4 = 0\ \Omega)$ e $(\omega = \omega_x)$ $\Leftrightarrow$

$$Z_{r_{IRMC}} = \frac{\omega^2.L_{34}^2}{R_{eq}}, \tag{6.51}$$

$$Z_{r_{ORMC}} = \frac{\frac{\omega^2.L_{12}^2}{1}}{\frac{\omega^2.L_{34}^2}{R_{eq}}} = \frac{\omega^2.L_{12}^2(Z_4 + R_{eq})}{(Z_2(Z_4 + R_{eq}) + \omega^2.L_{34}^2)} = \frac{L_{12}^2.R_{eq}}{L_{34}^2}, \tag{6.52}$$

## 6. Input impedance

The input impedance $Z_{in}$ is the equivalent impedance seen by the power supply and it is the aggregated of the reflected impedance from IRMC and the receiver side ORMC onto the transmitter side ORMC and the equivalent impedances of the transmitter side ORMC and input side. The equation of $Z_{in}$ is shown by

$$Z_{in}(s) = r_s + s.L_s + \frac{1}{s.C_1} - \frac{1}{s^2.C_1^2\left(Z_1 + Z_{r_{ORMC}} + \frac{1}{s.C_1}\right)}. \tag{6.53}$$

If the system losses are neglected $(r_s = r_1 = r_2 = r_3 = r_4 = 0\ \Omega)$, apply the Laplace transforms $(s = j.\omega)$, the system is under resonance $(\omega = \omega_x)$ and $L_s = L_1$, using MATLAB simplify function, (6.53) is defined by

$$Z_{in} = \frac{\omega^2.L_1^2.L_{34}^2}{L_{12}^2.R_{eq}}. \tag{6.54}$$

Assuming the mentioned conditions, (6.54) is purely resistive and depends on the ratio of $L_{34}^2/L_{12}^2$, $L_1^2$ and $\omega^2$.

## 7. Voltage and transconductance gain equations

The equations of voltage gains and transconductance where these equations allow identifying the loading profiles of each configuration. Considering the current equations, it is possible to determine the equations for the gains that are given by

$$G_{vReqvin} = \frac{\overline{V}_{R_{eq}}}{\overline{V}_{in}}, \tag{6.55}$$

$$G_{i4vin} = \frac{\overline{I}_4}{\overline{V}_{in}}, \tag{6.56}$$

$$G_{i2vin} = \frac{\overline{I}_2}{\overline{V}_{in}}, \tag{6.57}$$

$$G_{i1vin} = \frac{\overline{I}_1}{\overline{V}_{in}}, \tag{6.58}$$

⇔ Applying the equalities between the equations of the currents and highlighting ⇔

$$G_{vReqvin}(s) = \frac{R_{eq}(s.L_{12}.L_{34})}{C_1(Z_4+R_{eq})(Z_2+Z_{r_{IRMC}})\left(Z_1+\frac{1}{(s.C_1)}+Z_{r_{ORMC}}\right)\left(r_s+s.L_s+\frac{1}{(s.C_1)}-\frac{1}{s^2.C_1^2\left(Z_1+Z_{r_{ORMC}}+\frac{1}{(s.C_1)}\right)}\right)}, \tag{6.55}$$

$$G_{i4vin}(s) = \frac{(s.L_{12}.L_{34})}{C_1(Z_4+R_{eq})(Z_2+Z_{r_{IRMC}})\left(Z_1+\frac{1}{(s.C_1)}+Z_{r_{ORMC}}\right)\left(r_s+s.L_s+\frac{1}{(s.C_1)}-\frac{1}{s^2.C_1^2\left(Z_1+Z_{r_{ORMC}}+\frac{1}{(s.C_1)}\right)}\right)}, \tag{6.56}$$

$$G_{i2vin}(s) = \frac{L_{12}}{C_1(Z_2+Z_{r_{IRMC}})\left(Z_1+\frac{1}{(s.C_1)}+Z_{r_{ORMC}}\right)\left(r_s+s.L_s+\frac{1}{(s.C_1)}-\frac{1}{s^2.C_1^2\left(Z_1+Z_{r_{ORMC}}+\frac{1}{(s.C_1)}\right)}\right)}. \tag{6.57}$$

$$G_{i1vin}(s) = \frac{1}{s.C_1\left(Z_1+\frac{1}{(s.C_1)}+Z_{r_{ORMC}}\right)\left(r_s+s.L_s+\frac{1}{(s.C_1)}-\frac{1}{s^2.C_1^2\left(Z_1+Z_{r_{ORMC}}+\frac{1}{(s.C_1)}\right)}\right)}. \tag{6.58}$$

⇔ Applying Laplace transforms $(s = j.\omega)$ ⇔

$$G_{vReqvin} = \frac{j.\omega.R_{eq}.L_{12}.L_{34}}{C_1(R_{eq}+Z_4)\left(Z_1+Z_{r_{ORMC}}+\frac{1}{(j.\omega.C_1)}\right)(Z_2+Z_{r_{IRMC}})\left(r_s+j.\omega.L_s+\frac{1}{(j.\omega.C_1)}+\frac{1}{C_1^2.\omega^2\left(Z_1+Z_{r_{ORMC}}+\frac{1}{(j.\omega.C_1)}\right)}\right)}. \tag{6.55}$$

$$G_{i4vin} = \frac{j.\omega.L_{12}.L_{34}}{C_1(R_{eq}+Z_4)\left(Z_1+Z_{r_{ORMC}}+\frac{1}{(j.\omega.C_1)}\right)(Z_2+Z_{r_{IRMC}})\left(r_s+j.\omega.L_s+\frac{1}{(j.\omega.C_1)}+\frac{1}{C_1^2.\omega^2\left(Z_1+Z_{r_{ORMC}}+\frac{1}{(j.\omega.C_1)}\right)}\right)}. \tag{6.56}$$

$$G_{i2vin} = \frac{L_{12}}{C_1\left(Z_1+Z_{r_{ORMC}}+\frac{1}{(j.\omega.C_1)}\right)(Z_2+Z_{r_{IRMC}})\left(r_s+j.\omega.L_s+\frac{1}{(j.\omega.C_1)}+\frac{1}{C_1^2.\omega^2\left(Z_1+Z_{r_{ORMC}}+\frac{1}{(j.\omega.C_1)}\right)}\right)}. \tag{6.57}$$

$$G_{i1vin} = -\frac{j}{C_1.\omega\left(Z_1+Z_{r_{ORMC}}+\frac{1}{(j.\omega.C_1)}\right)\left(r_s+j.\omega.L_s+\frac{1}{(j.\omega.C_1)}+\frac{1}{C_1^2.\omega^2\left(Z_1+Z_{r_{ORMC}}+\frac{1}{(j.\omega.C_1)}\right)}\right)}. \tag{6.58}$$

$\Leftrightarrow$ If the system is under resonance $(\omega = \omega_x)$, $(r_s = r_1 = r_2 = r_3 = r_4 = 0\ \Omega)$ and $L_s = L_1$, using MATLAB simplify function $\Leftrightarrow$

$$G_{vReqvin} = \frac{j.R_{eq}.L_{12}}{L_1.L_{34}.\omega}. \tag{6.55}$$

$$G_{i4vin} = \frac{j.L_{12}}{L_1.L_{34}.\omega}. \tag{6.56}$$

$$G_{i2vin} = \frac{R_{eq}.L_{12}}{L_1.L_{34}^2.\omega^2}. \tag{6.57}$$

$$G_{i1vin} = -\frac{j}{\omega.L_1}. \tag{6.58}$$

# Anexo C - Analysis of the proposed electrical circuit with LCC-S configuration

## 1. Generic equations

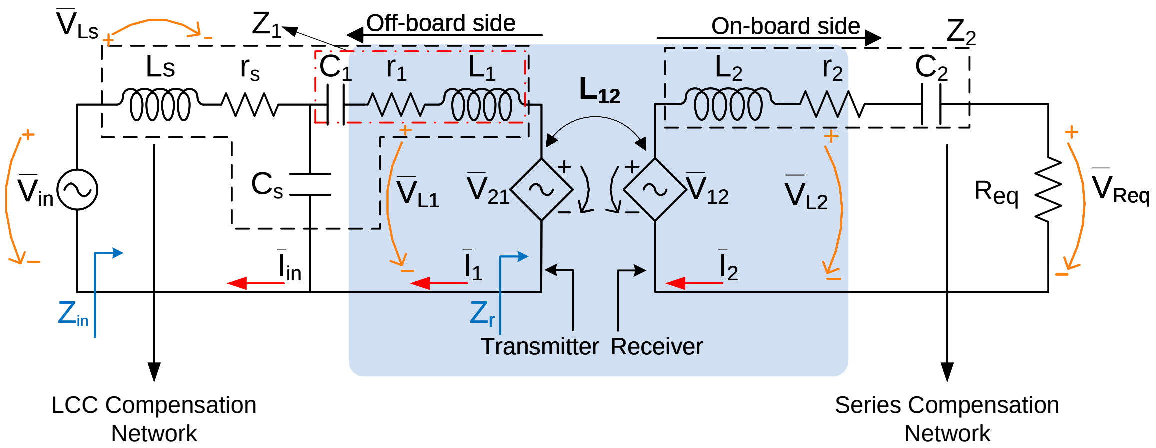


Figure 6.5: Equivalent circuit model of a IPT with LCC-S resonant compensation.

Applying Kirchhoff's laws to analyze the equivalent circuit of the LCC-S configuration, the following equations are obtained:

$$\overline{V}_{in} = \overline{V}_{L_s} + \overline{V}_{C_s} + \overline{V}_{r_s}, \tag{6.59}$$

$$\overline{V}_{C_s} = \overline{V}_{L_1} + \overline{V}_{C_1} + \overline{V}_{r_1} + \overline{V}_{21}, \tag{6.60}$$

$$\overline{V}_{12} = \overline{V}_{L_2} + \overline{V}_{r_2} + \overline{V}_{C_2} + \overline{V}_{R_{eq}}, \tag{6.61}$$

$\Leftrightarrow$ Applying Laplace transforms $(s = j.\omega)$ $\Leftrightarrow$

$$\overline{V}_{in}(s) = s.L_s.\overline{I}_{in}(s) + \frac{1}{s.C_s}\overline{I}_{C_s}(s) + s.r_s.I_{in}(s), \tag{6.59}$$

$$\overline{V}_{C_s}(s) = \frac{1}{s.C_1}\overline{I}_1(s) + s.L_1.\overline{I}_1(s) + s.r_1.\overline{I}_1(s) - s.L_{12}.\overline{I}_2(s), \tag{6.60}$$

$$s.L_{12}.\overline{I}_1(s) = s.L_2.\overline{I}_2(s) + r_2.\overline{I}_2(s) + \frac{1}{s.C_2}\overline{I}_2(s) + R_{eq}.\overline{I}_4(s), \tag{6.61}$$

$$\Leftrightarrow \text{Assuming } \overline{I}_2(s) = \overline{I}_1(s)\frac{s.L_{12}}{(Z_2+R_{eq})} \Leftrightarrow$$

$$\frac{\overline{I}_{in}(s) - \overline{I}_1(s)}{s.C_s} = \frac{1}{s.C_1}\overline{I}_1(s) + s.L_1.\overline{I}_1(s) + r_1.\overline{I}_1(s) - s.L_{12}.\overline{I}_1(s)\frac{s.L_{12}}{(Z_2+R_{eq})}, \Leftrightarrow$$

$$\overline{I}_{in}(s) = \overline{I}_1(s) + s.C_s.\overline{I}_1(s)(Z_1 + Z_r), \Leftrightarrow \tag{6.60}$$

$$\overline{I}_{in}(s) = s.C_s.\overline{I}_1(s)\left(Z_1 + Z_r + \frac{1}{s.C_s}\right),$$

$$\Leftrightarrow \text{Assuming } \overline{I}_1(s) = \overline{I}_{in}(s)\frac{1}{s.C_s\left(Z_1+Z_r+\frac{1}{s.C_s}\right)} \Leftrightarrow$$

$$\overline{V}_{in}(s) = s.L_s.\overline{I}_{in}(s) + \frac{1}{s.C_s}\overline{I}_{C_s}(s) + s.r_s.\overline{I}_{in}(s), \Leftrightarrow$$

$$\overline{V}_{in}(s) = \overline{I}_{in}(s)\left(s.L_s + \frac{1}{s.C_s} + r_s - \frac{1}{s^2.C_s^2\left(Z_1 + Z_r + \frac{1}{s.C_s}\right)}\right), \tag{6.59}$$

$$\Leftrightarrow \text{Assuming } (s = j.\omega) \text{ to (6.59), (6.60) and (6.61)} \Leftrightarrow$$

$$\overline{V}_{in} = r_s.\overline{I}_{in} + j.\omega((L_s - 1/(\omega^2.C_s))\overline{I}_{in} + 1/(\omega^2.C_s)\overline{I}_1), \tag{6.59}$$

$$0 = r_1.\overline{I}_1 + j.\omega(1/(\omega^2.C_s)\overline{I}_{in} + (L_1 - 1/(\omega^2.C_1) - 1/(\omega^2.C_s))\overline{I}_1 - L_{12}.\overline{I}_2), \tag{6.60}$$

$$0 = (r_2 + R_{eq}).\overline{I}_2 + j.\omega((L_2 - 1/(\omega^2.C_2))\overline{I}_2 - L_{12}.\overline{I}_1), \tag{6.61}$$

## 2. Generic equations for currents and voltages

Through (6.59), (6.60) and (6.61), the equations for the currents in the equivalent electrical circuit were defined to better define the LCC-S configuration. The equations for the currents are given by:

$$\overline{I}_{in}(s) = \frac{\overline{V}_{in}(s)}{Z_{in}} = \frac{\overline{V}_{in}(s)}{r_s + s.L_s + \frac{1}{(s.C_s)} + \frac{1}{s^2.C_s^2\left(Z_1+Z_r+\frac{1}{(s.C_s)}\right)}}, \tag{6.62}$$

$$\overline{I}_1(s) = \overline{I}_{in}(s)\frac{1}{s.C_s\left(Z_1 + Z_r + \frac{1}{(s.C_s)}\right)}, \tag{6.63}$$

$$\overline{I}_2(s) = \overline{I}_1(s)\frac{s.L_{12}}{(Z_2 + R_{eq})}, \tag{6.64}$$

$$\Leftrightarrow \text{Applying Laplace transforms } (s = j.\omega) \Leftrightarrow$$

$$\overline{I}_{in} = \frac{\overline{V}_{in}}{Z_{in}} = \frac{\overline{V}_{in}}{r_s + j.\omega.L_s + \frac{1}{(j.\omega.C_s)} + \frac{1}{\omega^2.C_s^2\left(Z_1+Z_r+\frac{1}{(j.\omega.C_s)}\right)}}, \tag{6.62}$$

$$\overline{I}_1 = -\overline{I}_{in} \frac{j}{\omega.C_s\left(Z_1 + Z_r + \frac{1}{(j.\omega.C_s)}\right)}, \tag{6.63}$$

$$\overline{I}_2 = \overline{I}_1 \frac{j.\omega.L_{12}}{(Z_2 + R_{eq})}, \tag{6.64}$$

The induced voltages across the coils are expressed by

$$|\overline{V}_{L_s}(s)| = |\overline{I}_{in}(s).(r_s + s.L_s)| \tag{6.65}$$

$$|\overline{V}_{L_1}(s)| = |\overline{I}_1(s).(r_1 + s.L_1 + Z_{r_{ORMC}})| \tag{6.66}$$

$$|\overline{V}_{L_2}(s)| = |\overline{I}_2(s).(R_{eq} + 1/(s.C_2))| \tag{6.67}$$

$\Leftrightarrow$ Applying Laplace transforms $(s = j.\omega)$ $\Leftrightarrow$

$$|\overline{V}_{L_s}| = |\overline{I}_{in}.(r_s + j.\omega.L_s)| \tag{6.65}$$

$$|\overline{V}_{L_1}| = |\overline{I}_1.(r_1 + j.\omega.L_1 + Z_{r_{ORMC}})| \tag{6.66}$$

$$|\overline{V}_{L_2}| = |\overline{I}_2.(R_{eq} + 1/(j.\omega.C_2))| \tag{6.67}$$

## 3. Equations for capacitors

The equations for capacitors allow us to determine the resonant frequency and control the energy transfer between the MC coils. Fig. 6.6 illustrates the different meshes where the following capacitors are placed.

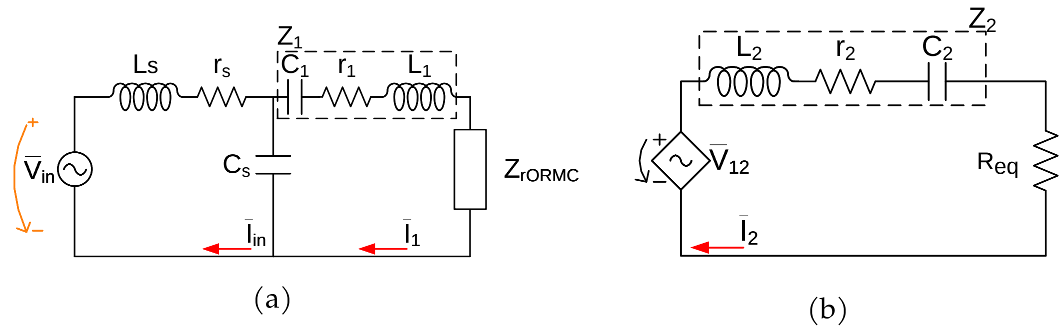


Figure 6.6: (a) $C_s$ and $C_1$ mesh and (b) $C_2$ mesh

According to the Fig. 6.6, the Kirchhoff's equations of the different meshes are

$$\overline{V}_{in}(s) = \left(s.L_s + \frac{1}{(s.C_s)} + r_s\right)\overline{I}_{in}(s) - \frac{1}{(s.C_s)}\overline{I}_1(s), \tag{6.68}$$

$$Z_{r_{ORMC}}.\overline{I}_1(s) = \frac{1}{(s.C_s)}\overline{I}_{in}(s) - \left(s.L_1 + \frac{1}{(s.C_s)} + \frac{1}{(s.C_1)} + r_1\right)\overline{I}_1(s), \tag{6.69}$$

$$\overline{V}_{12}(s) = \left(s.L_2 + \frac{1}{(s.C_2)} + r_2\right)\overline{I}_{2_{(s)}} + R_{eq}.\overline{I}_2(s), \tag{6.70}$$

$\Leftrightarrow$ Applying Laplace transforms $(s = j.\omega)$ and $(r_s = r_1 = r_2 = 0)$ $\Leftrightarrow$

$$\overline{V}_{in} = \left(j.\omega.L_s + \frac{1}{(j.\omega.C_s)}\right)\overline{I}_{in} - \frac{1}{(j.\omega.C_s)}.\overline{I}_{in}, \tag{6.68}$$

$$Z_{r_{ORMC}}.\overline{I}_1 = \frac{1}{(j.\omega.C_1)}\overline{I}_{in} - \left(j.\omega.L_1 + \frac{1}{(j.\omega.C_1)}\right)\overline{I}_1 \tag{6.69}$$

$$\overline{V}_{12} = \left(j.\omega.L_2 + \frac{1}{(j.\omega.C_2)}\right)\overline{I}_2 + R_{eq}.\overline{I}_2, \tag{6.70}$$

From (6.68), (6.69), (6.70) and assuming the imaginary part equal to 0, the following equations are expressed by

$$\omega_s.L_s - \frac{1}{(\omega_s.C_s)} = 0 \tag{6.71}$$

$$\begin{aligned} \omega_1.L_1 - \frac{1}{(\omega_s.C_s)} - \frac{1}{(\omega_1.C_s)} &= 0 \\ \omega_1.L_1 - \omega_s.L_s - \frac{1}{(\omega_1.C_s)} &= 0 \end{aligned} \tag{6.72}$$

$$\omega_2.L_2 - \frac{1}{(\omega_2.C_2)} = 0 \tag{6.73}$$

$\Leftrightarrow$ Assuming $(\omega_s = \omega_1 = \omega_2 = \omega)$ [50] $\Leftrightarrow$

$$C_s = 1/(\omega^2.L_s), \tag{6.71}$$

$$C_1 = 1/(\omega^2.(L_1 - L_s)), \tag{6.72}$$

$$C_2 = 1/(\omega^2.L_2), \tag{6.73}$$

## 4. Equations for impedances

The equations for impedances contribute to determining the equations for the voltage and transconductance gains, where these equations allow the identification of the loading profiles of each configuration. The equations for the impedances are given by

$$Z_1(s) = s.L_1 + r_1 + \frac{1}{s.C_1}, \tag{6.74}$$

$$Z_2(s) = s.L_2 + r_2 + \frac{1}{s.C_2}, \tag{6.75}$$

$\Leftrightarrow$ Applying Laplace transforms $(s = j.\omega)$ and $\omega_x = \frac{1}{\sqrt{L_x.C_x}}$ $\Leftrightarrow$

$$Z_1 = r_1 + j.\omega(L_1 - 1/(\omega^2.C_1)), \tag{6.74}$$

$$Z_2 = r_2 + j.\omega.(L_2 - 1/(\omega^2.C_2)), \tag{6.75}$$

## 5. Equations for reflected impedances under resonance and ideal conditions

The equations for the reflected impedances contribute to determining the equations for the voltage and transconductance gains, where these equations allow the identification of the loading profiles of each configuration. The equations for the reflected impedances are given by

$$Z_r(s) = -\frac{s^2.L_{12}^2}{(Z_2 + R_{eq})} \tag{6.76}$$

⇔ Applying Laplace transforms $(s = j.\omega)$ and
considering the conditions $(r_1 = r_2 = r_3 = r_4 = 0)$ e $(\omega = \omega_x)$ ⇔

$$Z_r = \frac{\omega^2.L_{12}^2}{R_{eq}} \tag{6.76}$$

## 6. Input impedance

The input impedance $Z_{in}$ is the equivalent impedance seen by the power supply and it is the aggregated of the reflected impedance from IRMC and the receiver side ORMC onto the transmitter side ORMC and the equivalent impedances of the transmitter side ORMC and input side. The equation of $Z_{in}$ is shown by

$$Z_{in}(s) = r_s + s.L_s + \frac{1}{(s.C_s)} - \frac{1}{s^2.C_s^2\left(Z_1 + Z_r + \frac{1}{(s.C_s)}\right)}. \tag{6.77}$$

If the system losses are neglected $(r_s = r_1 = r_2 = 0)$, apply the Laplace transforms $(s = j.\omega)$ and the system is under resonance $(\omega = \omega_x)$, using MATLAB simplify function, (6.77) is defined by

$$Z_{in} = \frac{R_{eq}.L_s^2}{L_{12}^2}. \tag{6.78}$$

Assuming the mentioned conditions, (6.78) is purely resistive and depends on the ratio of $L_{34}^2/L_{12}^2$, $L_s^2$.

## 7. Voltage and transconductance gain equations

The equations of voltage gains and transconductance where these equations allow identifying the loading profiles of each configuration. Considering the current equations, it is possible to determine the equations for the gains that are given by

$$G_{vReqvin} = \frac{\overline{V}_{R_{eq}}}{\overline{V}_{in}}, \tag{6.79}$$

$$G_{i2vin} = \frac{\overline{I}_2}{\overline{V}_{in}}, \tag{6.80}$$

$$G_{i1vin} = \frac{\overline{I}_1}{\overline{V}_{in}}, \tag{6.81}$$

⇔ Applying the equalities between the equations of the currents and highlighting ⇔

$$G_{vReqvin}(s) = \frac{R_{eq}.L_{12}}{C_s(Z_2+R_{eq})\left(Z_1+\frac{1}{(s.C_s)}+Z_r\right)\left(r_s+s.L_s+\frac{1}{(s.C_s)}-\frac{1}{s^2.C_s^2\left(Z_1+Z_r+\frac{1}{(s.C_s)}\right)}\right)}, \tag{6.79}$$

$$G_{i2vin}(s) = \frac{L_{12}}{C_s(Z_2+R_{eq})\left(Z_1+\frac{1}{(s.C_s)}+Z_r\right)\left(r_s+s.L_s+\frac{1}{(s.C_s)}-\frac{1}{s^2.C_s^2\left(Z_1+Z_r+\frac{1}{(s.C_s)}\right)}\right)}, \tag{6.80}$$

$$G_{i1vin}(s) = \frac{1}{s.C_s\left(Z_1+\frac{1}{(s.C_s)}+Z_r\right)\left(r_s+s.L_s+\frac{1}{(s.C_s)}-\frac{1}{s^2.C_s^2\left(Z_1+Z_r+\frac{1}{(s.C_s)}\right)}\right)}, \tag{6.81}$$

⇔ Applying Laplace transforms $(s = j.\omega)$ ⇔

$$G_{vReqvin} = \frac{R_{eq}.L_{12}}{C_s(Z_2+R_{eq})\left(Z_1+\frac{1}{(j.\omega.C_s)}+Z_r\right)\left(r_s+j.\omega.L_s+\frac{1}{(j.\omega.C_s)}+\frac{1}{\omega^2.C_s^2\left(Z_1+Z_r+\frac{1}{(j.\omega.C_s)}\right)}\right)}, \tag{6.79}$$

$$G_{vReqvin} = \frac{L_{12}}{C_s(Z_2+R_{eq})\left(Z_1+\frac{1}{(j.\omega.C_s)}+Z_r\right)\left(r_s+j.\omega.L_s+\frac{1}{(j.\omega.C_s)}+\frac{1}{\omega^2.C_s^2\left(Z_1+Z_r+\frac{1}{(j.\omega.C_s)}\right)}\right)}, \tag{6.80}$$

$$G_{i1vin} = -\frac{j}{\omega.C_s\left(Z_1+\frac{1}{(j.\omega.C_s)}+Z_r\right)\left(r_s+j.\omega.L_s+\frac{1}{(s.C_s)}+\frac{1}{\omega^2.C_s^2\left(Z_1+Z_r+\frac{1}{(j.\omega.C_s)}\right)}\right)}, \tag{6.81}$$

⇔ If the system is under resonance $(\omega = \omega_x)$ and $(r_1 = r_2 = r_3 = r_4 = 0\ \Omega)$,
using MATLAB simplify function ⇔

$$G_{vReqvin} = \frac{L_{12}}{L_s}. \tag{6.79}$$

$$G_{i2vin} = \frac{L_{12}}{L_s.R_{eq}}. \tag{6.80}$$

$$G_{i1vin} = -\frac{j}{\omega.L_s}. \tag{6.81}$$

# Appendix D - Analysis of the proposed electrical circuit with LCC-S-S configuration

## 1. Generic equations

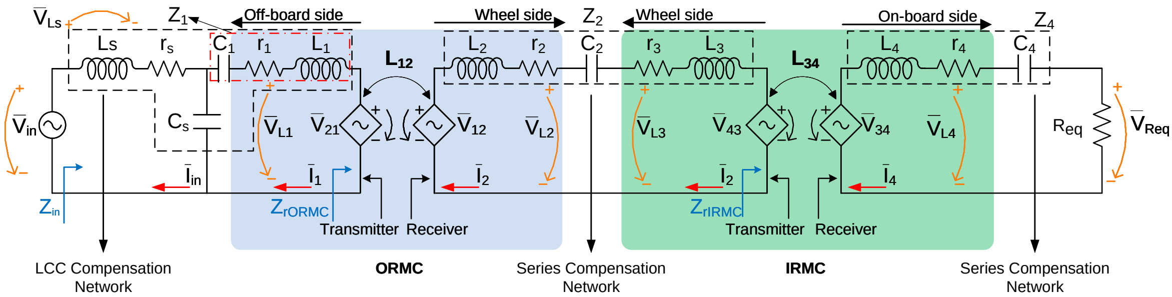


Figure 6.7: Equivalent circuit model of a double coupling inWIPT with LCC-S-S resonant compensation.

Applying Kirchhoff's laws to analyze the equivalent circuit of the LCC-S-S configuration, the following equations are obtained:

$$\overline{V}_{in} = \overline{V}_{L_s} + \overline{V}_{C_s} + \overline{V}_{r_s}, \tag{6.82}$$

$$\overline{V}_{C_s} = \overline{V}_{L_1} + \overline{V}_{C_1} + \overline{V}_{r_1} + \overline{V}_{21}, \tag{6.83}$$

$$\overline{V}_{12} = \overline{V}_{L_2} + \overline{V}_{r_2} + \overline{V}_{C_2} + \overline{V}_{L_3} + \overline{V}_{r_3} + \overline{V}_{43}, \tag{6.84}$$

$$\overline{V}_{34} = \overline{V}_{L_4} + \overline{V}_{C_4} + \overline{V}_{r_4} + \overline{V}_{R_{eq}}, \tag{6.85}$$

$\Leftrightarrow$ Applying Laplace transforms $(s = j.\omega)$ $\Leftrightarrow$

$$\overline{V}_{in}(s) = s.L_s.\overline{I}_{in}(s) + \frac{1}{s.C_s}\overline{I}_{C_s}(s) + r_s.I_{in}(s), \tag{6.82}$$

$$\overline{V}_{C_s}(s) = \frac{1}{s.C_1}\overline{I}_1(s) + s.L_1.\overline{I}_1(s) + r_1.\overline{I}_1(s) - s.L_{12}.\overline{I}_2(s), \tag{6.83}$$

$$s.L_{12}.\overline{I}_1(s) = s.L_2.\overline{I}_2(s) + r_2.\overline{I}_2(s) + \frac{1}{s.C_2}\overline{I}_2(s) + s.L_3.\overline{I}_2(s) + r_3.\overline{I}_2(s) - s.L_{34}.\overline{I}_4(s), \tag{6.84}$$

$$s.L_{34}.\overline{I}_2(s) = s.L_4.\overline{I}_4(s) + \frac{1}{s.C_4}\overline{I}_4(s) + r_4.\overline{I}_4(s) + R_{eq}.\overline{I}_4(s), \tag{6.85}$$

$$\Leftrightarrow \text{Assuming } \overline{I}_4(s) = \overline{I}_2(s)\tfrac{s.L_{34}}{(Z_4+R_{eq})} \Leftrightarrow$$

$$s.L_{12}.\overline{I}_1(s) = \overline{I}_2(s)\left(s.L_2 + r_2 + \frac{1}{s.C_2} + s.L_3 + r_3\right) - s.L_{34}\left(\overline{I}_2(s)\frac{s.L_{34}}{(Z_4+R_{eq})}\right), \Leftrightarrow$$

$$s.L_{12}.\overline{I}_1(s) = \overline{I}_2(s)\left(s.L_2 + s.L_3 + r_2 + r_3 + \frac{1}{s.C_2} + s.L_3 + r_3 + \frac{1}{s.C_2} - \frac{s^2.L_{34}^2}{(Z_4+R_{eq})}\right), \Leftrightarrow \tag{6.84}$$

$$\overline{I}_2(s) = \overline{I}_1(s)\frac{s.L_{12}}{(Z_2 + Z_{r_{IRMC}})},$$

$$\Leftrightarrow \text{Assuming } \overline{I}_2(s) = \overline{I}_1(s)\tfrac{s.L_{12}}{(Z_2+Z_{r_{IRMC}})} \Leftrightarrow$$

$$\frac{\overline{I}_{in}(s) - \overline{I}_1(s)}{s.C_s} = \frac{1}{s.C_1}\overline{I}_1(s) + s.L_1.\overline{I}_1(s) + r_1.\overline{I}_1(s) - s.L_{12}.\overline{I}_1(s)\frac{s.L_{12}}{(Z_2+Z_{r_{IRMC}})}, \Leftrightarrow$$

$$\overline{I}_{in}(s) = \overline{I}_1(s) + s.C_s.\overline{I}_1(s)(Z_1 + Z_{r_{ORMC}}), \Leftrightarrow \tag{6.83}$$

$$\overline{I}_{in}(s) = s.C_s.\overline{I}_1(s)\left(Z_1 + Z_{r_{ORMC}} + \frac{1}{s.C_s}\right),$$

$$\Leftrightarrow \text{Assuming } \overline{I}_1(s) = \overline{I}_{in}(s)\tfrac{1}{s.C_s\left(Z_1+Z_{r_{ORMC}}+\frac{1}{s.C_s}\right)} \Leftrightarrow$$

$$\overline{V}_{in}(s) = s.L_s.\overline{I}_{in}(s) + \frac{1}{s.C_s}\overline{I}_{C_s}(s) + s.r_s.\overline{I}_{in}(s), \Leftrightarrow$$

$$\overline{V}_{in}(s) = \overline{I}_{in}(s)\left(s.L_s + \frac{1}{s.C_s} + r_s - \frac{1}{s^2.C_s^2\left(Z_1 + Z_{r_{ORMC}} + \frac{1}{s.C_s}\right)}\right), \tag{6.82}$$

$$\Leftrightarrow \text{Assuming } (s = j.\omega) \text{ to (6.82), (6.83), (6.84) and (6.85)} \Leftrightarrow$$

$$\overline{V}_{in} = r_s.\overline{I}_{in} + j.\omega((L_s - 1/(\omega^2.C_s))\overline{I}_{in} + 1/(\omega^2.C_s)\overline{I}_1), \tag{6.82}$$

$$0 = r_1.\overline{I}_1 + j.\omega(1/(\omega^2.C_s)\overline{I}_{in} + (L_1 - 1/(\omega^2.C_1) - 1/(\omega^2.C_s))\overline{I}_1 - L_{12}.\overline{I}_2), \tag{6.83}$$

$$0 = (r_2 + r_3).\overline{I}_2 + j.\omega((L_2 + L_3 - 1/(\omega^2.C_2))\overline{I}_2 - L_{12}.\overline{I}_1 - L_{34}.\overline{I}_4), \tag{6.84}$$

$$0 = (R_{eq} + r_4).\overline{I}_4 + j.\omega((L_4 - 1/(\omega^2.C_4))\overline{I}_4 - L_{34}.\overline{I}_2), \tag{6.85}$$

## 2. Generic equations for currents and voltages

Through (6.82), (6.83), (6.84) and (6.85), the equations for the currents in the equivalent electrical circuit were defined to better define the LCC-S-S configuration. The equations for the currents are given by:

$$\overline{I}_{in}(s) = \frac{\overline{V}_{in}}{Z_{in}(s)} = \frac{\overline{V}_{in}}{r_s + s.L_s + \frac{1}{(s.C_s)} + \frac{1}{s^2.C_s^2\left(Z_1+Z_{r_{ORMC}}+\frac{1}{(s.C_s)}\right)}}, \tag{6.86}$$

$$\overline{I}_1(s) = \overline{I}_{in}(s)\frac{1}{s.C_s\left(Z_1 + Z_{r_{ORMC}} + \frac{1}{(s.C_s)}\right)}, \tag{6.87}$$

$$\overline{I}_2(s) = \overline{I}_1(s)\frac{s.L_{12}}{(Z_2 + Z_{r_{IRMC}})}, \tag{6.88}$$

$$\overline{I}_4(s) = \overline{I}_2(s)\frac{s.L_{34}}{(Z_4 + R_{eq})}, \tag{6.89}$$

$\Leftrightarrow$ Applying Laplace transforms $(s = j.\omega)$ $\Leftrightarrow$

$$\overline{I}_{in} = \frac{\overline{V}_{in}}{Z_{in}} = \frac{\overline{V}_{in}}{r_s + j.\omega.L_s + \frac{1}{(j.\omega.C_s)} + \frac{1}{\omega^2.C_s^2\left(Z_1 + Z_{r_{ORMC}} + \frac{1}{(j.\omega.C_s)}\right)}}, \tag{6.86}$$

$$\overline{I}_1 = -\overline{I}_{in}\frac{j}{\omega.C_s\left(Z_1 + Z_{r_{ORMC}} + \frac{1}{(j.\omega.C_s)}\right)}, \tag{6.87}$$

$$\overline{I}_2 = \overline{I}_1\frac{j.\omega.L_{12}}{(Z_2 + Z_{r_{IRMC}})}, \tag{6.88}$$

$$\overline{I}_4 = \overline{I}_2\frac{j.\omega.L_{34}}{(Z_4 + R_{eq})}, \tag{6.89}$$

The induced voltages across the coils are expressed by

$$|\overline{V}_{L_s}(s)| = |\overline{I}_{in}(s).(r_s + s.L_s)| \tag{6.90}$$

$$|\overline{V}_{L_1}(s)| = |\overline{I}_1(s).(r_1 + s.L_1 + Z_{r_{ORMC}})| \tag{6.91}$$

$$|\overline{V}_{L_2}(s)| = |\overline{I}_2(s).(r_2 + s.L_3 + 1/(s.C_2) + Z_{r_{IRMC}})| \tag{6.92}$$

$$|\overline{V}_{L_3}(s)| = |\overline{I}_2(s).(r_3 + s.L_3 + Z_{r_{IRMC}})| \tag{6.93}$$

$$|\overline{V}_{L_4}(s)| = |\overline{I}_4(s).(R_{eq} + 1/(s.C_4))| \tag{6.94}$$

$\Leftrightarrow$ Applying Laplace transforms $(s = j.\omega)$ $\Leftrightarrow$

$$|\overline{V}_{L_s}| = |\overline{I}_{in}.(r_s + j.\omega.L_s)| \tag{6.90}$$

$$|\overline{V}_{L_1}| = |\overline{I}_1.(r_1 + j.\omega.L_1 + Z_{r_{ORMC}})| \tag{6.91}$$

$$|\overline{V}_{L_2}| = |\overline{I}_2.(r_2 + j.\omega.L_3 + 1/(j.\omega.C_2) + Z_{r_{IRMC}})| \tag{6.92}$$

$$|\overline{V}_{L_3}| = |\overline{I}_2.(r_3 + j.\omega.L_3 + Z_{r_{IRMC}})| \tag{6.93}$$

$$|\overline{V}_{L_4}| = |\overline{I}_4.(R_{eq} + 1/(j.\omega.C_4))| \tag{6.94}$$

## 3. Equations for capacitors

The equations for capacitors allow us to determine the resonant frequency and control the energy transfer between the MC coils. Fig. 6.8 illustrates the different meshes where the following capacitors are placed.

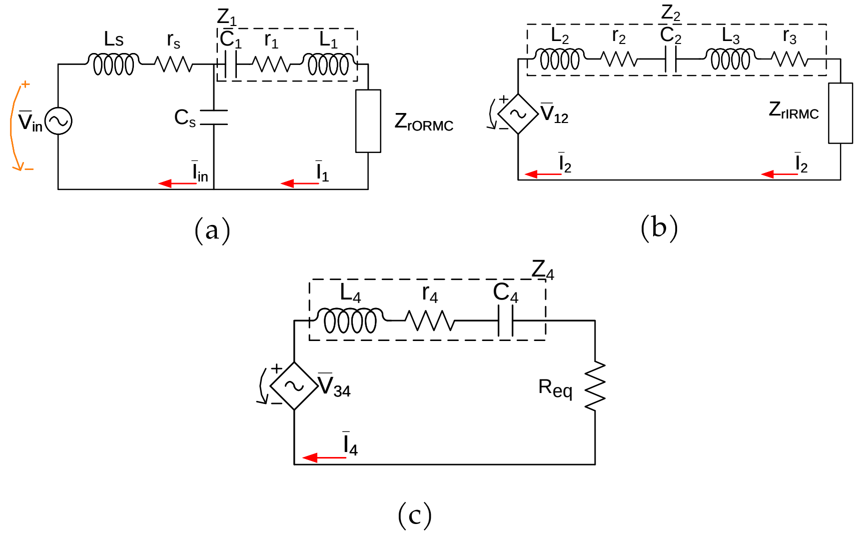


Figure 6.8: (a) $C_s$ and $C_1$ mesh, (b) $C_2$ mesh and (c) $C_4$ mesh

According to the Fig. 6.8, the Kirchhoff's equations of the different meshes are

$$\overline{V}_{in}(s) = \left(s.L_s + \frac{1}{(s.C_s)} + r_s\right)\overline{I}_{in}(s) - \frac{1}{(s.C_s)}\overline{I}_1(s), \tag{6.95}$$

$$Z_{r_{ORMC}}.\overline{I}_1(s) = \frac{1}{(s.C_s)}\overline{I}_{in}(s) - \left(s.L_1 + \frac{1}{(s.C_s)} + \frac{1}{(s.C_1)} + r_1\right)\overline{I}_1(s), \tag{6.96}$$

$$\overline{V}_{12}(s) = \left(s.L_2 + s.L_3 + \frac{1}{(s.C_2)} + r_2 + r_3\right)\overline{I}_2(s) + Z_{r_{IRMC}}.\overline{I}_2(s), \tag{6.97}$$

$$\overline{V}_{34}(s) = \left(s.L_4 + \frac{1}{(s.C_4)} + r_4\right)\overline{I}_4(s) + R_{eq}.\overline{I}_4(s), \tag{6.98}$$

$\Leftrightarrow$ Applying Laplace transforms $(s = j.\omega)$ and $(r_s = r_1 = r_2 = r_3 = r_4 = 0\,\Omega)$ $\Leftrightarrow$

$$\overline{V}_{in} = \left(j.\omega.L_s + \frac{1}{(j.\omega.C_s)}\right)\overline{I}_{in} - \frac{1}{(j.\omega.C_s)}.\overline{I}_{in}, \tag{6.95}$$

$$Z_{r_{ORMC}}.\overline{I}_1 = \frac{1}{(j.\omega.C_1)}\overline{I}_{in} - \left(j.\omega.L_1 + \frac{1}{(j.\omega.C_1)}\right)\overline{I}_1 \tag{6.96}$$

$$\overline{V}_{12} = \left(j.\omega.L_2 + j.\omega.L_3 + \frac{1}{(j.\omega.C_2)}\right)\overline{I}_2 + Z_{r_{IRMC}}.\overline{I}_2, \tag{6.97}$$

$$\overline{V}_{34} = \left(j.\omega.L_4 + \frac{1}{(j.\omega.C_4)}\right)\overline{I}_4 + R_{eq}.\overline{I}_4, \tag{6.98}$$

From (6.95), (6.96), (6.97), (6.98) and assuming the imaginary part equal to 0, the following equations are expressed by

$$\omega_s.L_s - \frac{1}{(\omega_s.C_s)} = 0 \tag{6.99}$$

$$\begin{aligned} \omega_1.L_1 - \frac{1}{(\omega_s.C_s)} - \frac{1}{(\omega_1.C_s)} &= 0 \\ \omega_1.L_1 - \omega_s.L_s - \frac{1}{(\omega_1.C_s)} &= 0 \end{aligned} \tag{6.100}$$

$$\omega_2(L_2 + L_3) - \frac{1}{(\omega_2.C_2)} = 0 \tag{6.101}$$

$$\omega_4.L_4 - \frac{1}{(\omega_4.C_4)} = 0 \tag{6.102}$$

$$\Leftrightarrow \text{Assuming } (\omega_s = \omega_1 = \omega_2 = \omega_4 = \omega) \text{ [50]} \Leftrightarrow$$

$$C_s = 1/(\omega^2.L_s), \tag{6.99}$$

$$C_1 = 1/(\omega^2.(L_1 - L_s)), \tag{6.100}$$

$$C_2 = 1/(\omega^2.(L_2 + L_3)), \tag{6.101}$$

$$C_4 = 1/(\omega^2.L_4). \tag{6.102}$$

## 4. Equations for impedances

The equations for impedances contribute to determining the equations for the voltage and transconductance gains, where these equations allow the identification of the loading profiles of each configuration. The equations for the impedances are given by

$$Z_1(s) = s.L_1 + r_1 + \frac{1}{(s.C_1)}, \tag{6.103}$$

$$Z_2(s) = s.L_2 + s.L_3 + r_2 + r_3 + \frac{1}{(s.C_2)}, \tag{6.104}$$

$$Z_4(s) = s.L_4 + r_4 + \frac{1}{(s.C_4)}, \tag{6.105}$$

$$\Leftrightarrow \text{Applying Laplace transforms } (s = j.\omega) \text{ and } \omega_x = \tfrac{1}{\sqrt{L_x.C_x}} \Leftrightarrow$$

$$Z_1 = r_1 + j.\omega(L_1 - 1/(\omega^2.C_1)), \tag{6.103}$$

$$Z_2 = (r_2 + r_3) + j.\omega.(L_2 + L_3 - 1/(\omega^2.C_2)), \tag{6.104}$$

$$Z_4 = r_4 + j.\omega(L_4 - 1/(\omega^2.C_4)), \tag{6.105}$$

## 5. Equations for reflected impedances under resonance and ideal conditions

The equations for the reflected impedances contribute to determining the equations for the voltage and transconductance gains, where these equations allow the identification of the loading profiles of each configuration. The equations for the reflected impedances are given by

$$Z_{r_{IRMC}}(s) = -\frac{s^2.L_{34}^2}{(Z_4 + R_{eq})} \tag{6.106}$$

$$Z_{r_{ORMC}}(s) = -\frac{s^2.L_{12}^2}{(Z_2 + Z_{r_{IRMC}}(s))} \tag{6.107}$$

$\Leftrightarrow$ Applying Laplace transforms ($s = j.\omega$) and
considering the conditions ($r_s = r_1 = r_2 = r_3 = r_4 = 0\ \Omega$) e ($\omega = \omega_x$) $\Leftrightarrow$

$$Z_{r_{IRMC}} = \frac{\omega^2.L_{34}^2}{R_{eq}} \tag{6.106}$$

$$Z_{r_{ORMC}} = \frac{\frac{\omega^2.L_{12}^2}{1}}{\frac{\omega^2.L_{34}^2}{R_{eq}}} = \frac{\omega^2.L_{12}^2(Z_4 + R_{eq})}{(Z_2(Z_4 + R_{eq}) + \omega^2.L_{34}^2)} = \frac{L_{12}^2.R_{eq}}{L_{34}^2} \tag{6.107}$$

## 6. Input impedance

The input impedance $Z_{in}$ is the equivalent impedance seen by the power supply and it is the aggregated of the reflected impedance from IRMC and the receiver side ORMC onto the transmitter side ORMC and the equivalent impedances of the transmitter side ORMC and input side. The equation of $Z_{in}$ is shown by

$$Z_{in}(s) = r_s + s.L_s + \frac{1}{(s.C_s)} - \frac{1}{s^2.C_s^2\left(Z_1 + Z_{r_{ORMC}} + \frac{1}{(s.C_s)}\right)}. \tag{6.108}$$

If the system losses are neglected ($r_s = r_1 = r_2 = r_3 = r_4 = 0\ \Omega$), apply the Laplace transforms ($s = j.\omega$) and the system is under resonance ($\omega = \omega_x$), using MATLAB simplify function, (6.108) is defined by

$$Z_{in} = \frac{\omega^2.L_s^2.L_{34}^2}{L_{12}^2.R_{eq}}. \tag{6.109}$$

Assuming the mentioned conditions, (6.109) is purely resistive and depends on the ratio of $L_{34}^2/L_{12}^2$, $L_s^2$ and $\omega^2$.

## 7. Voltage and transconductance gain equations

The equations of voltage gains and transconductance where these equations allow identifying the loading profiles of each configuration. Considering the current equations, it is possible to determine the equations for the gains that are given by

$$G_{vReqvin} = \frac{\overline{V}_{R_{eq}}}{\overline{V}_{in}}, \tag{6.110}$$

$$G_{i4vin} = \frac{\overline{I}_4}{\overline{V}_{in}}, \tag{6.111}$$

$$G_{i2vin} = \frac{\overline{I}_2}{\overline{V}_{in}}, \tag{6.112}$$

$$G_{i1vin} = \frac{\overline{I}_1}{\overline{V}_{in}}, \tag{6.113}$$

$\Leftrightarrow$ Applying the equalities between the equations of the currents and highlighting $\Leftrightarrow$

$$G_{vReqvin}(s) = \frac{R_{eq}(s.L_{12}.L_{34})}{C_s(Z_4+R_{eq})(Z_2+Z_{r_{IRMC}})\left(Z_1+\frac{1}{(s.C_s)}+Z_{r_{ORMC}}\right)\left(r_s+s.L_s+\frac{1}{(s.C_s)}-\frac{1}{s^2.C_s^2\left(Z_1+Z_{r_{ORMC}}+\frac{1}{(s.C_s)}\right)}\right)}, \tag{6.110}$$

$$G_{i4vin}(s) = \frac{(s.L_{12}.L_{34})}{C_s(Z_4+R_{eq})(Z_2+Z_{r_{IRMC}})\left(Z_1+\frac{1}{(s.C_s)}+Z_{r_{ORMC}}\right)\left(r_s+s.L_s+\frac{1}{(s.C_s)}-\frac{1}{s^2.C_s^2\left(Z_1+Z_{r_{ORMC}}+\frac{1}{(s.C_s)}\right)}\right)}, \tag{6.111}$$

$$G_{i2vin}(s) = \frac{L_{12}}{C_s(Z_2+Z_{r_{IRMC}})\left(Z_1+\frac{1}{(s.C_s)}+Z_{r_{ORMC}}\right)\left(r_s+s.L_s+\frac{1}{(s.C_s)}-\frac{1}{s^2.C_s^2\left(Z_1+Z_{r_{ORMC}}+\frac{1}{(s.C_s)}\right)}\right)}. \tag{6.112}$$

$$G_{i1vin}(s) = \frac{1}{s.C_s\left(Z_1+\frac{1}{(s.C_s)}+Z_{r_{ORMC}}\right)\left(r_s+s.L_s+\frac{1}{(s.C_s)}-\frac{1}{s^2.C_s^2\left(Z_1+Z_{r_{ORMC}}+\frac{1}{(s.C_s)}\right)}\right)}. \tag{6.113}$$

$\Leftrightarrow$ Applying Laplace transforms $(s = j.\omega)$ $\Leftrightarrow$

$$G_{vReqvin} = \frac{j.\omega.R_{eq}.L_{12}.L_{34}}{C_s(R_{eq}+Z_4)\left(Z_1+Z_{r_{ORMC}}+\frac{1}{(j.\omega.C_s)}\right)(Z_2+Z_{r_{IRMC}})\left(r_s+j.\omega.L_s+\frac{1}{(j.\omega.C_s)}+\frac{1}{C_s^2.\omega^2\left(Z_1+Z_{r_{ORMC}}+\frac{1}{(j.\omega.C_s)}\right)}\right)}. \tag{6.110}$$

$$G_{i4vin} = \frac{j.\omega.L_{12}.L_{34}}{C_s(R_{eq}+Z_4)\left(Z_1+Z_{r_{ORMC}}+\frac{1}{(j.\omega.C_s)}\right)(Z_2+Z_{r_{IRMC}})\left(r_s+j.\omega.L_s+\frac{1}{(j.\omega.C_s)}+\frac{1}{C_s^2.\omega^2\left(Z_1+Z_{r_{ORMC}}+\frac{1}{(j.\omega.C_s)}\right)}\right)}. \tag{6.111}$$

$$G_{i2vin} = \frac{L_{12}}{C_s\left(Z_1+Z_{r_{ORMC}}+\frac{1}{(j.\omega.C_s)}\right)(Z_2+Z_{r_{IRMC}})\left(r_s+j.\omega.L_s+\frac{1}{(j.\omega.C_s)}+\frac{1}{C_s^2.\omega^2\left(Z_1+Z_{r_{ORMC}}+\frac{1}{(j.\omega.C_s)}\right)}\right)}. \tag{6.112}$$

$$G_{i1vin} = -\frac{j}{C_s.\omega\left(Z_1+Z_{r_{ORMC}}+\frac{1}{(j.\omega.C_s)}\right)\left(r_s+j.\omega.L_s+\frac{1}{(j.\omega.C_s)}+\frac{1}{C_s^2.\omega^2\left(Z_1+Z_{r_{ORMC}}+\frac{1}{(j.\omega.C_s)}\right)}\right)}. \tag{6.113}$$

$\Leftrightarrow$ If the system is under resonance $(\omega = \omega_x)$ and $(r_1 = r_2 = r_3 = r_4 = 0\ \Omega)$, using MATLAB simplify function $\Leftrightarrow$

$$G_{vReqvin} = \frac{j.R_{eq}.L_{12}}{L_s.L_{34}.\omega}. \tag{6.110}$$

$$G_{i4vin} = \frac{j.L_{12}}{L_s.L_{34}.\omega}. \tag{6.111}$$

$$G_{i2vin} = \frac{R_{eq}.L_{12}}{L_{34}^2.L_s.\omega^2}. \tag{6.112}$$

$$G_{i1vin} = -\frac{j}{\omega.L_s}. \tag{6.113}$$

# Appendix E - Characterization of Multiple Integrated Pad Geometries for in-Wheel EV IPT Applications - Results

## IRMC

- (SP) Wood structure: $L_3$, $L_4$, $L_{34}$ e $k_{34}$ as a function of coil width

COIL WIDTH INCREASE

| Ns=5 turns \| Airgap 15 mm | | | | |
|---|---|---|---|---|
| Coil width [mm] | $L_3$ [μH] | $L_4$ [μH] | $L_{34}$ [μH] | $k_{34}$ |
| 42 | 23,88 | 20,01 | 12,025 | 0,550103 |
| 75 | 19,88 | 16,9 | 11,215 | 0,611854 |
| 109 | 18,35 | 15,13 | 10,265 | 0,616058 |
| 142 | 17,99 | 13,53 | 9,34 | 0,598663 |
| 169 | 16,96 | 11,61 | 8,275 | 0,589711 |

SELF AND MUTUAL INDUCTANCE DECREASE AND COUPLING FACTOR INCREASE

Figure 6.9: Table of experimental results for IRMC as function of coil width for Self-inductances $L_3$ and $L_4$ and, Mutual inductance $L_{34}$ and Coupling factor $k_{34}$.

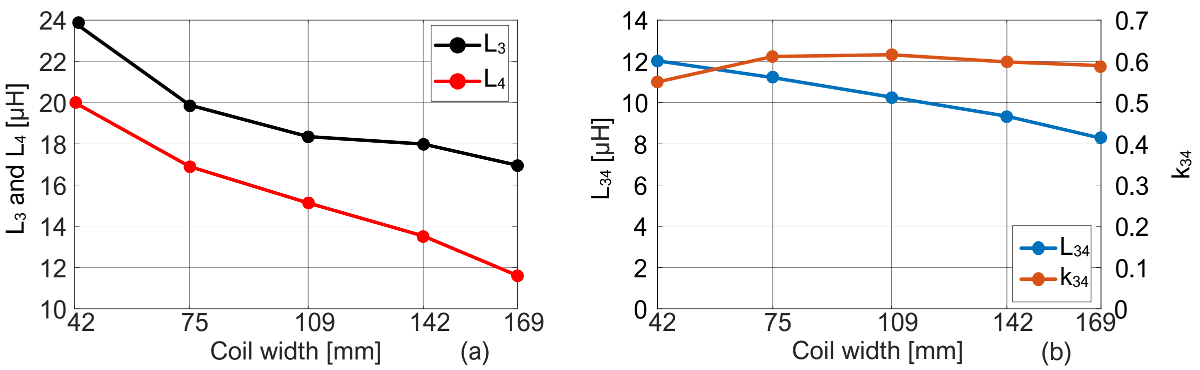


Figure 6.10: Experimental results for IRMC as function of coil width/space between turns for (a) Self-inductances $L_3$ and $L_4$ and, (b) Mutual inductance $L_{34}$ and Coupling factor $k_{34}$.

- (SP) Aluminium structure: $L_3$, $L_4$, $L_{34}$ e $k_{34}$ as a function of number of turns $N_s$ for different air gaps and core width $core_w$

**FERROMAGNETIC VOLUME INCREASE**

**AIRGAP INCREASE**

| Ferrites 12+12 (12x1x(43x24x4)/core$_{w1}$) \| Airgap 10 mm | | | | |
|---|---|---|---|---|
| N turns | $L_3$ [µH] | $L_4$ [µH] | $L_{34}$ [µH] | $k_{34}$ |
| 2 | 17,16 | 20,75 | 1,1 | 0,058294 |
| 4 | 19,29 | 22,38 | 3,575 | 0,17206 |
| 6 | 21,15 | 25,37 | 6,58 | 0,28406 |
| 8 | 22,55 | 26,66 | 8,87 | 0,36176 |
| 10 | 23,95 | 28,35 | 10,545 | 0,404685 |

| Ferrites 24+24 (12x2x(43x24x4)/core$_{w2}$) \| Airgap 10 mm | | | | |
|---|---|---|---|---|
| N turns | $L_3$ [µH] | $L_4$ [µH] | $L_{34}$ [µH] | $k_{34}$ |
| 2 | 18,26 | 22,26 | 2,34 | 0,116065 |
| 4 | 23,63 | 26,72 | 6,825 | 0,271614 |
| 6 | 30,19 | 33,82 | 14,48 | 0,453159 |
| 8 | 37,09 | 41,48 | 22,265 | 0,567643 |
| 10 | 43,05 | 48,56 | 28,795 | 0,629783 |

| Ferrites 12+12 (12x1x(43x24x4)/corew1) \| Airgap 15 mm | | | | |
|---|---|---|---|---|
| N turns | $L_3$ [µH] | $L_4$ [µH] | $L_{34}$ [µH] | $k_{34}$ |
| 2 | 16,74 | 20,43 | 0,73 | 0,039474 |
| 4 | 18,57 | 22,75 | 2,665 | 0,129658 |
| 6 | 20,75 | 25,28 | 4,995 | 0,218091 |
| 8 | 22,15 | 26,69 | 6,895 | 0,283578 |
| 10 | 23 | 27,49 | 7,83 | 0,311394 |

| Ferrites 24+24 (12x2x(43x24x4)/corew2) \| Airgap 15 mm | | | | |
|---|---|---|---|---|
| N turns | $L_3$ [µH] | $L_4$ [µH] | $L_{34}$ [µH] | $k_{34}$ |
| 2 | 18,11 | 22,1 | 1,55 | 0,077478 |
| 4 | 22,93 | 27,02 | 6,96 | 0,279618 |
| 6 | 29,73 | 33,88 | 12,915 | 0,406935 |
| 8 | 36,84 | 41,38 | 19,94 | 0,510705 |
| 10 | 43,86 | 48,26 | 25,09 | 0,545347 |

Figure 6.11: Table of experimental results for IRMC as function of the number of turns, considering different air gaps and, ferrite width, for Self-inductances $L_3$ and $L_4$ and, Mutual inductance $L_{34}$ and Coupling factor $k_{34}$.

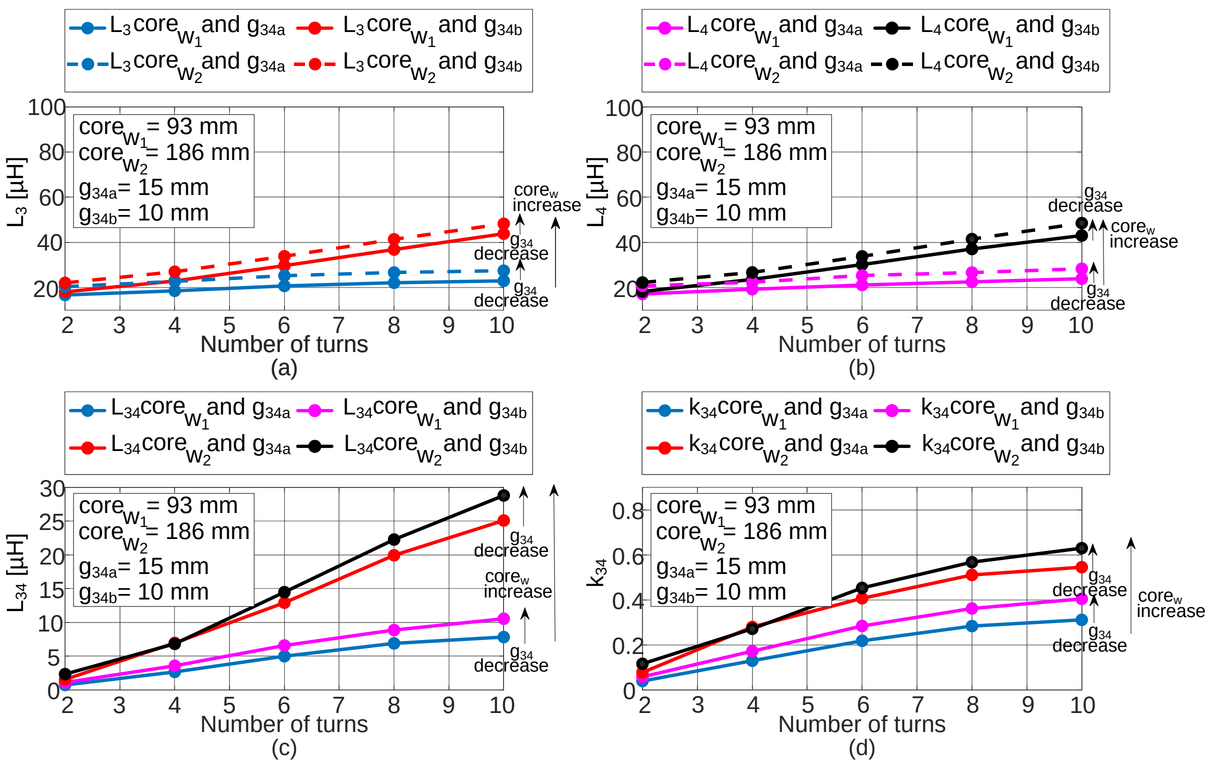


Figure 6.12: Experimental results for IRMC as function of the number of turns, considering different air gaps and, ferrite width, for (a) Self-inductance $L_3$, (b) Self-inductance $L_4$, (c) Mutual inductance $L_{34}$ and (d) Coupling factor $k_{34}$.

## ORMC

- (DDP-BPP) Aluminium structure: $L_1$, $L_2$, $L_{12}$ e $k_{12}$ as a function of wheel's rotation angle $\theta$ for $airgap = 20\ mm$, different core width and different misalignment in $x$ axis

  **Core:** 12x1x(93x28x16)

**ORMC coupled**

**Ns 10+8 (Copper+Litz/DDP+BPP) / Airgap - 20 mm / Cores 12x1x(93x28x16) / Mx = 0 mm**

| Ang de Rot [Graus] | $L_1$ [μH] | $L_2$ [μH] | $L_{12}$ [μH] | $k_{12}$ | |
|---|---|---|---|---|---|
| -60 | 75,16 | 31,75 | 3,405 | 0,069703063 | ferrite alinhada |
| -52,5 | 75,14 | 31,79 | 2,915 | 0,059642756 | ferrite desalinhada |
| -45 | 75,11 | 31,84 | 2,225 | 0,045498241 | ferrite desalinhada |
| -37,5 | 75,13 | 31,85 | 1,24 | 0,025348967 | ferrite desalinhada |
| -30 | 75,15 | 31,8 | 0,175 | 0,00357981 | ferrite alinhada |
| -22,5 | 75,11 | 31,8 | 1,245 | 0,025474573 | ferrite desalinhada |
| -15 | 75,06 | 31,78 | 2,53 | 0,051801137 | ferrite desalinhada |
| -7,5 | 75,1 | 31,75 | 3,775 | 0,077308122 | ferrite desalinhada |
| 0 | 75,16 | 31,74 | 4,3 | 0,088038292 | ferrite alinhada |
| 7,5 | 75,12 | 31,77 | 3,705 | 0,07584061 | ferrite desalinhada |
| 15 | 75,08 | 31,71 | 2,755 | 0,056462662 | ferrite desalinhada |
| 22,5 | 75,12 | 31,65 | 0,965 | 0,019790769 | ferrite desalinhada |
| 30 | 75,15 | 31,56 | 0,005 | 0,000102668 | ferrite alinhada |
| 37,5 | 75,11 | 31,73 | 1,02 | 0,020893743 | ferrite desalinhada |
| 45 | 75,09 | 31,72 | 2,005 | 0,041082488 | ferrite desalinhada |
| 52,5 | 75,14 | 31,71 | 2,675 | 0,0548012 | ferrite desalinhada |
| 60 | 75,17 | 31,7 | 3,035 | 0,062173711 | ferrite alinhada |

**ORMC coupled**

**Ns 10+8 (Copper+Litz/DDP+BPP) / Airgap - 20 mm / Cores 12x1x(93x28x16) / Mx = 50 mm**

| Ang de Rot [Graus] | $L_1$ [μH] | $L_2$ [μH] | $L_{12}$ [μH] | $k_{12}$ | |
|---|---|---|---|---|---|
| -60 | 76,62 | 31,73 | 3,525 | 0,07149127 | ferrite alinhada |
| -52,5 | 76,66 | 31,77 | 3,615 | 0,073251292 | ferrite desalinhada |
| -45 | 76,64 | 31,79 | 3,315 | 0,067159974 | ferrite desalinhada |
| -37,5 | 76,61 | 31,8 | 2,755 | 0,055816849 | ferrite desalinhada |
| -30 | 76,65 | 31,81 | 1,93 | 0,039085835 | ferrite alinhada |
| -22,5 | 76,67 | 31,81 | 0,34 | 0,006884689 | ferrite desalinhada |
| -15 | 76,6 | 31,78 | 0,91 | 0,018443785 | ferrite desalinhada |
| -7,5 | 76,56 | 31,75 | 2,195 | 0,044520671 | ferrite desalinhada |
| 0 | 76,63 | 31,66 | 4,155 | 0,084356035 | ferrite alinhada |
| 7,5 | 76,67 | 31,67 | 4,53 | 0,091930885 | ferrite desalinhada |
| 15 | 76,6 | 31,69 | 3,855 | 0,07824361 | ferrite desalinhada |
| 22,5 | 76,59 | 31,72 | 2,795 | 0,056706023 | ferrite desalinhada |
| 30 | 76,65 | 31,73 | 1,61 | 0,03264636 | ferrite alinhada |
| 37,5 | 76,66 | 31,72 | 0,16 | 0,003244658 | ferrite desalinhada |
| 45 | 76,6 | 31,71 | 0,605 | 0,012275604 | ferrite desalinhada |
| 52,5 | 76,59 | 31,71 | 1,35 | 0,027393632 | ferrite desalinhada |
| 60 | 76,66 | 31,7 | 2,28 | 0,046250966 | ferrite alinhada |

**ORMC coupled**

**Ns 10+8 (Copper+Litz/DDP+BPP) / Airgap - 20 mm / Cores 12x1x(93x28x16) / Mx = -50 mm**

| Ang de Rot [Graus] | $L_1$ [μH] | $L_2$ [μH] | $L_{12}$ [μH] | $k_{12}$ | |
|---|---|---|---|---|---|
| -60 | 77,29 | 31,87 | 2,18 | 0,043924195 | ferrite alinhada |
| -52,5 | 77,23 | 31,89 | 1,31 | 0,026396784 | ferrite desalinhada |
| -45 | 77,23 | 31,91 | 0,27 | 0,005438853 | ferrite desalinhada |
| -37,5 | 77,27 | 31,94 | 0,845 | 0,017009196 | ferrite desalinhada |
| -30 | 77,26 | 31,92 | 1,81 | 0,036447671 | ferrite alinhada |
| -22,5 | 77,18 | 31,91 | 3,005 | 0,060552027 | ferrite desalinhada |
| -15 | 77,2 | 31,88 | 4,01 | 0,080830742 | ferrite desalinhada |
| -7,5 | 77,28 | 31,92 | 4,45 | 0,089597319 | ferrite desalinhada |
| 0 | 77,28 | 31,87 | 3,825 | 0,077073814 | ferrite alinhada |
| 7,5 | 77,21 | 31,77 | 2,01 | 0,04058361 | ferrite desalinhada |
| 15 | 77,23 | 31,73 | 0,37 | 0,007474354 | ferrite desalinhada |
| 22,5 | 77,29 | 31,73 | 0,91 | 0,018375734 | ferrite desalinhada |
| 30 | 77,26 | 31,81 | 1,685 | 0,033989182 | ferrite alinhada |
| 37,5 | 77,2 | 31,82 | 2,46 | 0,049633668 | ferrite desalinhada |
| 45 | 77,25 | 31,81 | 3,03 | 0,061123969 | ferrite desalinhada |
| 52,5 | 77,29 | 31,78 | 3,185 | 0,064264456 | ferrite desalinhada |
| 60 | 77,26 | 31,76 | 2,96 | 0,059754981 | ferrite alinhada |

Figure 6.13: Table of experimental results for ORMC with DDP-BPP topology and 12x1 Core as function of wheel's rotation angle, with different misalignment in $x$ axis and different core width, for Self-inductances $L_1$ and $L_2$ and Mutual inductance $L_{12}$ and Coupling factor $k_{12}$.

- (DDP-BPP) Aluminium structure: $L_1$, $L_2$, $L_{12}$ e $k_{12}$ as a function of wheel's rotation angle $\theta$ for $airgap = 20\ mm$, different core width and different misalignment in $x$ axis

  **Core:** 12x2x(93x28x16)

**ORMC coupled**

Ns 10+8 (Copper+Litz/DDP+BPP) / Airgap - 20 mm / Cores 12x2x(93x28x16) / Mx = 0 mm

| Ang de Rot [Graus] | $L_1$ [μH] | $L_2$ [μH] | $L_{12}$ [μH] | $k_{12}$ | |
|---|---|---|---|---|---|
| -60 | 78,35 | 35,66 | 3,555 | 0,067255752 | ferrite alinhada |
| -52,5 | 78,24 | 35,68 | 3,21 | 0,060754463 | ferrite desalinhada |
| -45 | 78,12 | 35,67 | 2,145 | 0,040634472 | ferrite desalinhada |
| -37,5 | 78,23 | 35,67 | 0,9 | 0,017037438 | ferrite desalinhada |
| -30 | 78,35 | 35,65 | 0,75 | 0,014190967 | ferrite alinhada |
| -22,5 | 78,27 | 35,63 | 2,8 | 0,053021554 | ferrite desalinhada |
| -15 | 78,19 | 35,61 | 4,5 | 0,085280732 | ferrite desalinhada |
| -7,5 | 78,24 | 35,6 | 5,88 | 0,111413523 | ferrite desalinhada |
| 0 | 78,26 | 35,6 | 6,67 | 0,126366196 | ferrite alinhada |
| 7,5 | 78,05 | 35,59 | 6,23 | 0,118205477 | ferrite desalinhada |
| 15 | 77,91 | 35,62 | 4,385 | 0,083238844 | ferrite desalinhada |
| 22,5 | 78 | 35,61 | 2,695 | 0,05113585 | ferrite desalinhada |
| 30 | 78,13 | 35,69 | 0,54 | 0,010226136 | ferrite alinhada |
| 37,5 | 78,06 | 35,7 | 1,28 | 0,0242472 | ferrite desalinhada |
| 45 | 77,99 | 35,71 | 2,85 | 0,054004565 | ferrite desalinhada |
| 52,5 | 78,18 | 35,72 | 3,8 | 0,071908468 | ferrite desalinhada |
| 60 | 78,27 | 35,7 | 4,335 | 0,082008209 | ferrite alinhada |

**ORMC coupled**

Ns 10+8 (Copper+Litz/DDP+BPP) / Airgap - 20 mm / Cores 12x2x(93x28x16) / Mx = 50 mm

| Ang de Rot [Graus] | $L_1$ [μH] | $L_2$ [μH] | $L_{12}$ [μH] | $k_{12}$ | |
|---|---|---|---|---|---|
| -60 | 76,94 | 35,4 | 3,17 | 0,060740944 | ferrite alinhada |
| -52,5 | 77,04 | 35,45 | 3,545 | 0,067834399 | ferrite desalinhada |
| -45 | 76,93 | 35,41 | 3,27 | 0,062652286 | ferrite desalinhada |
| -37,5 | 76,82 | 35,43 | 2,625 | 0,050316055 | ferrite desalinhada |
| -30 | 76,95 | 35,44 | 1,345 | 0,025755567 | ferrite alinhada |
| -22,5 | 77,04 | 35,44 | 0,04 | 0,000765517 | ferrite desalinhada |
| -15 | 76,97 | 35,42 | 1,805 | 0,034569427 | ferrite desalinhada |
| -7,5 | 76,89 | 35,41 | 3,7 | 0,070909403 | ferrite desalinhada |
| 0 | 76,9 | 35,4 | 5,85 | 0,112122059 | ferrite alinhada |
| 7,5 | 76,84 | 35,37 | 6,795 | 0,130340161 | ferrite desalinhada |
| 15 | 76,66 | 35,39 | 6,375 | 0,122392696 | ferrite desalinhada |
| 22,5 | 76,56 | 35,4 | 5,42 | 0,104111018 | ferrite desalinhada |
| 30 | 76,67 | 35,41 | 3,41 | 0,065445333 | ferrite alinhada |
| 37,5 | 76,78 | 35,42 | 2,1 | 0,040269011 | ferrite desalinhada |
| 45 | 76,67 | 35,42 | 0,005 | 9,59474E-05 | ferrite desalinhada |
| 52,5 | 76,63 | 35,44 | 1,335 | 0,025617397 | ferrite desalinhada |
| 60 | 76,77 | 35,43 | 2,7 | 0,051770507 | ferrite alinhada |

**ORMC coupled**

Ns 10+8 (Copper+Litz/DDP+BPP) / Airgap - 20 mm / Cores 12x2x(93x28x16) / Mx = -50 mm

| Ang de Rot [Graus] | $L_1$ [μH] | $L_2$ [μH] | $L_{12}$ [μH] | $k_{12}$ | |
|---|---|---|---|---|---|
| -60 | 77,66 | 35,59 | 2,175 | 0,041371053 | ferrite alinhada |
| -52,5 | 77,53 | 35,6 | 1,115 | 0,021223401 | ferrite desalinhada |
| -45 | 77,61 | 35,62 | 0,285 | 0,005420496 | ferrite desalinhada |
| -37,5 | 77,76 | 35,63 | 1,405 | 0,026692564 | ferrite desalinhada |
| -30 | 77,72 | 35,62 | 3,53 | 0,06709055 | ferrite alinhada |
| -22,5 | 77,62 | 35,59 | 4,945 | 0,094083937 | ferrite desalinhada |
| -15 | 77,66 | 35,56 | 6,24 | 0,118742181 | ferrite desalinhada |
| -7,5 | 77,76 | 35,54 | 6,6 | 0,125547219 | ferrite desalinhada |
| 0 | 77,68 | 35,52 | 5,95 | 0,113272863 | ferrite alinhada |
| 7,5 | 77,54 | 35,51 | 4,125 | 0,078611434 | ferrite desalinhada |
| 15 | 77,62 | 35,47 | 1,805 | 0,034400107 | ferrite desalinhada |
| 22,5 | 77,78 | 35,49 | 0,515 | 0,009802126 | ferrite desalinhada |
| 30 | 77,72 | 35,5 | 1,66 | 0,031602942 | ferrite alinhada |
| 37,5 | 77,59 | 35,5 | 3,045 | 0,058019001 | ferrite desalinhada |
| 45 | 77,65 | 35,47 | 4,06 | 0,077361469 | ferrite desalinhada |
| 52,5 | 77,75 | 35,46 | 4,305 | 0,081988623 | ferrite desalinhada |
| 60 | 77,62 | 35,47 | 3,895 | 0,07423181 | ferrite alinhada |

Figure 6.14: Table of experimental results for ORMC with DDP-BPP topology and 12x2 Core as function of wheel's rotation angle, with different misalignment in $x$ axis and different core width, for Self-inductances $L_1$ and $L_2$ and Mutual inductance $L_{12}$ and Coupling factor $k_{12}$.

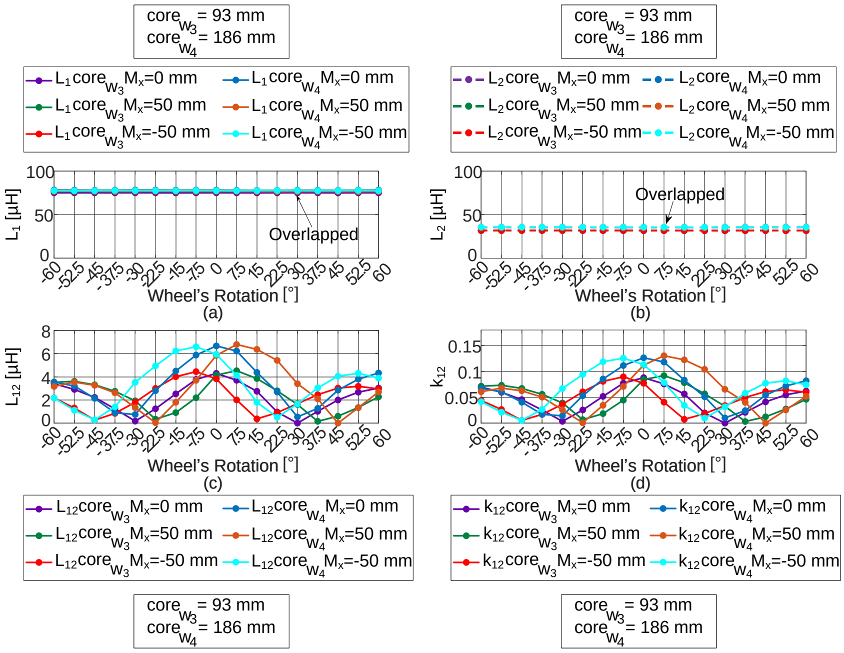


Figure 6.15: Experimental results for ORMC with DDP-Solenoid topology as function of wheel's rotation angle, with different misalignment in $x$ axis and different core width, for (a) Self-inductance $L_1$, (b) Self-inductance $L_2$, (c) Mutual inductance $L_{12}$ and (d) Coupling factor $k_{12}$.

Miguel Moreira Torres

Instituto Superior
de Engenharia
Politécnico de Coimbra